SAN DIEGO STATE UNIVERSITY
AND
UNIVERSITY OF CALIFORNIA, SAN DIEGO

Parallel goal-oriented adaptive finite element modeling for 3D electromagnetic exploration

A dissertation submitted in partial satisfaction of the
requirements for the degree
Doctor of Philosophy

in

Geophysics

by

Yuxiang Zhang

Committee in charge:

University of California, San Diego:
Professor Kerry Key, Chair
Professor Yuri Fialko
Professor Michael Holst
Professor Len Srnka

San Diego State University:
Professor Steve Day
Professor Samuel Shen

2017

The dissertation of Yuxiang Zhang is approved, and it is acceptable in quality and form for publication on microfilm and electronically:

_____

_____

_____

_____

_____

_____

University of California, San Diego

San Diego State University

2017

DEDICATION

To my parents, Xin'an and Shudi.

EPIGRAPH

A journey of a thousand miles commences with the first step.

- Laozi, Tao Te Ching

All models are wrong, but some are useful .

- George Box.

TABLE OF CONTENTS

Signature Page . . . iii

Dedication . . . iv

Epigraph . . . v

Table of Contents . . . vi

List of Figures . . . viii

List of Tables . . . x

Acknowledgements . . . xi

Vita . . . xiv

Abstract of the Dissertation . . . xv

Chapter 1 Introduction . . . 1
- 1.1 Marine Electromagnetic Exploration . . . 3
  - 1.1.1 Controlled-source EM method . . . 3
  - 1.1.2 Marine Magnetotelluric Method . . . 4
  - 1.1.3 Physical Problem in Exploration Geophysics . . . 5
- 1.2 Basic Theory of 3D Electromagnetic Modeling . . . 8
  - 1.2.1 Opportunities and Challenges for Large Scale 3D Modeling and Inversion . . . 9
  - 1.2.2 Forward Problem . . . 10
  - 1.2.3 Inverse Problem . . . 14

Chapter 2 Goal-oriented adaptive finite element modeling for 3D Electromagnetics . . . 17
- 2.1 Introduction . . . 17
- 2.2 Finite Element Analysis . . . 21
  - 2.2.1 Weak formulation of Electric Field Problem . . . 22
  - 2.2.2 Finite Element Approximation . . . 23
  - 2.2.3 Meshing . . . 25
  - 2.2.4 Numerical Computation . . . 25
- 2.3 Goal-oriented Adaptive Refinement . . . 27
  - 2.3.1 Dual Problem Formulation . . . 29
  - 2.3.2 Residual Based Error Estimation . . . 30
  - 2.3.3 Hierarchical Basis Error Estimation . . . 33
  - 2.3.4 Iteratively Adaptive Refinement Scheme . . . 35

2.4 Parallel Domain Decomposition 36
2.4.1 Data Domain Decomposition 36
2.5 Numerical Examples 43
2.5.1 Canonical Model 43
2.5.2 Model with Bathymetry 48
2.5.3 Conclusion 53

Chapter 3 Inversion 57
3.1 A review of Non-linear Inversion for EM geophysics 58
3.2 Occam's Razor: Simplest solution is preferred 60
3.2.1 Model Parameterization Using Dual Grid Strategy . 63
3.2.2 Calculation of First and Second Order Derivatives . . 65
3.2.3 Regularization: Model Roughness as Penalty 68
3.2.4 Bounding the Model Parameters 69
3.3 Synthetic Inversion Examples 72
3.3.1 Half-space Model 72
3.3.2 Model with Reservoir 83
3.3.3 Model with Reservoir and bathymetry 93
3.3.4 Conclusion 96

Chapter 4 Conclusion and Outlook 101
4.1 Conclusions 101
4.2 Outlook 102
4.2.1 Iterative solver development 103
4.2.2 Inversion scalability improvement 105

Bibliography 108

LIST OF FIGURES

Figure 1.1: EM exploration in the oceans 3

Figure 2.1: Data decomposition example on the 3D oil reservoir model 38
Figure 2.2: Overview of the subgroups for box partitioning pattern 39
Figure 2.3: Overview of the subgroups for stripe partitioning pattern 40
Figure 2.4: Final refinement results for subgroups 6th and 15th of model with 4 transmitters 41
Figure 2.5: The 5-layered 1D model 43
Figure 2.6: Validation of the electric and magnetic field responses computed by MARE3DEM(dots) for the 1-D layered reservoir model 44
Figure 2.7: Relative error in the solution decreases with each successive mesh refinement iteration 45
Figure 2.8: The slice cut over the seafloor for the 1D model 46
Figure 2.9: The comparison between two error estimation approaches based on the 1D layered model 47
Figure 2.10: Dual error distribution on the seafloor in each iteration 49
Figure 2.11: Overview of the regional bathymetry 50
Figure 2.12: View of the topography after removing the seawater and air layers . 51
Figure 2.13: Convergence of the electric and magnetic field amplitude 52
Figure 2.14: Initial mesh and final mesh of the 3D model 54
Figure 2.15: Anomaly generated by the oil reservoir 55

Figure 3.1: Polygon of the inverse model 64
Figure 3.2: The sensitivity distribution of the Jacobian for a specific transmitter and receiver pairs 67
Figure 3.3: Model roughness in 2D 69
Figure 3.4: Synthetic half-space inversion model 73
Figure 3.5: Convergence of the Regular Occam algorithms on half-space model: Experiment 1 75
Figure 3.6: Inverted result for the two layered model 76
Figure 3.7: Convergence of the Regular Occam algorithms on half-space model: Experiment 2 77
Figure 3.8: Convergence of the Regular Occam algorithms on half-space model: Experiment 3 79
Figure 3.9: Convergence of the Regular Occam algorithms on half-space model: Experiment 4 80
Figure 3.10: Convergence of the Regular Occam algorithms on half-space model: Experiment 5 82
Figure 3.11: Oil reservoir model 83
Figure 3.12: Convergence of the Regular Occam algorithms on the oil reservoir model with receivers line 84

Figure 3.13: Inverted result of the oil reservoir model with line receivers 85
Figure 3.14: Transmitters and receivers layout on the oil reservoir model 86
Figure 3.15: Convergence of the Regular Occam algorithms on oil reservoir model with receivers grid 87
Figure 3.16: Inverted result of the oil reservoir model with receivers grid 88
Figure 3.17: Convergence for the oil reservoir model: Experiment 3 89
Figure 3.18: RMS misfit shown as a function of Occam iteration for the oil reservoir model 90
Figure 3.19: Inverted result for each iteration of the oil reservoir model with receiver grid: from iteration 1 to 8 91
Figure 3.20: Inverted result for each iteration of the oil reservoir model with receiver grid: from iteration 9 to 14 92
Figure 3.21: Convergence for the oil reservoir model with bathymetry 93
Figure 3.22: RMS misfit shown as a function of Occam iteration for the bathymetry model 94
Figure 3.23: Inverted results for each iteration of the model with bathymetry: from iteration 1 to 8 95
Figure 3.24: Inverted results for each iteration of the model with bathymetry: from iteration 9 to 10 96
Figure 3.25: Lateral variation of the final model: from offset 1 to 8 97
Figure 3.26: Lateral variation of the final model: from offset 9 to 14 98
Figure 3.27: Vertical variation of the final model: from offset 1 to 8 99
Figure 3.28: Vertical variation of the final model: from offset 9 to 12 100

Figure 4.1: Run-time scaling and speed-up of the ScaLAPACK routines used for the dense matrix operations 106

LIST OF TABLES

Table 2.1: Parallel performance analysis using data decomposition scheme. . . 37
Table 2.2: Performance comparison between models with single and multiple transmitters . . . 37
Table 2.3: Runtime and memory usage for each iteration on the 1D layered model 48
Table 2.4: Runtime and memory usage for each iteration for the 3D reservoir model . . . 48

Table 3.1: Layout of the inversion experiments . . . 74
Table 3.2: Resistivity, RMS and Model Roughness for each iteration: Experiment 1 . . . 75
Table 3.3: Resistivity, RMS and Model Roughness for each iteration: Experiment 2 . . . 78
Table 3.4: Resistivity, RMS and Model Roughness for each iteration: Experiment 3 . . . 78
Table 3.5: Resistivity, RMS and Model Roughness for each iteration: Experiment 4 . . . 81
Table 3.6: Multiple frequency example: Resistivity, RMS and Model Roughness for each iteration . . . 81

ACKNOWLEDGEMENTS

First of all, I wish to thank my advisor, Kerry Key, whose passion for science has not only motivated me to explore the unknown in geophysics, but also ignited my enthusiasm for life. He has been a great mentor by always giving his unwavering support, whether it was to encourage me to attend conferences or connect me with various opportunities. He is also incredibly enthusiastic about me as a person more than just as a researcher, not only allowing me the flexibility for choosing the research path, but also high-fiving me at various milestones of my study. I am extremely grateful for the guidance and support, that he has presented me every step of the way.

I owe Prof. Steve Day gratitude for accepting me to this exciting program five years ago and giving me the opportunity to take this life-changing academic journey. I thank Prof. Michael Holst for finding time in his busy daily schedule to share his insights on error estimation and model domain decomposition. I am very thankful to Prof. Len Srnka for his useful comments and ideas that have helped improve this dissertation. I also wish to thank the remaining members of my committee, Prof. Yuri Fialko and Prof. Samuel Shen, for taking time out of their schedule to discuss my work. Their comments and inputs have been very valuable to this dissertation. I also wish to thank Prof. Steve Constable for introducing me to the Electromagnetic community at the IAMG workshop and sharing his professional network to help me search for potential career opportunities.

Working and studying at Scripps has been a unique experience, more because of its lovely people than the beautiful natural scenes. Thanks first go to my cohorts, including Dallas Sherman, Ekaterina Tymofyeyeva, James Holmes, William Savran, Xiaohua Xu and Zhao Chen, for creating a relaxing and cheerful studying environment. Also, I would like to acknowledge the members of Chinese Community at IGPP as a big family, which helped me feel less homesick. Especially, I would like to thank Qian Yao, Niu Du, Zhao Chen, Kang Wang and Wei Wang for helping me go through thick and thin

at different stages of my life.

I would also like to mention people from other communities outside of Scripps. First, I would like to thank Dr. Zhijun Du, who I worked with during my first internship at Petroleum Geo-Services. Thanks for inviting me to participate in the three-month internship, especially when the industry was in its downturn. In addition, I would like to thank Jan Petter Morten at EMGS, a friend and colleague, for sharing his knowledge and insights about geophysical optimization. Additionally, I wish to thank Prof. Jeffery Ovall, who has patiently helped me grip the idea of goal-oriented error estimation and selflessly shared his computational geometry programs.

I also wish to thank the many people whom I have had the privilege to call friends during my time in San Diego. Five years has been a time full of joy and beautiful memories. In particular, I thank Bing Zhang, Haowei Chen, Li Li, Chao Xu and Jessie Yang for organizing trips, including the day hike to the half dome of Yosemite, the rim-to-rim traverse in Grand Canyon and the backpacking adventure at the lost coast of California, dragging me away from my computers. Their team spirit and endurance have always been refreshing and motivative during the long-haul journey of my Ph.D.

Last but certainly not least, I owe endless gratitude to my parents, Xin'an Zhang and Sudi Sun, who have loved me enough to let me explore. I thank them for bestowing upon me the inspiration and freedom to follow the heart. I would have gone nowhere without their love and support.

The text of Chapter 2, in part, is currently being prepared for submission for publication of the material as it may appear in Zhang, Y., Key, K., Holst, M., Parallel goal-oriented adaptive finite element modeling for 3D electromagnetic exploration, Geophysics, 2017. The dissertation author was the primary investigator and author of this paper.

The text of Chapter 3, in part, is being prepared for submission for publication of

the material. Zhang, Y., Key, K., MARE3DEM: A Three-dimensional CSEM Inversion Based on A Parallel Adaptive Finite Element Method Using Unstructured Meshes. The dissertation author was the primary investigator and author of this paper.

VITA

2012	B.S. in Geophysics, University of Science and Technology of China.
2017	Ph. D. in Geophysics, University of California, San Diego and San Diego State University.

PUBLICATIONS

Zhang, Y., Key, K., Ovall, J., Holst, M., Parallel goal-oriented adaptive finite element modeling for 3D electromagnetic exploration, to be submitted for review for Geophysics.

SELECTED ABSTRACT

Zhang, Y., Key, K., MARE3DEM: A 3D CSEM Inversion Based on A Parallel Adaptive FE Method, AGU, 2016.

Zhang, Y., Key, K., MARE3DEM: A 3D CSEM Inversion Based on A Parallel Adaptive FE Method, SEG, 2016.

Zhang, Y., Forward modeling and inversion for 3D CSEM, 23rd Workshop on Electromagnetic Induction in Earth, Chiangmai, Thailand, 2016.

Zhang, Y., Key, K., A 3D CSEM Inversion Based on A Parallel Goal- oriented Adaptive FE Method, AGU, 2015.

Zhang, Y., Key. K., Parallel goal-oriented adaptive finite element modeling for 3D EM exploration, SEG, 2015.

ABSTRACT OF THE DISSERTATION

Parallel goal-oriented adaptive finite element modeling for 3D electromagnetic exploration

by

Yuxiang Zhang

Doctor of Philosophy in Geophysics

University of California, San Diego, 2017
San Diego State University, 2017

Professor Kerry Key, Chair

Over the past 10 years, both academia and industry collected large amounts of EM data. Compared with the abundance of data, the processing capacity is the bottleneck to have deeper insight into the earth. To increase the 3D processing capacity, this dissertation focuses on developing a 3D EM data processing toolkit, which could connect from data to model, uncovering the conductivity distribution of the seafloor.

The first part of the dissertation employs a parallel goal-oriented adaptive finite element method for 3D electromagnetic modeling. To efficiently discretize the model,

we use the unstructured tetrahedral mesh to accommodate arbitrarily complex 3D conductivity variations. Accuracy of the finite element solution could be achieved through adaptive mesh refinement that is performed iteratively until the solution converges to the desired accuracy tolerance. Refinement is guided by the goal-oriented error estimation approach to generate the optimal mesh, such that accurate EM responses at the locations of the EM receivers could be calculated. To further improve the computational efficiency, our algorithm is parallelized over frequencies, transmitters and receivers. We benchmark the newly developed algorithm by validating the controlled-source EM solutions on a 1D layered model. Furthermore, we employ a 3D model with significant seafloor bathymetry variations and a heterogeneous subsurface to demonstrate the code's ability to model complex features.

In the second part, we introduce the framework for 3D inversion of marine controlled-source electromagnetic (CSEM) data. Our code, named Modeling with Adaptively Refined Elements for 3D EM (MARE3DEM), uses a new variant of the regularized Occam method for the inversion. The forward solver introduced previously serves as the backbone to calculate the model response and jacobians. The forward and inverse meshes are decoupled, such that we could accommodate the size of the inverse problem without sacrificing the accuracy of the forward solution. The sensitivity kernels which describe the change of the responses with respect to the variation of model parameters are efficiently calculated using the adjoint method. We show the reliability and the potential of the inversion algorithm by applying it to the inversion of synthetic marine controlled-source EM data.

Keywords: Numerical solution; Adaptive finite element; high performance computing; 3D Inversion; Marine electromagnetics.

Chapter 1

Introduction

Exploration geophysics is the applied branch of geophysics that uses various physical measurements to probe the shallow and deep interior of the earth. To obtain information about the subsurface of the earth, many geophysical methods have been developed, such as seismic methods, controlled-source electromagnetic methods, magnetotellurics, well-logging and gravity methods. Despite the fact that the governing physics among all these geophysical methods are different, measurement of the earth's properties are all carried out at the surface, in order to detect or infer the presence and position of ore minerals, hydrocarbons, geothermal reservoirs, groundwater reservoirs and other buried geological structures.

Among all the exploration approaches, seismic method is the most popular and widely used one. It is commonly accepted that seismic techniques are extremely powerful and generally applicable. For example, in the oil and gas industries, reflection seismology has been widely applied for obtaining high resolution maps of acoustic impedance contrasts at depths of up to 10 km within the subsurface. Also, it can be applied to crustal studies of the earth structure from the near surface all the way to the Moho discontinuity and beyond, at depths of up to 100 km. However, there are

some situations in which seismic methods fail to answer the geophysical questions. For example, when salt and basalt exists in the underlying geology, the resolution of seismic methods deteriorate, due to the energy scattering effect [Hoversten et al., 2000]. Besides, seismic methods have generally weak sensitivity to pore fluid types and concentrations, especially gas saturations, depending on the rock matrix and depth. Therefore, it is difficult to distinguish among these fluids trapped in the subsurface.

However, the indeterminacy of seismic methods at these scenarios has encouraged the development of electromagnetics (EM) methods, which are techniques for remotely characterizing the electric conductivity, dielectric permittivity and magnetic permeability of geological formations. The physical basis for electromagnetic methods is that the electric and magnetic properties of rocks, minerals, oil and geological structures are widely variable. The knowledge of these electromagnetical properties is effective in inferring the composition, porosity and pore fluid content. For example, the resistivity of an oil reservoir can be 1- 2 orders of magnitude higher than the resistivity of the surrounding water-saturated sediments. Targeting at imaging the resistivity distribution, EM method is sensitive to the large variation of material properties and could be applied to discover potential hydrocarbon reservoirs. Based on these merits, EM methods have also been applied to other areas, such as hydrological modeling, nuclear site evaluations, reservoir characterization and mineral exploration.

Depend on the type of source of the driving energy, marine electromagnetic exploration method can generally be classified into two categories: magnetotelluric method (MT) and controlled source electromagnetic method (CSEM), which have long been used for the oceanic crust and upper mantle studies [Key, 2003, Naif et al., 2013], as well as offshore hydrocarbon discovery [Constable and Weiss, 2006a, Eidesmo et al., 2002].

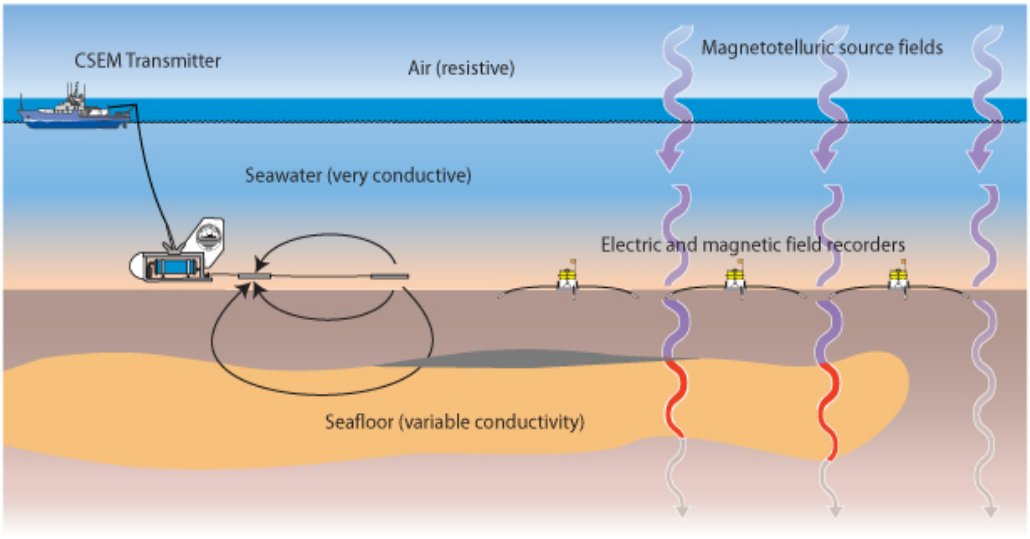

Figure 1.1: EM exploration in the oceans.

1.1 Marine Electromagnetic Exploration

As is seen in Fig. 1.1, for the controlled-source electromagnetic (CSEM) method, a deep-towed dipole antenna generates EM fields that diffuse through the seafloor. The magnetotelluric method uses natural low frequency plane waves generated in the ionosphere to map the broader scale conductivity structure from the seabed to 100's of kilometers into the mantle. Both methods involve an array of seafloor receivers, which record how the electromagnetic wave propagates through the conducting geology. The strength of the electric and magnetic fields recorded by seafloor EM receivers is a function of seafloor conductivity distribution and the transmitter-receiver offset. Therefore, the recorded data in these receivers reflect the physical process, based on which we will be able to invert the subsurface structure of the seafloor.

1.1.1 Controlled-source EM method

Marine CSEM, also referred to as seabed logging [Eidesmo et al., 2002], explores the subsurface conductivity structure by emitting a low-frequency EM wave from a high-

powered source (normally an electric dipole) which is connected to a vessel and towed close to the seabed. The transmitted wave (primary field) interacts with the electrically conductive Earth and induces eddy currents that become sources of a secondary EM field. The two fields, the primary and the secondary one, add up to a resultant field, which is measured by remote receivers placed on the seabed.

The marine controlled-source electromagnetic (CSEM) method is nowadays a well-known geophysical exploration tool in the offshore environment in industry. In most studies, typical operating frequencies of transmitters in CSEM vary from 0.25 to 1 Hz, according to the decaying rule of electromagnetic radiation, which means the penetration depth of the method can extend to several kilometers below the seafloor. The CSEM method is sensitive to reservoir fluids and saturation, and thus may indicate hydrocarbons directly, which makes it a source of data complementary to seismic data for marine enviornment exploration [Constable and Srnka, 2007, Ellingsrud et al., 2002].

1.1.2 Marine Magnetotelluric Method

Magnetotellurics (MT) method is used for inferring the earth's subsurface electrical conductivity from measurements of natural geomagnetic and geoelectric field variation at the Earth's surface. In the magnetotelluric method, the sources are located far away from the exploration site. The exploration area where the receiver is located is in the far-field of the distant source transmitter, so that the incident source field can be approximated as a uniform inducing field or as a plane wave. The period of the Earth's magnetic field ranges between 0.001 and 100,000 seconds and the investigation depth ranges from 300 m below ground with higher frequencies down to 10,000 m or deeper with long-period soundings.

First introduced independently by Japanese scientists Hirayama and Rikitake in the 1940s , the French geophysicist Louis Cagniard in 1953 and Russian geophysicist

Andrey Nikolayevich Tikhonov in 1950, MT is now being widely used in surveys around the world, including hydrocarbon exploration, geothermal exploration, carbon sequestration, mining exploration, as well as groundwater monitoring. Also, with the advances in instrumentation, processing and modelling, MT has become one of the most important tools in deep Earth research.

The development of both the CSEM and the MT method is discussed in the review paper by [Edwards, 2005] and the recent paper by [Key, 2012a].

1.1.3 Physical Problem in Exploration Geophysics

The Maxwell equation mathematically describes how the EM wave propagates through and interact with different mediums in a concise manner. To better comprehend the physical behavior of EM phenomenon, we start from Maxwell's equations in the time domain [Ward and Hohmann, 1988a].

An EM field may be defined as a domain of four vector functions:

$$\mathbf{e}(V/m) - \text{electric field intensity}$$

$$\mathbf{b}(Wb/m^2 \text{ or Tesla}) - \text{magnetic induction}$$

$$\mathbf{d}(C/m^2) - \text{dielectric displacement}$$

$$\mathbf{h}(A/m) - \text{magnetic field intensity}$$

From Faraday's law [Stratton, 2007],

$$\nabla \times \mathbf{e} + \frac{\partial \mathbf{b}}{\partial t} = 0 \tag{1.1}$$

electric fields **e** (V/m) are induced through temporally varying magnetic flux density **b**

(Tesla). The direction of this induced electric field is in the plane which is perpendicular to the direction of the magnetic flux intensity.

According to Ampere's law,

$$\nabla \times \mathbf{h} - \frac{\partial \mathbf{d}}{\partial t} = \mathbf{j} \tag{1.2}$$

the electric field **e**, in turn, generates a magnetic field **h** (A/m) through conduction currents **j** and displacement currents $\frac{\partial \mathbf{d}}{\partial t}$.

The other two Maxwell equations are expressed in terms of the divergence of the magnetic flux density **b** and the electric displacement **d**:

$$\nabla \cdot \mathbf{b} = 0 \tag{1.3}$$

and

$$\nabla \cdot \mathbf{d} = \rho \tag{1.4}$$

where ρ is electric charge density in c/m^3.

Equation 1.1 - 1.4 are the conventional general form of Maxwell's equations. The vector functions (**e**, **b**, **h**, **d**): can be coupled by empirical constitutive relations which reduce the number of basic vector field functions from five to two. Below is the constitutive relations in the frequency domain: (**E**, **B**, **H**, **D** are corresponding functions in the frequency domain)

$$\mathbf{D} = \tilde{\varepsilon}(\omega, \mathbf{E}, \mathbf{r}, t, T, P, ...) \cdot \mathbf{E}, \tag{1.5}$$

$$\mathbf{B} = \tilde{\mu}(\omega, \mathbf{E}, \mathbf{r}, t, T, P, ...) \cdot \mathbf{H}, \tag{1.6}$$

$$\mathbf{J} = \tilde{\sigma}(\omega, \mathbf{E}, \mathbf{r}, t, T, P, ...) \cdot \mathbf{E}, \tag{1.7}$$

where tensors $\tilde{\varepsilon}, \tilde{\mu}$ and $\tilde{\sigma}$ describe, respectively, dielectric permittivity, magnetic permeability and electric conductivity as functions of angular frequency, ω, electric field strength, **E**, or magnetic induction, **B**, position, **r**, time, t, temperature, T, and pressure, P. In the general case, each of these three tensors is complex and, consequently, the phases of **D** and **E**, of **H** and **B** and of **J** and **E** are different.

In problems that arise in CSEM, it is normally assumed that the Earth is heterogeneous, anisotropic and with electromagnetic parameters that are independent of temperature, time and pressure.

To describe the Maxwell's equations in the frequency domain, we could apply one-dimensional Fourier transformation to equation 2.1 and 2.2 using constitutive relations 2.5 and 2.7:

$$\nabla \times \mathbf{E} = -i\omega\mu\mathbf{H} \tag{1.8}$$

and

$$\nabla \times \mathbf{H} - \hat{\sigma}\mathbf{E} = \mathbf{J}^s \tag{1.9}$$

where ω is the angular frequency of the field with assumed time-dependence of the form: $e^{-i\omega t}$, J^s is the vector of the current density of a source, $\tilde{\sigma}\mathbf{E}$ is the ohmic conduction term and $i\omega\tilde{\varepsilon}\mathbf{E}$ is the term that describes displacement currents.

Boundary conditions

Boundary conditions on the vector field functions can be obtained from the integral form of Maxwell's equations:

Normal B: the normal component, B_n, of **B** is continuous across the interface separating medium 1 from medium 2, is written as

$$B_{n1} = B_{n2} \tag{1.10}$$

Normal D: the normal component, D_n, of D is discontinuous across the interface sepa-

rating medium 1 from medium 2 due to accumulation of surface charges whose density is ρ_s, i.e.:

$$D_{n2} - D_{n1} = \rho_s \tag{1.11}$$

Tangential E: the tangential component, E_t, of E is continuous across the interface separating medium 1 from medium 2, i.e.:

$$E_{t1} = E_{t2} \tag{1.12}$$

Tangential H: the tangential component, H_t, of H is continuous across the interface separating medium 1 from medium 2 if there are no surface currents, i.e.:

$$H_{t1} = H_{t2} \tag{1.13}$$

Normal J: the normal component, Jn, of J is continuous across the interface separating medium 1 from medium 2, i.e:

$$J_{n1} = J_{n2} \tag{1.14}$$

These boundary conditions stated above need to be accommodated during the discretization process. Otherwise numerical error will arise.

1.2 Basic Theory of 3D Electromagnetic Modeling

Above is the continuous form of the Maxwell equations. To numerically solve the diffusion equations for arbitrary models, we need to discretize the equation using the numerical methods [Hohmann, 1988, Jin, 2014].

1.2.1 Opportunities and Challenges for Large Scale 3D Modeling and Inversion

Along with the rapid development of instrumentation [Constable et al., 1998] and data acquisition techniques, many innovations in the data processing have also been motivated. These newly developed modeling and inversion methods have been applied to various datasets both in 2D and 3D [Börner, 2009, Key, 2012b].

In the 2D case, the modeling and inversion toolkit has been successfully applied to natural resource exploration and tectonic investigation [Darnet et al., 2007, Naif et al., 2013, Du, 2014]. For example, [Du, 2014] uses seismic guided EM inversion to provide valuable information on reservoir characteristics in the North Sea region. Also, [Naif et al., 2013] uses seafloor magnetotelluric data to image the electrical conductivity of the lithosphere and asthenosphere boundary beneath the edge of the Cocos plate offshore of Nicaragua, discovering either partial melting or a mantle dehydration boundary as explanations for high conductive structure. The application of EM techniques in the 2D situation has proved to be effective and successful. However, in many 3D situations, the use of 2D or even 1D processing schemes fails to take the 3D structure into consideration, which naturally leads to incomplete or false interpretations. Therefore, there is a real and increasing need for a reliable 3D EM data processing toolkit to deal with 3D data in complex geological environments. However, due to the complex nature and the large volume of the 3D dataset, extracting and processing has proven to be a formidable computational problem. In other words, to deal with these new industrial scale applications, where huge amount of data have been collected, it is very important to develop efficient and robust 3D inversion algorithms for a better understanding of the real geology in 3D.

To tackle the huge computational demands of 3D EM inversion, the first and

most important step is to solve for the forward problem with high efficiency. The crucial role of an efficient forward solver in the inversion scheme is twofold. First, forward calculation needs to calculate millions of field unknowns. The modeling grids designed to approximate large-scale complex geologies, which include structures with complicated shapes and big contrasts in conductivities, are usually enormous. Moreover, in order to obtain realistic subsurface images of huge Earth, normally there is a need to solve hundreds of forward problems within an inversion algorithm. Since the numerical engine driving those inversion algorithms is mostly dominated by the forward operator, the developments in 3D modeling techniques will significantly benefit the development of inversion strategies. Hence, it shall be emphasized that 3D EM inversion needs a fast, accurate and reliable 3D EM forward modeling engine in order to improve its own efficiency and thus be realistic for practical use in industry.

1.2.2 Forward Problem

As is mentioned, in order to create an efficient, reliable and practical 3D electromagnetic inversion, the first and most important step is to have a 3D electromagnetic modeling code that is highly accurate, robust and efficient.

EM field modeling on a 3D volume of the Earth has been an active research topic in the geophysical community for several decades. It involves a numerical solution of the diffusive Maxwell's equations in heterogeneous anisotropic electrically conductive media. In order to obtain a numerical solution of the partial differential equations, it is necessary to discretize the equations, which are, by nature, continuous, using some discretization technique. The integral equation method ([Raiche, 1974, Avdeev et al., 2002, Zhdanov et al., 2006]) was predominant at the beginning. It is numerically efficient, but it cannot deal with large conductivity contrasts and involves large, dense matrices. Then comes the finite difference method ([Streich, 2009a, Newman and Alumbaugh, 2002]

and recently followed by the finite element methods ([Mitsuhata and Uchida, 2004, Key and Weiss, 2006a, Nam et al., 2007, Key and Ovall, 2011b]) and the finite volume method ([Haber et al., 2000, Constable and Weiss, 2006b, Haber et al., 2007]).

The most commonly used ones are the finite difference (FD) and the finite element (FE) methods. Due to relatively simple implementation and maintenance, the FD method have been extensively used in solving three dimensional modeling problems in the time and frequent domain. Since [Ward and Hohmann, 1988b] presented a 3D FD algorithm which discretized the first-order Maxwell's equation systems on a staggered grid, staggered grids introduced by [Yee et al., 1966] have become popular for simulating the EM wave fields among many authors ([Druskin and Knizhnerman, 1994, Commer and Newman, 2008]). [Haber and Heldmann, 2007] developed an OcTree discretization of Maxwell's equations in the quasi-static regime, which would allow local adaptive grid refinement and the utilization of a multigrid solver. Commonly during the modeling process, the electric conductivity, the vector EM field functions and Maxwell's differential equations are approximated by a rectangular 3D mesh. This transforms the original problem to a resultant system of linear equations, which is a large, sparse, complex and symmetric matrix. Afterwards, we could solve the system using either iterative or direct solvers.

Despite the simple implementation, FD method supports only structured rectangular grids, which may be a substantial limitation in many situations. For example, complex terrains with large topographic or bathymetric variations cannot be accurately modeled with rectangular elements and can impart a strong influence on the measured data ([Schwalenberg and Edwards, 2004, Li and Constable, 2007]). Even though we could employ fine cells to incorporate complex geological structures into the finite difference model, these elongated cells will have to be extended to the model boundary, which not only increases the computational burden of the problem, but also deteriorates the

convergence behavior when using an iterative solver. Also, local grid refinements are not supported and, consequently, it is not possible to have a finer mesh at some place without increasing the overall computational requirements. Furthermore, it tends to underutilize the decaying character of the electromagnetic fields far away from the sources.

A well-known solution to these discretization difficulties is to employ the finite element method which uses an unstructured grid. The finite-element (FE) method has long been used in applied mathematics and solid mechanics. In geophysics, however, it has been employed for only a few decades. Many FE-based implementations of EM modeling have been applied to EM geophysical problems ([Key and Weiss, 2006b, Franke et al., 2007, Key and Ovall, 2011b, Schwarzbach and Haber, 2013]). The unstructured grid can readily conform to highly complex geological features, such as seafloor topography and stratigraphic horizons. In addition, the ability to efficiently discretize multiple-scale structures, including tiny grid elements required for near-surface features and deep thin hydrocarbon reservoirs is another key benefit. Moreover, the accurate representation of arbitrary complex and irregular geometries offered by the finite element method is important to avoid misleading artifacts in images. The FE method also supports local mesh refinements, which allow a higher solution accuracy without increasing the overall computational requirements. Therefore, it is possible to have small elements just in the places where a better resolution is required and gradually increase the size of the element to the model boundaries.

Moreover, on top of the adaptive mesh refinement, posterior error estimation seeks to increase the solution accuracy iteratively. In each iteration, a subset of elements will be selected for refinement based on an estimation of the solution accuracy and their influence to the solution error. Such methods fall under the category of goal-oriented error estimation [Estep et al., 2006, Ovall, 2006], which offers an efficient and optimal way to refine the mesh. Such methods have great potential since they can be used to

automatically compute an efficient and accurate model discretization, without requiring user's intervention or even expert knowledge about a particular problem.

However, this approach is still not as widely used as finite difference and a major obstacle for its broader adoption is that the standard nodal FE method does not correctly take into account all the physical aspects of the vector EM field functions. More specifically, the nodal FE method does not allow the discontinuity of the normal component of the electric field at material interfaces. Also, node-based finite elements are not divergence free, because of which some spurious solution may exist.

One solution to the boundary problems is to employ the specialized vector (edge) elements, which are used in some recent approaches for CSEM modeling. In the case of edge elements, the unknowns are the tangential components of the electric field along the edges of elements. Consequently, these elements permit the normal component of the electric field to be discontinuous across material interfaces. Also, vector elements are divergence free by construction and hence cannot support spurious modes. Edge elements not only solve both problems, but also support the direct vector field formulation.

To use the finite element scheme to solve a numerical system, another challenge is the robust grid generation. Before the emerging of the robust mesh generation toolkit, such as Tetgen [Si, 2015] and FETK [Holst, 2001], only few practical 3D CSEM inversion code based on finite difference method were available within the community. With the help of the newly developed computational geometry library, during the finite element modeling process, users only need to define the boundaries among different layers and the mesh generation engine will discretize the model efficiently.

With the help of unstructured model parameterization, automatic adaptive mesh refinement and high performance computing resource, 3D EM modeling based on finite element becomes more feasible and practical. Based on the successfully development of the forward solver, several inversion engines have also been available within the

EM community. For example, [Schwarzbach and Haber, 2013] developed finite element based inversion for time-harmonic emectromagnetic problems. [Grayver, 2015] applied adaptive finite element method for 3D magnetotelluric inversion.

1.2.3 Inverse Problem

The inverse problem is essentially an optimization problem, which can be generalized as searching for a set of model parameters which could fit the observed data. For geophysical inverse problem, from the observed data measured along the surface of the model, we seek to recover the model parameters for the entire domain. This procedure of parameter reconstruction is referred to as solution of the inverse problem, which can be formulated as [Zhdanov, 2015, Menke, 1984]

$$\mathbf{m} = F^{-1}(\mathbf{d}) \tag{1.15}$$

To solve the problem, there are two classes of methods: deterministic and stochastic approaches. Both approaches need to deal with incomplete data and the data uncertainty [Parker, 1994]. Ideally, we could only reconstruct the true model when the number of observations are infinite and the data are uncontaminated from noise. However, the real situation is far from ideal. As the British statistician George Box said, 'essentially, all models are wrong, but some are useful'. In this sense, we could not recover the real model, but only generate a model which could feasibly explain the observed data.

To find an optimal set of model parameters from the limited set of observed responses $\mathbf{d}$, the inverse problem as defined by equation 1.15 needs to be solved. The non-linearity of the forward operator $\mathbf{F}$ or inverse operator $\mathbf{F}^{-1}$ requires that the forward problem be solved iteratively upon linearization of $\mathbf{F}$. Apart from non-linearity, the inverse operator is also ill-posed. The ill-posedness results from the fact that the inverse

problem is typically under or mixed determined. More specifically, there are more model parameters than data or certain parts of the model are not constrained by the data, whereas other model regions are over-determined [Menke, 1984]. In either case, additional model regularization, e.g. smoothness constraints, need to be employed as a remedy. The basic motivation for seeking smooth models is not to be misled by features that appear in the model, but are not essential in matching the observations. [Constable et al., 2012]

The deterministic approach seeks a single model which could reduce the misfit to a certain threshold, according to the EM measurements. Many packages based on the deterministic method have been develop and now are available within the EM community. For example, [Newman and Commer, 2005] developed a conjugate-gradient framework to invert transient electromagnetic (TEM) data sets. [Key, 2016] developed a Gauss-newton based 2D anisotropic inversion of magnetotelluric (MT) data and frequency-domain controlled-source electromagnetic (CSEM) data.

Besides, bayesian stochastic framework and Markov Chain Monte Carlo sampling methods may offer a clear alternative to deterministic inversion methods for estimating the resistivity of the subsurface along with the associated uncertainties. The papers of [Chen and Dickens, 2009] provide a good overview of the methods for reservoir estimation problems. Recent paper by [Ray et al., 2014] uses a reversible-jump Markov chain Monte Carlo method to sample the Bayesian posterior model probability density function of 2D seafloor resistivity as constrained by marine controlled source electromagnetic data. Stochastic inversion could provide a posterior distribution of the model parameters, making it a good tool to estimate the model uncertainties.

For EM data processing, the trend nowadays is to develop robust and efficient packages for 3D data. In 3D environments, 2D interpretation of data is a standard practice due to its short processing times, as well as the fact that there are very few efficient 3D EM modeling and inversion schemes. However, in many 3D cases, the use of 2D

interpretation schemes may give images in which appear some artifacts that could lead to misinterpretation. Therefore, there is an increasing need for reliable and fast techniques of interpretation of 3D EM data sets acquired in complex geological environments. Also, 3D inversion could include broadside data into the inversion, resulting better imaging capacity [Jing et al, 2008].

The challenge for 3D processing not only comes from the larger 3D modeling domain, but also from the huge data volume. For example, present-day exploration with the CSEM technology in searching for hydrocarbons in highly complex and subtle offshore geological environments needs to employ up to hundreds of transmitter-receivers arrays, which operate at different frequencies and have a spatial coverage of more than 1000 km^2 ([Commer and Newman, 2008]). Those huge data sets exert more computational requirement for the inversion scheme. Even with the very high level of modern computing technology, the proper numerical solution of the 3D inverse problem still remains a very difficult and computationally extremely demanding task.

With the challenges and opportunities, this Ph.D project focuses on developing a numerical method for 3D CSEM modeling and inversion in the frequency domain.

Chapter 2

Goal-oriented adaptive finite element modeling for 3D Electromagnetics

2.1 Introduction

Electromagnetic (EM) geophysical methods are techniques for remotely characterizing the electrical conductivity distribution of geological formations, which can be used to detect or infer the presence and position of ore minerals, hydrocarbons, geothermal reservoirs, groundwater, reservoirs and other geological structures. As the foundation of the governing physics, Maxwell equation mathematically describes how the EM wave propagate through and interact with different mediums in a concise manner. However, in practice, we have to find the trade offs between the simplicity of continuous physics and the discrete numerical representation, considering model discretization, numerical approximation, solution accuracy, efficiency and the complication of the geology.

Speaking of numerical simulation for the Electromagnetic process, the commercial investment in marine EM exploration has motivated many innovations during the past decade [Börner, 2009, Key, 2012b]. In particular, forward modeling method using finite

element method went through a period of rapid growth in recent years due to the emerging of computation geometry software and industrial's substantial investment for using EM techniques as a valuable tool for characterizing offshore hydrocarbon reservoirs.

Traditionally, finite difference methods [Mackie et al., 1993, Haber et al., 2000, Weiss and Newman, 2002, Streich, 2009b] have been extensively used in solving three dimensional modeling problems in the time and frequent domain. Based on the structured grid, such as rectangle, model could be discretized without the need of specialized software and the resulting grid permits a convenient approximation of the spatial derivatives. E.g. Staggered grid introduced by [Yee et al., 1966], has been a common practice for simulating EM response among many authors. However, finite difference method supports only structured rectangular grids, which may have several major drawbacks to accommodate complex terrains with large topographic or bathymetric variations [Key and Weiss, 2006b]. For example, small scale elongated rectangle elements will have to be used to describe the highly variable topography. Those fine cells will propagate horizontally and vertically throughout the entire model, increasing the inefficiency to characterize multi-scale structures.

A well-known solution to these discretization difficulties is to use the unstructured grids, which can readily accommodate highly complex geological features, such as seafloor topography and stratigraphic horizons. Since [Coggon, 1971] first applied FE techniques to 2D DC resistivity problems using linear triangular elements, FE method based on unstructured element has been extensively explored by many authors [Wannamaker et al., 1987, Key and Ovall, 2011a, Grayver and Kolev, 2015] to solve EM modeling problems. Since tiny grid elements required for near-surface features or deep thin hydrocarbon reservoirs can grow with distance, small elements do not necessarily extend to the model boundaries. Therefore, unstructured grids are also highly suitable for modeling multiple scale structures. However, for arbitrarily complex models it is

difficult to construct an numerically accurate and optimal mesh. Due to the fact that EM observations are typically made at a few discrete points, the solution only needs to be accurate at these discrete locations. Instead of having a mesh to be accurate globally, adaptive mesh refinement combined with a posterior error estimation method provide us a automatic way to generate the optimal mesh with minimal number of elements. Although the posterior estimation approach has long been used in the applied math and engineering communities, they have only recently been applied to EM geophysical problems [Key and Weiss, 2006b, Key and Weiss, 2006b, Franke et al., 2007, Li and Key, 2007, Key and Ovall, 2011a, Ren et al., 2013, Grayver and Kolev, 2015].

Among posterior methods [Ainsworth and Oden, 1997], goal-oriented estimation approaches based on either post processing of the finite element solution or the computation of an auxiliary solution would overcome the complicated nature of electromagnetic coupling and offers an optimal mesh density distribution. E.g. [Ren et al., 2013] calculated the tangential and vertical discontinuity of the field based on the solution to create a posterior error estimation for Magnetotellurics modeling. In the framework of goal-oriented estimation [Becker and Rannacher, 2001, Estep et al., 2006, Ovall, 2006, Bank and Ovall, 2007], the global contribution to the local error, known as the pollution effect [Nitsche and Schatz, 1974] are taken into account by using a sensitivity functional that measures how the error in one portion of the model corrupts the solution at the regions of interest. Refinement only occurs where the solution is inaccurate and where that inaccuracy corrupts the solution at the receivers' locations.

The goal-oriented error estimation approach has great potential since they can be used to automatically compute an efficient and accurate model discretization, without requiring user intervention or even expert knowledge about a particular problem. Besides, the optimized mesh generation results in faster run-times with accurate solution, as well as the ability to handle a larger system given a limited memory capacity.

Aiming to overcome the difficulties encountered with traditional 3D modeling techniques using rectangular grids with high efficiency and accuracy, we uses the adaptive refinement guided by two different goal-oriented error estimation approaches: residual based error estimation and hierarchical basis error estimation approach. In the residual based method, we define the error functional in the dual problem as the normalized element-wise residual of the field. Since the lowest order Nédélec basis function breaks down the continuity constrain on the normal component of the total current and the tangential component of the magnetic field across the interior faces, to quantify such discontinuity, we calculated the volumetric residual and the face jump residual from both the primary and dual solution [Zhong et al., 2012]. The estimated error for each element is then weighted by its influence to the solution at the measurements sites. As a highlight of this method, to drive down the error more efficiently, different forms of error functional have been tested as the sourcing term of the dual problem. The current error function is optimal among several in-house error functions. Another novel part in our approach is the implementation of the hierarchical basis error estimation. In this case, the error of finite discretization is projected to a higher order space, which consists of quadratic face basis functions. The hierarchical basis approach is beneficial, since the underlying physics are applied throughout the entire model domain during the error estimation computations, rather than the operation for the piecewise residuals. In both method, we starting with a coarse model discretized by a grid of tetrahedral elements with the a priori refinement applied to the receivers' region. Afterwards, the adaptive methods seek to increase the solution accuracy by iteratively refining the grid. In each iteration, a subset of elements will be selected based on an estimation of their contribution to the solution error and be refined by creating new smaller elements in these regions. Such dynamic approach for grid generation will finally result in the optimal mesh distribution where accurate response could be calculated.

In the following sections, we review the total field formulation for 3D CSEM and introduce the corresponding FE solution. We then describe the goal-oriented error estimation scheme, followed by presenting the adaptive refinement procedure. To verify the accuracy of the method, we study the convergence behavior based on a 1D model by comparison with an simi-analytical code [Key, 2009]. Furthermore, to demonstrate the performance of our parallel data domain decomposition approach [Key and Ovall, 2011a], we test the code in a 3D case that includes significant seafloor bathymetry variations and a heterogeneous subsurface on a medium-scale computing cluster.

2.2 Finite Element Analysis

We implement the forward solver on unstructured tetrahedral meshes using edge elements. Unstructured meshes are not only capable of representing complex geometry, but also reduce the overall problem size. Therefore, the size of the system of linear equations arising from the forward problem is such that direct methods for its solution using a sparse matrix factorization become feasible.

We start by presenting the coupled differential form of Maxwell equations which describe the electromagnetic phenomenon. Consider the isotropic 3D electrical conductivity model $\sigma(x,y,z)$, some time-harmonic varying electric sources $\mathbf{J}^s$ and magnetic sources $\mathbf{M}^s$ being imposed in a given bounded computational domain Ω.

Assuming the time variation $e^{i\omega t}$ with frequency ω, the governing equations for the frequency domain electric field $\mathbf{E}$ and magnetic field $\mathbf{H}$ are

$$\nabla \times \mathbf{E} = -i\omega\mu\mathbf{H} \tag{2.1}$$

and

$$\nabla \times \mathbf{H} - \hat{\sigma}\mathbf{E} = \mathbf{J}^s \tag{2.2}$$

where μ is the magnetic permeability and ω is the angular frequency. The quantity $\hat{\sigma}$ is the admittivity $\hat{\sigma} = \sigma + i\omega\varepsilon$, where the dielectric permittivity ε is included for completeness. However, for low-frequency geophysical applications the imaginary term has a much smaller magnitude than the real conductivity σ and therefore is typically neglected [Ward and Hohmann, 1988b]. Eliminating the magnetic field strength from Faraday's law (Equation 2.1) and Ampere's law (Equation 2.2), the coupled system is transferred into a curl curl equation of the electric field

$$\nabla \times \mu_r^{-1} \nabla \times \mathbf{E} + (i\omega\mu_0\sigma - \omega^2\mu_0\varepsilon)\mathbf{E} = -i\omega\mu_0\mathbf{J}^s \tag{2.3}$$

Since a similar equation can be derived for the magnetic field $\mathbf{B}$ due to EM duality, we only discuss the application to the electric field equations for brevity. Equation 2.3 describes that the imposed source $\mathbf{J}^s$ generates the frequency domain electric field $\mathbf{E}$ inside of this bounded domain Ω. To guarantee the uniqueness of the solution, the dirichlet boundary condition is enforce on the surface $\partial\Omega$ as

$$\hat{n} \times \mathbf{E} = 0 \tag{2.4}$$

where $\hat{n}$ is the outward pointing unit normal vector on $\partial\Omega$.

2.2.1 Weak formulation of Electric Field Problem

Solution to equation 2.3 using 3D tetrahedral finite elements are well described in [Monk, 2003], though we give a brief explanation below in order to introduce notation and certain relevant concepts. Taking the vector dot product of equation 2.3 with a vector basis function in the H_0(curl, Ω) space, applying the first vector Green's identity and integrating by parts, we could arrive at the weak formulation of eq. (3) and (4) which is

stated thus: Find $\mathbf{E} \in H_0(curl, \Omega)$ such that

$$B(\mathbf{E}, \mathbf{v}) = f(\mathbf{v}) \quad \text{for all} \quad \mathbf{v} \in H_0(curl, \Omega) \tag{2.5}$$

where, the Sobolev space defined by $H(\text{curl}, \Omega) = \{ \mathbf{v} \in [L^2(\Omega)]^3 : \nabla \times \mathbf{v} \in [L^2(\Omega)]^3 \}$ is consisted of complex-valued functions which are square-integrable and whose first-order curl are also square-integrable. The solution space $H_0(\text{curl}, \Omega) = \{\mathbf{v} \in H(\text{curl}, \Omega) ; \mathbf{v} \times \hat{n} = 0 \text{ on } \partial \Omega\}$ consist of functions which vanish on the boundary in the sense of trace [Evans, 1998].

The notation $\bar{v}$ denotes the component-wise complex conjugate of a vector v here and elsewhere. The nature norm of the space $H(\text{curl}, \Omega)$ is defined by

$$||\mathbf{v}||_H^2 = ||\mathbf{v}||_{[L^2(\Omega)]^3}^2 + ||\nabla \times \mathbf{v}||_{[L^2(\Omega)]^3}^2 \tag{2.6}$$

The detailed expression of the hermitian bilinear form $B(\mathbf{E}, \mathbf{v})$ and the source inner product term $f(\mathbf{v})$ is shown in equations 2.7 and 2.8.

$$B(\mathbf{E}, \mathbf{v}) = \int_\Omega (\mu_r^{-1} \nabla \times \mathbf{E}) \cdot (\nabla \times \overline{\mathbf{v}}) + i\omega\mu_0 \sigma \mathbf{E} \cdot \overline{\mathbf{v}} dV \tag{2.7}$$

$$f(\mathbf{v}) = -\int_\Omega i\omega\mu_0 \mathbf{J}_s \cdot \overline{\mathbf{v}} dV \tag{2.8}$$

2.2.2 Finite Element Approximation

To discretize the equations, the infinite dimensional space H_0 is replaced by a finite dimensional function space H^T, which consists of the lowest order Nédélec basis function [Nédélec, 1986, Jin, 2014]. One merit for using edge basis functions is that the continuity of the tangential components are automatically satisfied. The normal component can therefore be different at the interface of different media.

For model discretization, the meshes will be constructed in a way that respects the underlying geological structures, using a family of tetrahedral elements $\mathcal{T} = \{\mathcal{T}_n\}_{n \in N_t}$. As the total number of tetrahedra(N_t) increase, $\mathcal{T}$ will be better suited for approximating $\mathbf{E}$. Although the electric conductivity varies throughout the model, it is assumed to be constant inside of each element.

The global Nédélec finite element space is defined by

$$H^T = \{\mathbf{v} \in H^1 : \mathbf{v}|_\tau \in [P_1(\tau)]^2 \quad \text{for each} \quad \tau \in \mathcal{T}_n\} \tag{2.9}$$

In other words, H^T refers to the space of piecewise-linear functions used for the finite element solution. $P_k(\tau)$ defines the space of polynomials in three variables of total degree no greater than k on each elements. A discrete version of equation 2.5 is stated as: Find $\mathbf{E}^T \in H^T$, such that

$$B(\mathbf{E}^T, \mathbf{v}) = f(\mathbf{v}) \quad \text{for all} \quad \mathbf{v} \in H^T \tag{2.10}$$

To complete the numerical form of the linear equations system, we map the stiffness matrix of each tetrahedral to the global stiffness. Since connectivity of the edge in the mesh is locally supported, this mapping will result in a global stiffness matrix with significant sparsity. For better memory efficiency, we employ the compress sparse row format to store the sparse matrix. We use LU decomposition to solve the resulted N $\times$ N equations system, where N is the number of interior edges in $\mathcal{T}$. Once the system is solved, the electrical field can be interpolated by the combination of the coefficients and the corresponding basis functions, according to equation 2.11.

$$\mathbf{E}^T(\mathbf{r}) = \sum_{i=1}^{6} E_i \mathbf{v}_i(\mathbf{r}) \tag{2.11}$$

2.2.3 Meshing

Mesh Generation: At the very beginning of solving a finite element based boundary value problem, the 3D model domain must be discretized into a mesh of non-overlapping polyhedral elements. Meshing is a very important part of the modeling process, since the quality of a mesh greatly affects numerical accuracy of the FE solution.

In order to carry out the numerical tests, which will be presented in a later session, I used Tetgen, a mesh generation software, to create the required meshes. Users only need to define the model boundaries and the internal interfaces of the model. The mesh generation engine then discretizes the model using tetrahedras to accommodate very irregular and complex geometries. In EM modeling, it is not necessary to create a fine mesh over the whole domain. On the contrary, it is enough to make local mesh refinements in the regions where field gradients are large, as well as in some parts of the domain where it is preferable to obtain a solution of higher accuracy. Therefore, the meshes that I have created for the tests have some a priori refinement in such places close to the source or receivers. At the same time, at distances of a few skin depths, sizes of tetrahedra can be quite large and keep growing towards the computational boundaries. A series of experiments have shown that such mesh generation strategy minimizes the total number of elements in the mesh and improves the quality of the numerical solution.

2.2.4 Numerical Computation

From the numerical computation perspective, the execution of the program mainly consists of the following steps:

Step 1: Input files definition. In this step, the program has to read in the model geometry, as well as the information about sources and receivers for a problem. Therefore, it is necessary to create some files that contain the frequency, number and locations of the

sources and receivers, as well as the internal and external boundaries which separate each regions. Since we will have the a priori mesh refinement, we need to define the desired element size at the source and receivers' location. The program will read in these files, in order to prepare the discretized mesh for modeling. The internal computational geometry subroutines will assemble the geometric information into tables which contains element definition and neighbor definition. Element definition means specification of the global edge indexes associated with each element. Also, neighbor definition will specify the global index of the neighboring element with respect to the centering elements.

Step 2: Stiffness matrix calculation. Substitute the element basis functions into the weak form of the primary problem and transform the integrals into a form appropriate for numerical evaluation. The integrals have been evaluated numerically using the Gauss quadrature rule of integration. Evaluate the stiffness matrix for each element and assemble the terms into the system equations. The resultant system equations have the stiffness matrix in which most of the terms are zero, which means that the matrix is sparse. The sparsity of stiffness matrix is determined by the mesh connectivity. The sparseness of the stiffness matrix is an important characteristic of the FE method, making it feasible and economical to solve very large problems.

Step 3: Boundary conditions integration. For the boundary elements, we need to apply the dirichlet boundary conditions to the system equations. Once the boundary is applied to the model, the numerical solution will become unique. The resulting stiffness matrix is large, sparse and complex in value. Therefore, we use the compressed sparse format to store and manipulate the stiffness matrix for efficiency.

Step 4: Solve the equations system. There are generally two categories of methods to solve the system: direct method and iterative method. Currently, we use LU decomposition to solve for the solutions. The benefit for employing direct solver is that we could reuse the factorization result for multiple transmitters, as well as the

dual problems, which we will define in the next session. In terms of iterative solver, the condition number of stiffness matrix strongly depends on the particular problem with many factors affecting it, for example high conductivity contrasts in the model or big element size ratios in unstructured grids. Therefore, preconditioning is important to expedite the convergence of the iterative solver. For our previous and current work on iterative solver, we will cover that in the last chapter.

2.3 Goal-oriented Adaptive Refinement

It is well known from classical error analysis theory of the finite element method [Brenner and Scott, 2008] that once the global mesh density satisfies a certain level, the accuracy of the finite element solutions are strongly affected by the local mesh density. This suggests that global refinement techniques might not only increase the number of unknowns and hence the computational cost, but also they may not efficiently improve the accuracy of numerical solutions. Instead of refining the mesh globally, the optimal mesh refinement pattern is controlled by the nature of the geophysical application. Since geophysical observations are typically made at only a relatively few discrete points, the solution only needs to be accurate at these locations. In this case, accurate responses at the sensor's locations can usually be accomplished with a much sparser optimal mesh using the adaptive refinement approach.

In practice, typically, there are two approaches for adaptive refinement, which are the goal-oriented adaptive method and the non-goal oriented adaptive approach [Oden and Prudhomme, 2001]. Although the non-goal oriented one is easier to implement, it will lead to dense meshes in some areas which do not contribute to the accuracy of the solutions(Ren et al., 2013). However, the goal-oriented approach could enforce the efficient refinement of the subdomain in areas of interest by targeting at those elements

where the inaccuracy of the solution corrupts the response at the possibly distant EM receivers. Therefore, to develop an accurate finite element code with a low computation cost, we employed the goal oriented adaptive refinement technique, which offers a way of numerically detecting global contributions to the local error in regions of interest and driving adaptivity accordingly. To measure the global contribution to the local error, our first goal-oriented error estimation method uses a sensitivity functional to measure how the error in one portion of the model corrupts the solution at the regions of interest, an effect referred to as pollution [Oden and Prudhomme, 2001]. Instead of globally decreasing errors of the electric fields, it targets decreasing the error of a linear functional G(E) of the local electric field. As a result, refinement only occurs where the solution is inaccurate and where such inaccuracy corrupts the solution at the receivers' locations. Therefore, an optimal mesh density distribution could be reached to ensure accurate solutions at receivers' location.

For EM geophysics, an accurate solution is only required at discrete points in the model where the electric and magnetic sensors are deployed. In this case, the goal of obtaining accurate responses at the sensors' locations can usually be accomplished with a much sparser mesh than required when a globally accurate solution is desired. Such locally-accurate approximations might be very inaccurate in other parts of the domain, provided such errors in the far field do not adversely affect the local approximations too strongly. This pollution effect [Oden and Prudhomme, 2001] suggests that the naive approach of refining only the region of interest will not necessarily result in good approximations. In fact, it can be clearly seen in some cases to be unable to reduce local error at all beyond a certain point [Ren et al., 2013]. Therefore, a way of numerically detecting global contributions to the local error in regions of interest, and driving adaptivity accordingly, provides a much better plan for efficiently reducing these local errors. The goal of assessing and efficiently reducing error in targeted regions fits

within the larger framework of functional error estimation and goal-oriented adaptivity [Giles and Süli, 2002, Pierce and Giles, 2006, Ovall, 2006, Estep et al., 2006].

2.3.1 Dual Problem Formulation

The purpose of a goal-oriented error estimator is to reduce the size of the functional error $|G(\mathbf{E}-\mathbf{E^T})|$. In other words, the goal is to reduce the error in the quantity of interest G($\mathbf{E}$), rather than the global error in $\mathbf{E}$. Given a functional G, the associated dual problem is stated as

$$B(\mathbf{v},\mathbf{D}) = G(\mathbf{v}) \quad \text{for all} \quad \mathbf{v} \in H_0(curl,\Omega) \tag{2.12}$$

According to equation 2.12, the key relationship for the dual functional error $G(\mathbf{e})$ is

$$G(\mathbf{e}) = G(\mathbf{E}-\mathbf{E^T}) = B(\mathbf{E}-\mathbf{E^T},\mathbf{D}) \tag{2.13}$$

Equation 2.13 shows that the dual solution $\mathbf{D}$ could be thought of as a sensitivity term for the primary error $\mathbf{E}-\mathbf{E^T}$, which serves to weight such error according to its influence on the dual functional G($\mathbf{e}$). This idea has been explored and successfully applied to EM geophysical problems [Key and Weiss, 2006b, Key and Ovall, 2011a, Ren et al., 2013].

We then define $\mathbf{d} = \mathbf{D}-\mathbf{D}^T$ as the error of the dual solution $\mathbf{D}$ and $\mathbf{e} = \mathbf{E}-\mathbf{E}^T$ as the error for the primary solution $\mathbf{E}$. The error functional $G(\mathbf{e})$ could be expanded as

$$\begin{aligned} G(\mathbf{e}) &= B(\mathbf{E}-\mathbf{E^T},\mathbf{D}) = B(\mathbf{E}-\mathbf{E^T},\mathbf{D^T}+\mathbf{d}) \\ &= B(\mathbf{E}-\mathbf{E^T},\mathbf{D^T}) + B(\mathbf{E}-\mathbf{E^T},\mathbf{d}) = B(\mathbf{e},\mathbf{d}) \end{aligned} \tag{2.14}$$

where $B(\mathbf{E}-\mathbf{E^T},\mathbf{D^T})$ equal to zero because of Galerkin orthogonality [Jin, 2014]. We define the generic form of local element error indicator, using Cauchy-Schwartz inequality

[Hughes, 2012]

$$|G(\mathbf{e})| = |B(\mathbf{e},\mathbf{d})| \leq \sum_{n=1}^{N_t} |B_\tau(\mathbf{e},\mathbf{d})| \leq \sum_{n=1}^{N_t} \eta_\tau^e \eta_\tau^d \tag{2.15}$$

where η_τ^e is defined as the primary error which describe the inaccuracy of the solution of each element. The dual error η_τ^d presents the global influence to the solution at place of interest. The final error indicator for each element is a combination of these two with the dual error serves as a weight to the primary error. In the following session, we will present two different method to calculate the element-wise error indicator.

2.3.2 Residual Based Error Estimation

A critical part of this method is the choice of an appropriate dual functional G($\mathbf{v}$), which measures the error in a functional sense. E.g. in Ren's paper, G($\mathbf{E}$) is chosen to be the averaged value of the electric field over the measuring subdomains. In our case, we define G($\mathbf{v}$) in a discontinuous subdomain which contains receivers, shown in equation 2.16

$$\begin{aligned} G_k(v) = \frac{1}{|\alpha_k| \|\nabla \times \mathbf{E^T}\|^2_{L^2(\Omega_k)}} \Big(& \int_{\Omega_k} (f - \beta \mathbf{E^T}) \cdot \overline{\mathbf{v}} \\ & - (\alpha \nabla \times \mathbf{E^T}) \cdot (\nabla \times \overline{\mathbf{v}})\, dV \\ & - \int_{\partial\Omega_k} ((\alpha \nabla \times \mathbf{E^T}) \times \hat{n}) \cdot \overline{\mathbf{v}}\, dS \Big) \end{aligned} \tag{2.16}$$

We define the error functional G as the relative value of the volumetric residual summing over the face jump residual. The relative weighting is appropriate for EM geophysics applications, since the sources of relative error are typically more significant than the absolute value of the sensor noise floors. Besides, the field of a CSEM transmitters can exhibit several orders of magnitude variations across the EM receivers array. If the error functional only considered the absolute error, the adaptive procedure will be limited to the

region with large field amplitudes while neglecting smaller amplitude regions. Therefore, the relative error functional will be more advantage, since it operates independently of the absolute field amplitude.

The discrete solution $\mathbf{D^T}$ to the dual problem is calculated using the functional error G as a sourcing function.

$$B(\mathbf{v},\mathbf{D^T}) = G(\mathbf{v}) \quad \text{for all} \quad \mathbf{v} \in H^T \tag{2.17}$$

From a physical point of view, the dual solution $\mathbf{D^T}$ can be considered as the generalized electric field Green's function due to the injection of a set of vector sources. The dual error indicator formed up by $\mathbf{D^T}$ describes the global contribution to the local error in regions of interest.

As the first method to calculate the element-wise goal oriented error, we use a residual type a posteriori error estimator to compute the primary error as well as dual error [Zhong et al., 2012]. Given a conforming mesh $\mathcal{T}$, let $\mathcal{F}(\mathcal{T})$ denote the set of the interior faces of $\mathcal{T}$. For a face shared by two elements K_1 and K_2, we define the inter-element jumps of a scalar function p between elements K_1 and K_2 as

$$\langle p \rangle_f = p|_{K1} - p|_{K2}$$

For K $\in \mathcal{T}$, f $\in \mathcal{F}(\mathcal{T})$ and $\mathbf{u} \in H^T$, [Zhong et al., 2012] define the following element-wise volumetric residuals and face-wise jump residuals associated with interior faces as

$$R_1(\mathbf{u})|_K = (\mathbf{f} - \nabla \times \alpha \nabla \times \mathbf{u} + \beta \mathbf{u})|_K \tag{2.18}$$

$$R_2(\mathbf{u})|_K = \nabla \cdot (\mathbf{f} + \beta \mathbf{u})|_K \tag{2.19}$$

$$J_1(\mathbf{u})|_f = (\alpha(\nabla \times \mathbf{u}) \times \mathbf{n}_f)|_f \tag{2.20}$$

$$J_2(\mathbf{u})|_f = ((f + \beta\mathbf{u}) \cdot \mathbf{n}_f)|_f \tag{2.21}$$

The error indicator for $\mathbf{u} \in H^T$ on K $\in \mathcal{T}$ is given by

$$\eta_\tau^2(\mathbf{u}, K) = h_K^2(\|R_1(\mathbf{u})\|_K^2 + \|R_2(\mathbf{u})\|_K^2) + \sum_{f \in K \cap \mathcal{F}(\mathcal{T})} h_K(\langle J_1(\mathbf{u})\rangle_f^2 + \langle J_2(\mathbf{u})\rangle_f^2) \tag{2.22}$$

where $|K|$ is the volume of K and $h_K = |K|^{\frac{1}{3}}$ measures the size of the element K. The primary and dual error could be computed by replacing $\mathbf{u}$ with the discrete finite element solution $\mathbf{E^T}$ and $\mathbf{D^T}$, according to equation 2.18 - 2.21.

In the goal-oriented adaptive refinement algorithm, the estimated error for each element is weighted by its influence to the solution at the receivers as equation 2.23.

$$\eta_K = \eta_\tau(\mathbf{E^T}, K)\eta_\tau(\mathbf{D^T}, K) \tag{2.23}$$

As a result, refinement only occurs where the solution is inaccurate and where that inaccuracy corrupts the response at the locations of the EM receivers. To summarize the goal oriented adaptive refinement procedure, our adaptive refinement procedure starts with a coarse Delaunay discretization [Si, 2015] of the model domain. We apply the goal-oriented error estimation method as described to produce the local error indicator K for each element. The adaptive methods seek to increase the solution accuracy by iteratively refining the grid, where each iteration consists of selecting a subset of elements for refinement based on an estimate of their contribution to the solution error, and then refining the grid by creating new smaller elements in these regions. This process is repeated until the functional error is less than some user-specified tolerance.

As is shown, the residual based goal oriented error estimation approach is based on post-processing of the finite element solution for the primary and dual problems. The

primary error accounts for the volumetric and face jump residual generated from the finite element discretization. As the weight of by the primary error, the dual error describes the global influence effect to the local errors. Combing them together, we have the local error indicator which is used to refine the mesh.

2.3.3 Hierarchical Basis Error Estimation

Furthermore, we implemented the hierarchical basis error estimation method as another option to drive the refinement procedure. In both methods, we define the primary and dual problems on the linear curl-conforming space H^T (equation 2.24 - 2.25), consisting of the lowest order Nédélec basis functions. Primary error is weighted by the dual error to form up the local error indicator, such that the error indicator would carry the global influence to the solution at the receivers' location. Both methods provide reliable guides for which element to refine.

$$B(\mathbf{E}^T, \mathbf{v}) = F(\mathbf{v}) \quad \text{for all} \quad \mathbf{v} \in H^T \tag{2.24}$$

$$B(\mathbf{D}^T, \mathbf{v}) = G(\mathbf{v}) \quad \text{for all} \quad \mathbf{v} \in H^T \tag{2.25}$$

However, in the scheme of hierarchical basis error estimation, instead of calculating the face jump and volume residual (eq.(12-15)) from the primary and dual solution on the residual based scheme, we project and measure the finite element error **e** in an auxiliary space, which is defined as

$$\begin{aligned} Q^T = \{\mathbf{v} \in H : \mathbf{v}|_\tau \in [P_2(\tau)]^2 \quad &\text{for each} \quad \tau \in \mathcal{T}_n, \\ \mathbf{v}(z) = \mathbf{0} \quad &\text{for each} \quad z \in \mathcal{E}_n\} \end{aligned} \tag{2.26}$$

where $\mathcal{E}_n$ to be the set of interior edges of $\mathcal{T}_n$. Such space is said to consist of quadratic

'face-bump' functions, so-called because the standard basis for this space is naturally associated with the faces in the mesh. For each face of a tetrahedral, there are two independent face basis function associated and such functions vanish at every edge and the opposing vertex. For more detailed description of the face-basis function could refers to [Webb, 1999]. The estimated error in the higher order function space could be computed according to the following error equations:

$$B(\mathbf{e}, v) = F(v) - B(\mathbf{E}^T, v) \quad \text{for all} \quad v \in Q^T \tag{2.27}$$

$$B(\mathbf{d}, v) = G(v) - B(\mathbf{D}^T, v) \quad \text{for all} \quad v \in Q^T \tag{2.28}$$

Being the solution of equation 2.27 - 2.28 **e** and **d** are the numerical error for these primary and dual problem equation 2.24 and 2.25 in the auxiliary space. The solution of equations 2.28 and 2.27 are equivalent to the solution of a 2M$\times$2M linear system, where M is the number of interior faces in $\mathcal{T}$.

Compared with the edge basis system in our primary problem, the face basis system is more well-defined. Since each interior face only support two neighboring tetrahedral, each line of the the stiffness matrix will hold a fixed number of non-zero entries. We use the Gauss-seidel iterative solver [Press, 2007] to calculate the solution efficiently.

Based on the solution of equations 2.28 and 2.27, we then evaluate the energy norm in terms of the bilinear form B(,). According to equation 2.15, the final weighted goal-oriented error indicator could be expressed as:

$$\eta_\tau = \eta_\tau(\mathbf{e})\eta_\tau(\mathbf{d}) = ||\mathbf{e}||_{e,\tau}||\mathbf{d}||_{e,\tau} \tag{2.29}$$

η_τ are used to decide which triangles should be refined to further decrease the error.

In summary, both of the error estimation methods follows the same goal-oriented idea which is to weight the primary error by its influence to the solutions. Solutions from the adjoint/dual problem are used to form the dual error indicator, which carry the information about the global contribution to the local value of interest. The key difference is the dual error are evaluated in different function spaces. By evaluating the energy norm of **d** and **e**, we could get the local error indicator to drive the adaptive refinement.

2.3.4 Iteratively Adaptive Refinement Scheme

Our adaptive refinement procedure starts with a coarse Delaunay discretization of the model domain. Tetgen [Si, 2015] can rapidly generate a high quality mesh that conform to the polygon boundary in the model. There is no limitation on the amount of structural complexity included in the mesh. We apply the goal-oriented error estimation method as described to produce the local error indicator η_K for each element. Then we identify the fraction γ of elements with the largest errors, marking them for refinement. In practice, we find refining 5 - 10 percent worst elements works well.

Grid refinement is implemented with two refinement engines. First we implemented Tetgen, an open-source constrain and conforming delaunay discretization code, as an option for refinement engine. Elements selected for refinement are set to have their volume reduced by a factor of two, although the algorithm used by Tetgen refines based on a hierarchy of vertices instead of tetrahedra, so this is only approximate. The other option employs the Geometry Engine Methods from FETK [Holst, 2001] as a option. It bisects the longest edge of the flagged element, which directly divide the volume of the element into a half. This algorithm will results in a sequence meshes containing a hierarchy of tetrahedra rather than a hierarchy of vertices. This feature could make it easier to identify the parent element in the coarser mesh. Therefore, the forward projection of the estimated error could be carried out from a coarse mesh onto a refined

mesh.

Solution convergence is measured by computing the relative field difference between the current and previous iterations for all the receivers. This refinement process is repeated until the maximum value of the relative difference falls below some user-specified tolerance. E.g. relative difference of the x component of the electric field is desired to be less than 1 percent.

$$\delta\mathbf{E} = \frac{|\mathbf{E}_{i,j} - \mathbf{E}_{i-1,j}|}{\mathbf{E}_{i,j}} \tag{2.30}$$

where i and j are correspondingly the mesh and receiver indexes. With the goal-oriented error estimation method, the final mesh will be the optimal to generate accuracy solutions. The mesh refinement process are illustrated by the open-source software Paraview.

2.4 Parallel Domain Decomposition

In complex three dimensional geological situations, where many of these resources remain to be found, resistivity mapping requires large-scale modeling and imaging capabilities, as well as the ability to treat significant data volumes, which can easily overwhelm single-core and modest multicore computing hardware.

2.4.1 Data Domain Decomposition

Traditional methods for EM modeling utilize a single fixed mesh that is designed to be suitable for the entire range of parameters (i.e. transmitters, frequencies and receivers), therefore the mesh is likely to be over meshed for at least some of the data parameters, leading to an inefficiency in the run-time. Conversely, the domain decomposition scheme and the adaptive finite element technique allows MARE3DEM

Table 2.1: Parallel performance using the data decomposition scheme are compared with no decomposition example. The first row shows the performance without partitioning. The second and third rows show the performance of using 16 processors. For the cases with partitioning, the bounds in the statistics of the performance are taken from the fastest and slowest task.

Partitioning pattern	Number of edges	Total time(s)	Memory(GB)
No partitioning	2.11 million	2860	21
Box	0.437 - 0.561 million	446 - 707	3.36 - 3.81
Stripe	0.507 - 0.586 million	521 - 633	3.56 - 3.92

Table 2.2: Performance comparison between models with single and multiple transmitters. For both cases, the solving times are taken from the slowest task.

Number of Tx and Rx	Total time(s)	Memory(GB)
1 Tx, 256 Rx	633	3.92
4 Tx, 256 Rx	817	5.66

to generate a unique mesh that is optimized for a given set of parameters, resulting in a very efficient use of mesh. By decomposing the problem into small subsets according to the transmitters, receivers and frequencys in the data domain, we could alleviate the requirement of the computational resources for each subproblem, resulting in the increasing of capability to solve larger dataset in parallel.

The model here inherits the bathymetry data from the 3D model in the previous section. In this setting, we use a single transmitter and a 2D grid receivers array consisting of 256 receivers with 1km interval. We divide the receiver array into 16 subgroups with 16 processors carrying out the algorithm independently. Fig 2.1 shows the layout of the 2D array for two different partitioning patterns. Figures 2.2 and Fig 2.3 show the final refined mesh with partitioning. For each subgroup, fine mesh in the central region accommodates the seafloor topography. After five iterations, the error indicator decrease significantly and refinement concentrates on its own receiver group. For other subgroups, due to the field coupling between source and receivers, the regions contain transmitter and the sub-receivers group get large amount of refinement.

In both simulations, we run the refinement for 5 iterations and refinement the top

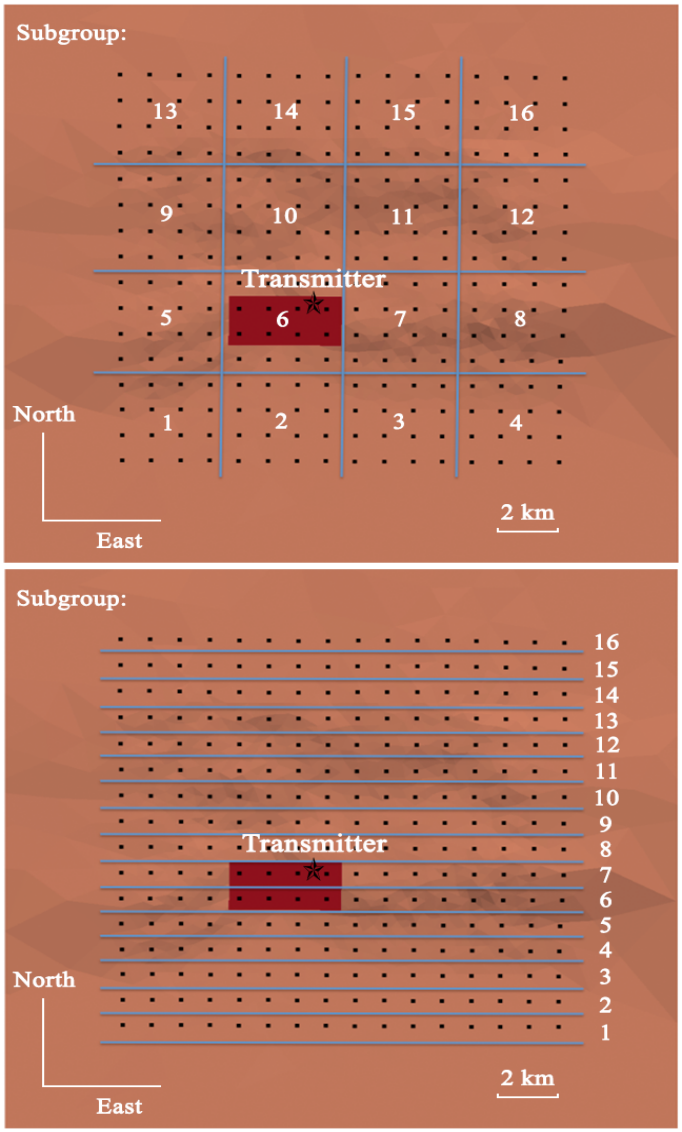

Figure 2.1: Data decomposition example on the 3D oil reservoir model. Data decomposition divides the receivers array into 16 groups and assign each subgroup to different processors. E.g. Process #1 has the first subgroup of 16 receivers in the blue box.

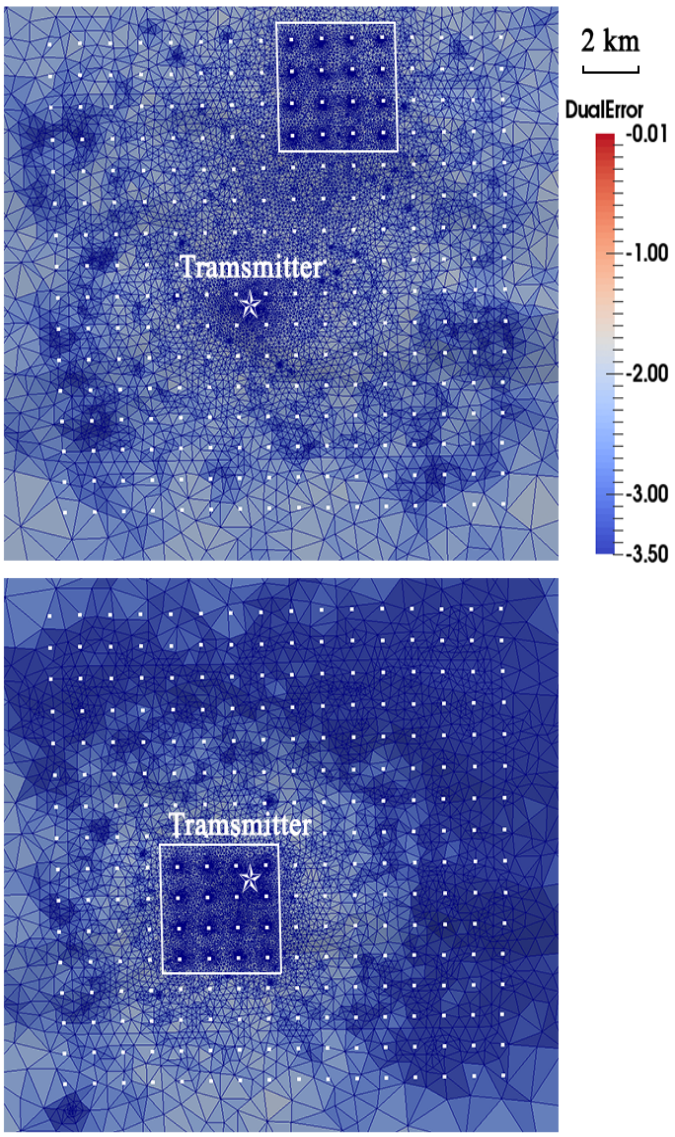

Figure 2.2: Overview of the subgroups for box partitioning pattern. Final refined mesh for the 15th (Top) and the 6th (bottom) subgroups. Shading stands for the value of the error estimator in log10 scale.

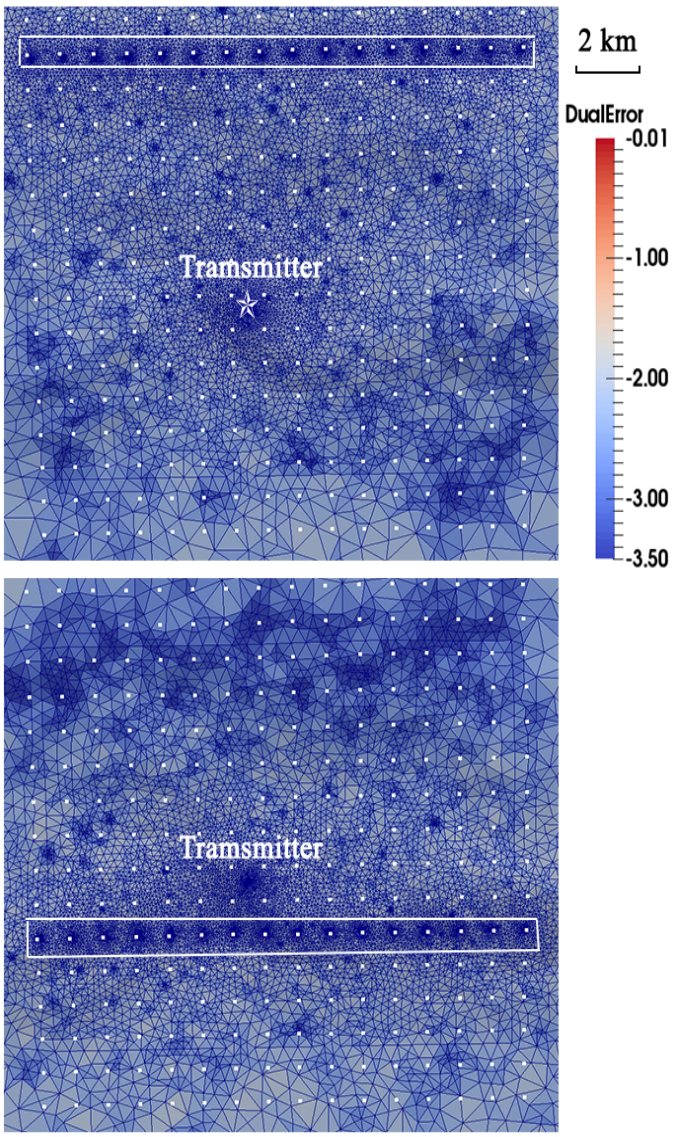

Figure 2.3: Overview of the subgroups for stripe partitioning pattern. Final refined mesh for the 15th (Top) and the 6th (bottom) subgroups. Shading stands for the value of the error estimator in log10 scale.

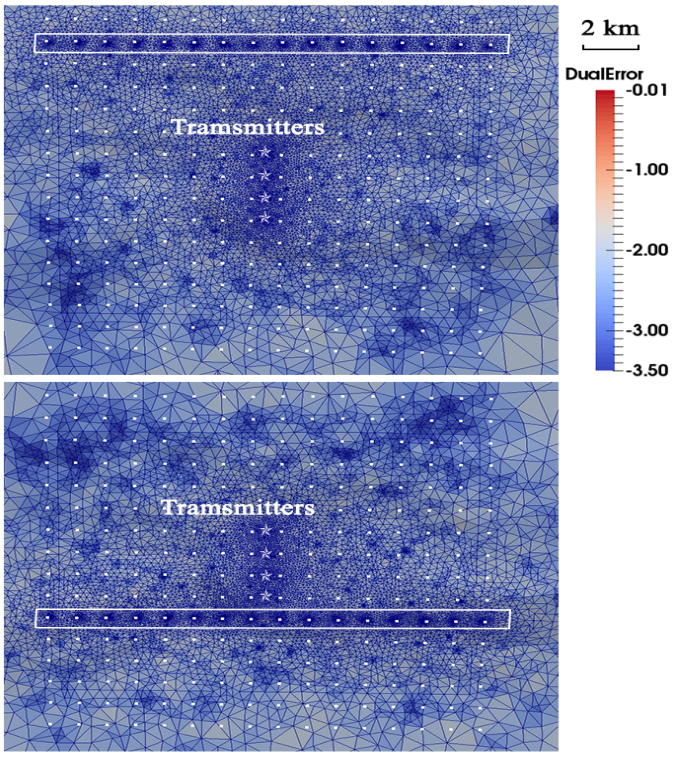

Figure 2.4: Final refinement results for subgroups 6th and 15th of model with 4 transmitters. Viewing from right above the seafloor, fine meshes in the central region of each group accommodate the seafloor topography. For each individual subgroup, transmitters and its own receivers are refined iteratively.

5% of elements with larger error estimator. Table 2.1 shows the performance comparison between using 1 and 16 processors. As we seen from the table, decomposition could reduce the number of edges around three fourths on average in the final mesh among all sub-problems. As a result, it saves more than four times of the computational time and five times of the memory on average. At the same time, we could also see the saving is not perfectly scaled with the number of processes used for computation. The scalability limitation is towfold. First, even the fine mesh associated with receivers are decreased as much as 16 times, but the system still need to model the large amount of elements in the outer region. Secondly, the bottleneck of computational is more about memory than computing power, when the problem get large, the limitation of memory will also be the bottleneck for further improvement. Comparing these two decomposition patterns, we could see that decomposing receivers array into stripes will have better efficiency and load balance over the other.

To illustrate the best performance possible, we adopt the stripe decomposition pattern to a model with four transmitters, in order to test the performance of direct solver for multiple transmitters. Since the mesh structure differs among different groups, each processor will solve different equation systems. However, for each sub-problem, different transmitters will share the same mesh structure, therefore the stiffness matrix in equation 2.10 are the same. In this sense, the direct solver could factorize the left hand side stiffness matrix once and apply the factorization result to all the transmitters on the right hand side, therefore achieving a higher efficiency.

From Table 2.2, we can see the increase of memory requirement is moderate. The solving time only increase less than 30% when the number of modeling task increases 4 times. Once the factorization which consumes most of the computing time is completed, it is relative trivial to solve the addition sources. In the data decomposition scheme, each task is independent and running in parallel, therefore allowing for a large savings in the

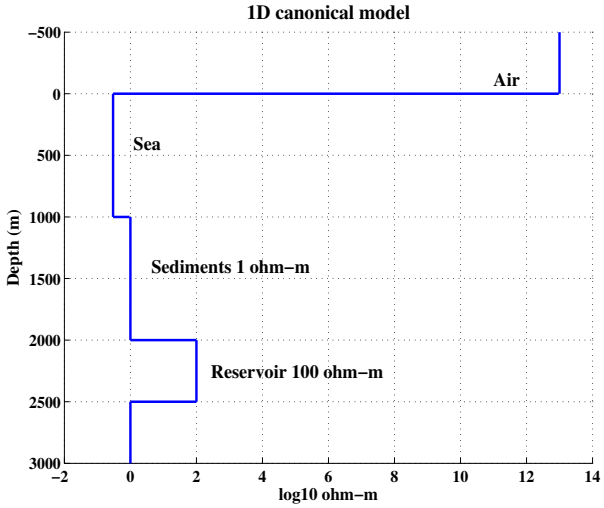

Figure 2.5: The 5-layered 1D model. The cross-section of the model is shown. The top and bottom of the profile are extend to the model boundaries.

computational resources.

Fig 2.4 shows the refinement results for the 6th and 15th subgroups when we decompose the array into stripes. As we can see, the increased density of elements is only associated with the adding transmitters.

2.5 Numerical Examples

From the following two examples, we will validate the reliability and effectiveness of MARE3DEM, as well as study the performance of the adaptive refinement algorithm for CSEM modeling.

2.5.1 Canonical Model

The first example considers marine CSEM responses for the 1-D layered reservoir model, consisting of the resistive air layer, 1000-m-thick sea water and a 500-m-thick, 100-ohm-m oil reservoir buried 2 km below the seafloor in 1 ohm-m sediments. In

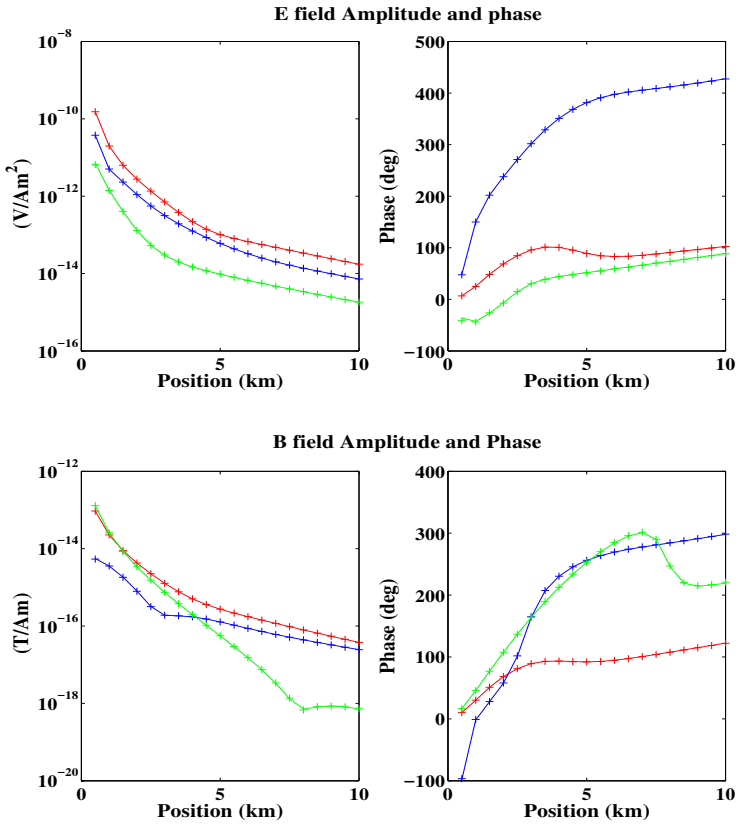

Figure 2.6: Validation of the electric and magnetic field responses computed by MARE3DEM(dots) for the 1-D layered reservoir model. It also shows a comparison with results computed with the Dipole1D code (lines) for both amplitude and phrase.

this tests, a 0.1 Hz horizontal electric dipole transmitter is located 50 m above the seafloor, pointing to the x direction. Receivers are positioned along transect x=y with a 500m intervals from 500m to 10 km range. Therefore, there is a 45 azimuth angle between the orientation of transmitter and the line of receivers. In this setting, all 6 field components will be non-zero, thus testing all aspects of MARE3DEM's output fields. The initial coarse mesh is a 100km cubic, consisting of 386,851 elements, while the final meshes contains around 1.3 million elements. Computations were performed on a iMac containing a 3.5GHz quad-core Intel Core i7 processor. The accuracy of the MARE2DEM solutions is measured by comparing 3D solution with the semi-analytical

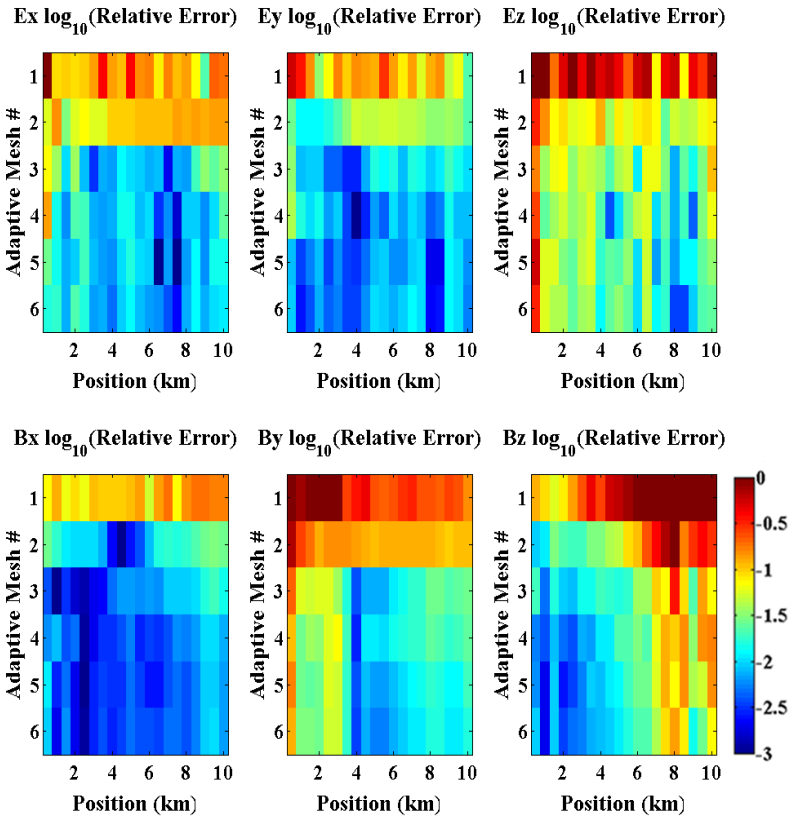

Figure 2.7: Relative error in the solution decreases with each successive mesh refinement iteration. Here red is for large error and dark blue means less than 0.1% tolerance.

1D responses generated by the open-source code Dipole1D [Key, 2009]. Dipole1D is a useful tool to benchmark the accuracy of the 3D code, since it uses an explicit formulation for each field component at each source-receiver offset, thus attains a similar order of accuracy for each component(Li and Kerry). Figure 2.6 shows the amplitude and phase responses for the electric(top) and magnetic(bottom) field, as computed using the final 6th mesh (dots). According to the analytical solution, we could compute the relative error for every receiver in each iteration.

As is shown in Figure 2.7, the relative error of the finite element fields decrease efficiently with the iterations. This shows the efficiency in mesh refinement made possible by the goal-oriented error estimation. Errors of horizontal components of the electric field

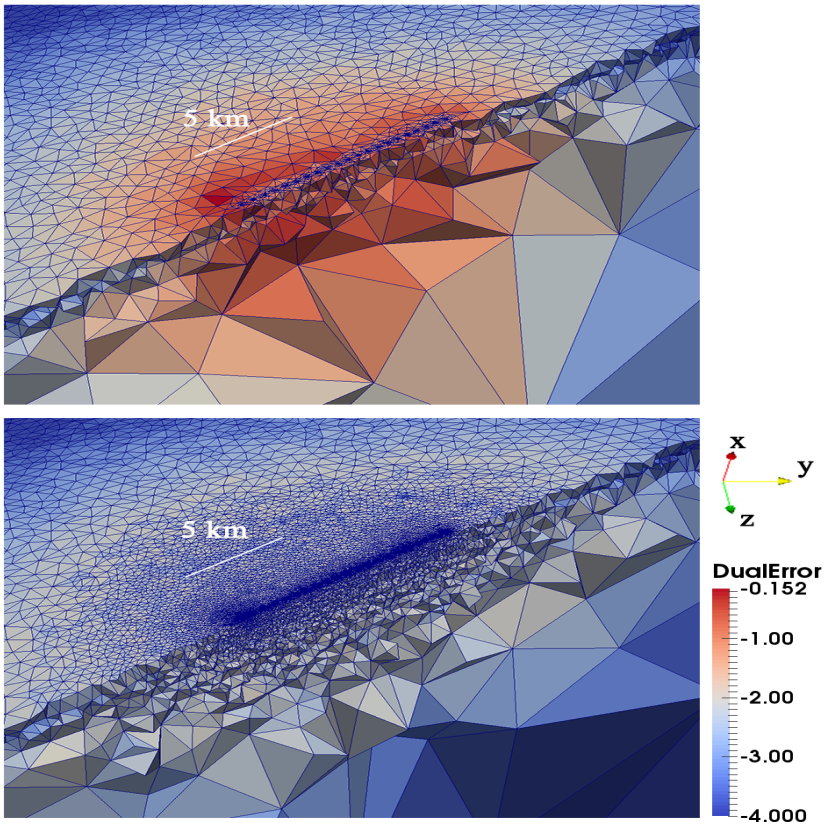

Figure 2.8: The slice cut over the seafloor. Model above the seafloor has been removed to see the refinement result around receivers. Top: Starting mesh consisted of 386,851 tetrahedral with about 452,293 edges. Bottom: final mesh at the 6th iteration. Shading indicates the amplitude of the dual weighted error estimators.The algorithm directs refinement toward elements most affecting the dense array of receivers.

and the B_x component are well below 1%. For some locations, such solution are accuracy to 0.1%. The less accuracy in the magnetic field than the electric field is expected and observed in B_y, since the magnetic component are computed from the less accurate spatial gradients of the electric fields. Since the source has no vertical component, the field of the vertical direction have a smaller amplitude compared with the horizontal ones, resulting less accuracy in the E_z and B_z fields. In general, all components are within an order of magnitude accuracy.

Figure 2.8 shows the coarse initial mesh consisting of 452,293 of edges and the refined result of the final mesh. Shading indicates the amplitude of the dual weighted

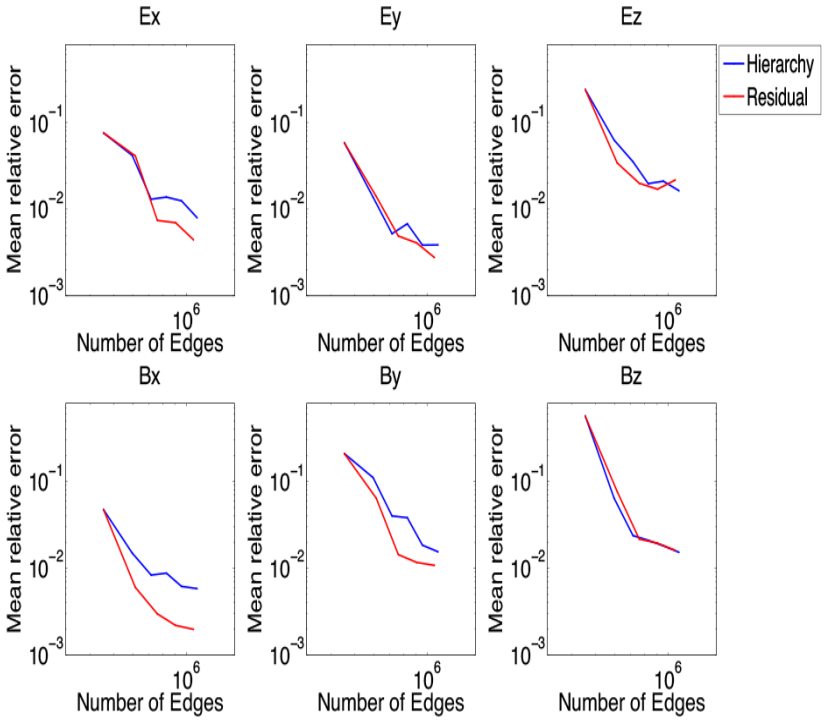

Figure 2.9: The comparison between two error estimation approaches based on the 1D layered model. Residual based method are showed in red and Hierarchical method are in blue.

error estimators. In the initial mesh, a priori mesh refinement has been carried out before the modeling iterations, guaranteeing the volume of the tetrahedral at the receivers location is less than $1m^3$. As the final mesh shown, the refinement not only happened in regions which contain receivers, but also extend to the outer regions to mitigate the pollution effects. In other words, the algorithm directs refinement toward elements most affecting the dense array of receivers. In each iteration, the algorithm selects elements where the solution is inaccurate and where that inaccuracy corrupts the solution at the receivers' locations. Plus, our goal-oriented approach is effective to detect the pollution effect and can be used to compute asymptotically exact FE solutions [Li and Key, 2007].

Figure 2.9 shows the comparison using two different error estimation approach. Averaged relative error among receivers are plotted as the function of the number of

Table 2.3: Runtime and memory usage for each iteration. Total time is the cumulative time starting from the first iteration. In each iteration, the solving time for Eq. 2.10 takes up to 88%.

Iteration	Edge #	Iteration time(s)	Total time(s)	Memory(GB)
1	452,293	25.7	25.7	3.04
2	612,906	38.1	73.8	4.42
3	755,396	57.9	145	6.81
4	898,563	84.9	245	9.31
5	1,061,113	128	391	12.9
6	1,252,179	183	595	17.0

Table 2.4: Runtime and memory usage for each iteration for the 3D reservoir model.

Iteration	Edge number	Total time(s)	Memory(GB)
1	241,821	13.1	1.05
2	415,341	44.0	3.36
3	618,785	98.1	6.15
4	901,588	186	9.94
5	1,302,065	360	16.5
6	1,872,164	625	26.9

edges in the mesh. As is shown, both methods can effectively reduce the error. Figure 2.10 shows the dual error distribution on the seafloor for each iteration. The dual error is computed as the element-wise weighted L2 norm, according to eq. 2.23. In the initial mesh, larger value of error indicator are associated with the regions containing receivers. Along the refinement, the large value of dual error indicator are wiped out continuously, demonstrating the effectiveness of the algorithm to reduce the dual error.

2.5.2 Model with Bathymetry

3D oil reservoir model

The previous example demonstrates the accuracy of MARE3DEM and verifies the reliability the goal-oriented error estimation approach. Here we demonstrate how the algorithm performs for a significantly more complicated model by designing a synthetic

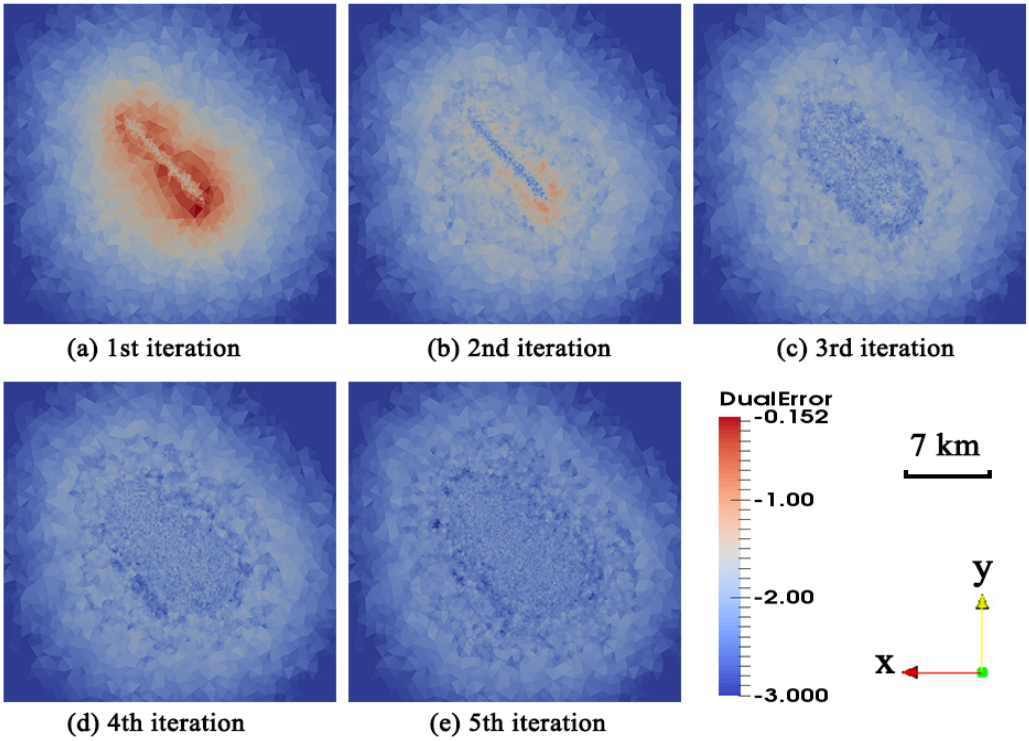

Figure 2.10: Dual error distribution on the seafloor in each iteration. First to the last meshes corresponds to (a)-(e). Overview of the seafloor, warm color represents larger value of the dual error. In the initial mesh, the distribution of large error indicator is aligned with the line of receivers.

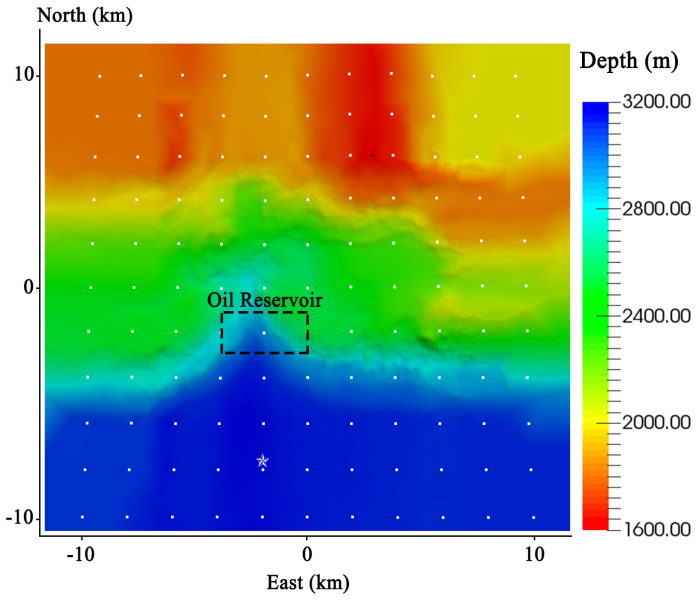

Figure 2.11: Overview of the topography of the region. From the north of Gulf of Mexico, the water depth of the region ranges from 1600m(red) to 3200m(blue). The white dots are receivers deployed on the seafloor and the star stands for the transmitter's location.

model containing the sea floor topography, an underlying resistive oil reservoir and a deeper basement with variable topography. The specific topography data is from the north region of Gulf of Mexico. Figure 2.11 shows the regional bathymetry variations where the water depth is between 1600 and 3200 meters. The region near sea canyon have intensive topography variation which cannot be efficiently discretized on a structure rectangle grid. To accommodate the topography more efficiently, we use a relatively dense surface triangulation of the bathymetry dataset with element diameter around 400m. As a result, it only take 1596 mesh vertices to accommodate the topography. The whole modeling domain is a cubic with 100km in each dimension where topography are incorporated as the sea-seafloor interface and the sediment-basement interface. To simulate a marine CSEM survey, we consider the case of a transmitter of 0.25Hz, located 100m above the seafloor. A 10km by 10km 2D grid of receivers are positioned on the

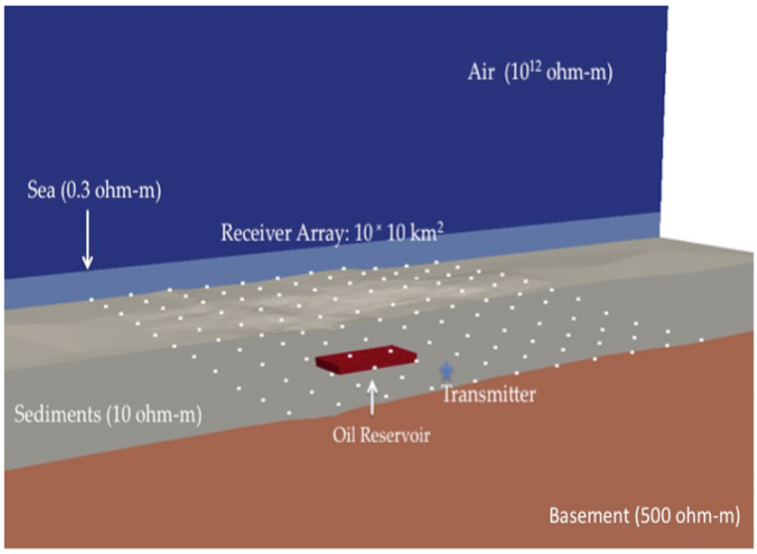

Figure 2.12: View of the topography after removing the seawater and air layers. A 0.25Hz transmitter is located 100m above the seafloor, pointing to the x axis. 3km right beneath the transmitter is the oil reservoir, with the dimension [2000 4000 500] m.

seafloor, with a interval of 2km alone the north and east direction. Computations were performed serially on the TSCC processors.

In each iteration, top 10% elements with the largest error indicator will be selected and refined. It takes 6 iterations to reach the final mesh with 253,961 vertices and 1,872,164 unknowns. Table 2.4 show the hierarchies of the meshes for the 3D oil reservoir model, along with the adaptive performance in items of total runtime and memory requirement.

The previous 1D example shows the performance of the code when compared to a known 1D solution. However, we do not have the analytic solution for modeling arbitrarily complicated 3D model. Still, a way of estimating the solution accuracy at each refinement iteration without a priori knowledge of the solution is at need. Therefore, we use the first order difference of the fields at two consequence iteration as a measure of the convergence of the solution. Due to the geometry of the transmitter and receiver, the null component Ey, Ez and Bx are significantly smaller than the non-vanishing components.

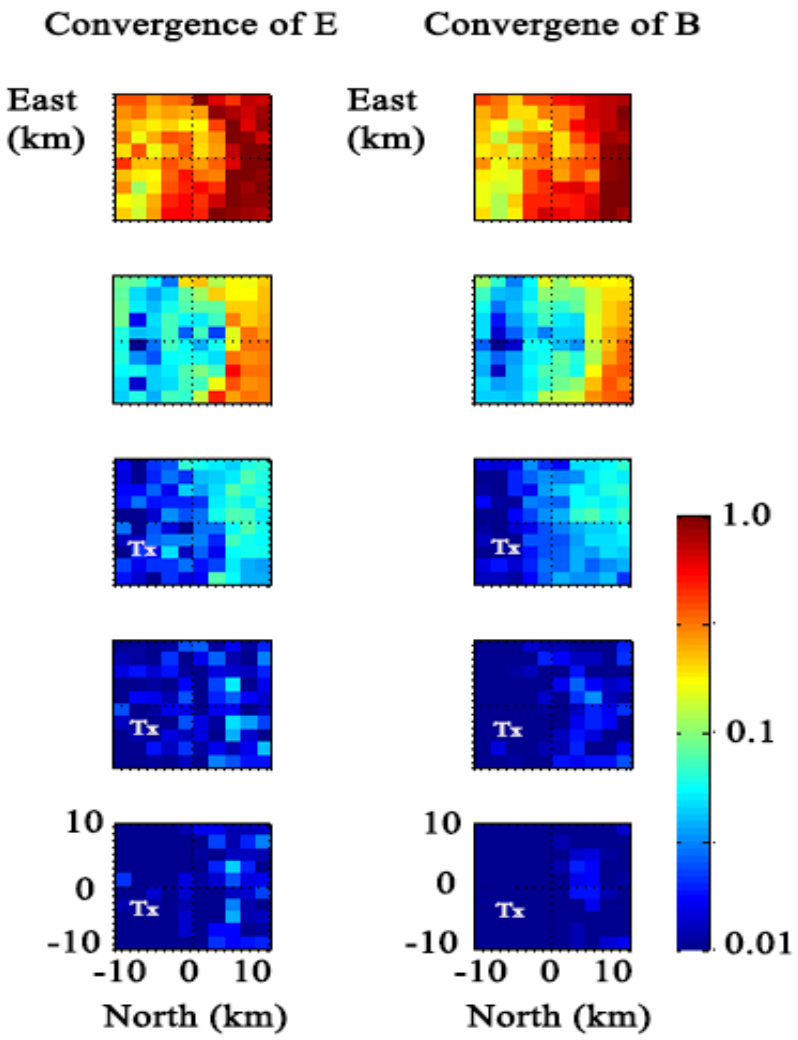

Figure 2.13: Convergence of the electric and magnetic field amplitude. Each box in the 2D array correspond to receivers. Warm color stands for larger difference, deep blue means the first order difference is 1%. The lighting box which does not converge in the later iterations reflects the source singularity.

Instead of showing the convergence of each single component, we plot the convergence of the amplitude of both the electric and magnetic filed. Figure 2.13 shows the convergence of the amplitude of the field with iterations.

Figure 2.14 shows the interior of the first and last mesh. During the refinement process, most of the refinement focuses on the regions contains the receivers and transmitters. The continuity of fine elements along the seafloor is expected, since the fields have considerable curvature at the seafloor interface and the error indicator could guide the refinement to elements most affecting the receivers. Interface of the sediment and basement also shows an increased concentration of elements.

To quantify the stability of the algorithm and to estimate the distortion of the electromagnetic field due to some subsurface anomaly, we introduce another model without the resistive oil reservoir for comparison. Both of the models shared the same data parameters, except for the existence of the reservoir. Fig 2.15 plots the relative difference of the response for each receiver.

The comparison shows that MARE3DEM could capture the anomaly generated by the buried oil reservoir in depth. The dimension of the anomaly varies with the size of the reservoir body which indicates the possible application to reservoir monitoring.

2.5.3 Conclusion

The parallel adaptive finite element modeling method presented here provide a new tool for studying the controlled source electromagnetic response of complex 3D structure. The adaptive algorithm started from a coarse unstructured mesh which could readily accommodate complex geological structure such as seafloor topography and seismically imaged strata. The goal oriented error estimation approach could automatically generate a optimal mesh where users are free from having to design a complex grid for each specific problem. The a priori refinement at the receiver's locations proved to be

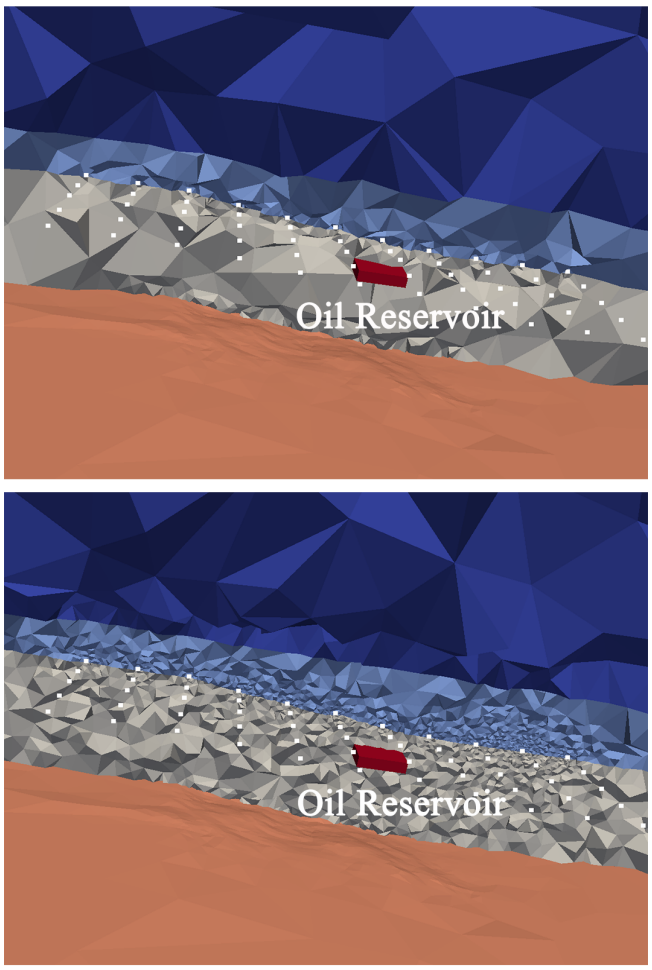

Figure 2.14: Profile alone the survey line. Initial coarse mesh and the final mesh at 7th iteration. Refinement is concentrated in the region containing the receivers and the oil reservoir.

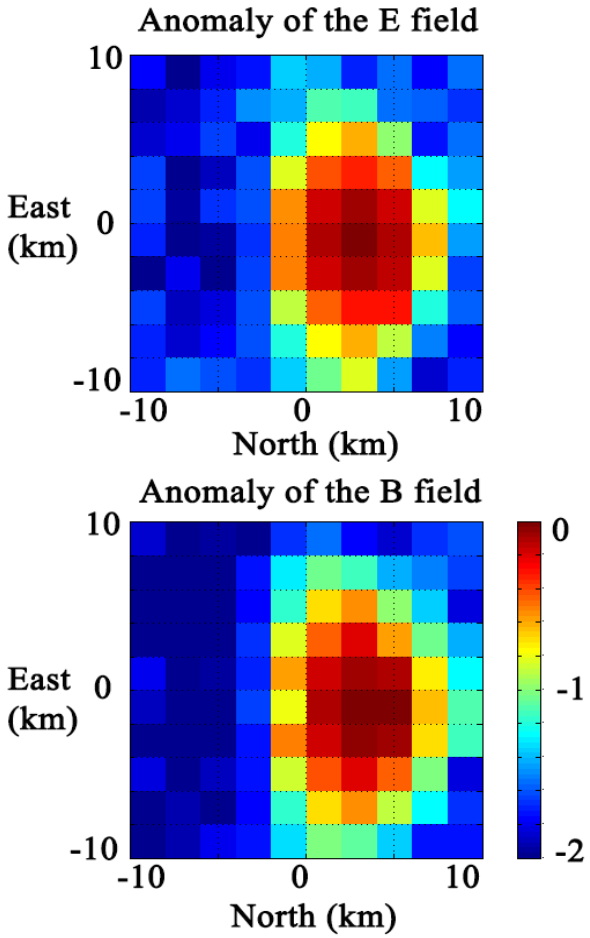

Figure 2.15: Anomaly generated by the oil reservoir. The horizontal extension of the oil reservoir is 2km by 4km with 1km thickness.

beneficial to enhance the convergence of the solution. Highly accurate EM responses are calculated based on the final optimalized mesh with the minimum number of unknowns. Enable the LU factorization, not only makes the dual problem associated with the error estimator be solved directly, but also allows multiple transmitters to be modeled more efficiently.

The data domain decomposition divides the entire data set into different subset of transmitters, receivers and frequencies. Since each task is naturally independent, this scheme improves the efficiency for larger data sets, such as 2D receivers girds. Mesh sharing for nearby frequencies could be also used to reduce the number of tasks when the computing power is a limitation. For large computing cluster, parallel matrix factorizations on top of the data decomposition scheme could result in further speed improvement.

The accurate and effective forward solver not only enhances the modeling capacity for complex 3D problems, but also proves to be more useful as a kernel routine for 3D non-linear inversions. As the next step, we will apply this adaptive finite element method to 3D Gaussian Newton inversion. For the inversion framework, we will use a dual grid strategy, where the forward and inverse meshes are nested with each other. Such mesh hierarchy will convenience the map of attributes between forward and inverse meshes. Moreover, the accuracy of the forward solution and jacobian matrix will be continuously improved, to stabilize the inversion process without loss of accuracy.

The text of Chapter 2, in part, is currently being prepared for submission for publication of the material as it may appear in Zhang, Y., Key, K., Ovall, J., Holst, M., Parallel goal-oriented adaptive finite element modeling for 3D electromagnetic exploration, Geophysics, 2017. The dissertation author was the primary investigator and author of this paper.

Chapter 3

Inversion

The inverse problem is to find a conductivity model compatible with a given data set. Solutions to this problem are well described throughout the literature of EM geophysics [Parker, 1994, Zhdanov, 2015]. Since a given data set is finite and imprecise, an infinite number of solutions to the inverse problem exist. A standard method for handling this non-uniqueness is to restrict the set of acceptable solutions to those that meet some a priori constraints on model structure. This process is known as the regularized inverse problem.

We introduce a new scheme for the reliable 3D inversion of marine controlled-source electromagnetic (EM) data. Our code, named Modeling with Adaptively Refined Elements for 3D EM (MARE3DEM), uses a new variant of the regularized Occam method for the inversion framework. A parallel goal-oriented adaptive finite element method serves as the backbone for the forward operator. Both the forward and inverse model domains are simulated using unstructured tetrahedral meshes, which readily accommodate arbitrarily complex 3D conductivity variations. The unstructured inverse mesh efficiently handles multiple scale structures and allows for fine-scale model parameters within the region of interest, while parameters in the outer domain can be made

coarser. The inverse and forward domains are decoupled with the initial forward mesh, which is nested in the inverse mesh. This initial mesh is iteratively refined using a goal-oriented adaptive scheme until the forward solution's accuracy converges to the desired tolerance. As the key interface between the forward and inverse operator, the sensitivity kernels that establish a linear relationship between changes in the model conductivity and changes in the modeled responses are efficiently computed using the adjoint-reciprocity method on the optimally refined mesh. Parallel computation of the forward responses and sensitivity kernels follows a data decomposition scheme where independent modeling tasks containing different frequencies and subsets of the transmitters and receivers are simulated in parallel. This gives the algorithm a high degree of scalability for significantly faster solve times when run using hundreds or thousands of processors on a high performance computing cluster. Further parallel scalability is obtained in the regularized Gauss-Newton portion of the inversion using parallel dense matrix-matrix multiplication and matrix factorization routines implemented with the ScaLAPACK library. We show the scalability, reliability and the potential of the algorithm to deal with complex geological scenarios by applying it to the inversion of synthetic marine controlled-source EM data generated for a complex 3D offshore model with significant seafloor topography.

3.1 A review of Non-linear Inversion for EM geophysics

Inverse problem is essentially an optimization problem, which can be generalized as searching for a set of model parameters which could fit the observed data. For the geophysical inverse problem, from the observed data measured along the surface of the model, we seek to recover the model parameters for the entire domain.

As one of the popular optimization approach, bayesian stochastic framework and Markov Chain Monte Carlo sampling methods may offer a way for estimating

the resistivity of the subsurface along with the associated uncertainties. The paper of [Chen and Dickens, 2009] provide a good overview of the methods for reservoir estimation problems. The recent paper by [Ray et al., 2014] uses a reversible-jump Markov chain Monte Carlo method to sample the Bayesian posterior model probability density function of 2D seafloor resistivity as constrained by marine controlled source electromagnetic data. Stochastic inversion could provide a posterior distribution of the model parameters, making it a good tool to estimate the model uncertainties. Moreover, since each sample of the likelihood function requires the solution of a independent EM boundary value problem, the solution of such a problem can be efficiently obtained by distributing it over a number of parallel computing tasks. Nevertheless, the advantages of stochastic estimation come at considerable computational expense. As a result, stochastic sampling methods are only suitable for simplified layered and 2D geologies. Global stochastic estimation for three-dimension problems are still too time and memory intensive to be of practical use.

The deterministic approach seeks a single model to produce the minimum misfit, with regard to the EM measurements. To reconstruct a constrained model of geology given a set of observed data, a number of distinct optimization algorithms have been developed. For example, [Newman and Commer, 2005] developed a conjugate-gradient framework to invert transient electromagnetic (TEM) data sets. [Key, 2016] developed a Gauss-newton based 2D anisotropic inversion of magnetotelluric (MT) data and frequency-domain controlled-source electromagnetic (CSEM) data. All of these deterministic methods define and minimize a cost functional using the derivative-based approaches, such as the non-linear conjugate gradient method [Newman and Alumbaugh, 2000], the quasi-Newton approach [Avdeev and Avdeeva, 2009] and the Gauss-Newton method [Constable et al., 2012].

In this study, we use the Occam's inversion method, a variant of non-linear Gauss-

Newton method, to find the smoothest model that fits the data. The basic motivation for seeking smooth models is that we wish to not be misled by features that appear in the model but that are not essential to match the observations. Ideally, the features of the inverted model depart from the simplest case only as far as is necessary to fit the data [Constable et al., 2012].

A important step in the creation of an inversion engine is to develop a forward operator for calculating the model response. Since the iterative inversion scheme will involve a large number of forward problems, the ability to solve the forward problem as efficiently as possible is crucial to the inversion strategies. Hence, we establish the inversion based on a 3D adaptive finite element forward solver [Zhang et al., 2015], which efficiently calculates the model responses in the frequency domain. To accurately accommodate the arbitrarily complex 3D conductivity variations and a priori known boundaries, we use the unstructured tetrahedral mesh. Accuracy of the finite element solution can be continuously improved through the iterative goal-oriented adaptive mesh refinements. To avoid over-parameterization of the inverse problem, we use the dual grid strategy [Commer and Newman, 2008] to decouple the forward and inverse meshes.

Our main focus of this study is to present numerical algorithms for 3D CSEM inversion. Synthetic inversion tests are used to examine the capability and robustness of the algorithm to recover the a priori known structures.

3.2 Occam's Razor: Simplest solution is preferred

In the early fourteen century William of Ockham wrote that 'It is vain to do with more what can be done with fewer'. What has been known as Occam's razor has also become a fundamental tenet of modern science; hypotheses should be neither unnecessarily complicated nor unnecessarily numerous [Constable et al., 2012]. To avoid

being misled by features that appear in the model but are not essential in matching the observations, our approach find the smoothest model in a special sense such that its features depart from the simplest case only as far as is necessary to fit the data. Finally, our approach gurarntees that the real profile must be at least as rich in structure as the profile found but never less complex in structure.

To set the context for the new implementation constructs for 3D problems, we briefly review the well-known Occam's method [Constable et al., 2012]. Occam's inversion method seeks to minimize the following unconstrained functional:

$$U = ||\mathbf{Rm}||^2 + ||\mathbf{P}(\mathbf{m} - \mathbf{m}^*)||^2 + \mu^{-1}||\{\mathbf{W}(\mathbf{d} - \mathcal{F}(\mathbf{m}))||^2 \tag{3.1}$$

where $\mathbf{m}$ is the n dimensional model vector of $log_{10}(\sigma)$ for each model parameters. The first term measures the model's roughness, which is defined as the weighted first order difference between the neighboring elements and the centering model parameters. The second term measures the model's deviation from a preferred model $\mathbf{m}^*$. The diagonal matrix $\mathbf{P}$ contains scaling parameters that determine the relative weighting between the model preference and model roughness. If a user desires to bias a particular subset of the model parameters, the corresponding diagonal elements can be set to some positive weighting value and the desired resistivity can be inserted into $\mathbf{m}^*$. The third term is the difference between the model response and the observed data weighted by the inverse standard errors $\mathbf{W}$. μ is the Lagrange multiplier which controls the trade off between the data misfit and the penalty terms, at the same time stabilizing the ill-conditioned inverse problem. By penalizing the roughness term, Occam's inversion searches for the smoothest model which fits the data within the specific target misfit.

To solve for the set of parameters which minimizes the constrained functional, we take the derivative of U with respect to the model parameter $\mathbf{m}$ and set it to zero. As is

mentioned in the previous chapter, the derivative of the forward operator is nonlinear in electromagnetics, such that the resulting equation has to be solved iteratively by creating a sequence of models, each of which gradually provides a better fit to the data. After linearizing the forward response about a starting model $\mathbf{m}_k$, the model update equation is:

$$\mathbf{m}_{k+1} = [\mu(\mathbf{R}^T\mathbf{R} + \mathbf{P}^T\mathbf{P}) + \mathbf{W}\mathbf{J}^T\mathbf{W}\mathbf{J}]^{-1}[(\mathbf{W}\mathbf{J})^T\mathbf{W}\hat{\mathbf{d}} + \mu\mathbf{P}^T\mathbf{P}\mathbf{m}_*] \tag{3.2}$$

with the modified data vector,

$$\hat{\mathbf{d}} = \mathbf{d} - \mathcal{F}(\mathbf{m}_k) + \mathbf{J}_k\mathbf{m}_k \tag{3.3}$$

$\mathbf{J}_k$ is the linearized model response gradient, or Jacobian matrix, defined as:

$$J_{ij} = \frac{\mathcal{F}(\mathbf{m}_k)}{m_j} = \frac{\mathcal{F}(\mathbf{m}_k)}{log_{10}\rho_j} = -\frac{ln(10)}{\rho_j}\frac{\mathcal{F}(\mathbf{m}_k)}{\sigma_j} \tag{3.4}$$

where i and j are indexes for the data and model parameters. For example, the i_{th} row and j_{th} column in the Jacobian matrix describe the change of the i_{th} data with respect to the variation of the j_{th} model parameter. In other words, J is a sensitivity matrix containing the derivative of each field component with respect to each model parameters. The method for efficiently computing J for 3D CSEM will be discussed in a later session.

To solve the model update equation, one must choose the value of the Lagrange multiplier. The approach used by Occam's method is to perform a golden section search of the lagrange multiplier to find the model $\mathbf{m}_{k+1}$ with the best fit to the data. The model update iterations are continued in this manner until the target misfit λ^2_{rms} has been reached, at which point Brent's method [Press et al., 1996] is used to find the intercepts. There can be more than one intercept of λ^2_{rms} along μ, and the model with the largest μ is chosen, because it will tend to be the smoothest model. In practice, the target misfit usually is

chosen to be equal to unity,

$$\lambda_{rms} = \sqrt{\frac{1}{n}\sum_{i=1}^{n}[\frac{d_i - \mathcal{F}(\mathbf{m_{k+1}})}{\sigma_i}]^2} \tag{3.5}$$

where n is the number of data and σ_i is the standard error of the i_{th} datum.

For both the regular Occam and fast Occam approaches, if the minimum search fails to find a model with a lower misfit, a reduced model step is taken and the line search is carried out again using the model $\mathbf{m}'_{k+1}$:

$$\mathbf{m}'_{\mathbf{k+1}} = \alpha\mathbf{m_{k+1}} + (1-\alpha)\mathbf{m_k} \tag{3.6}$$

Initially, the step size α is set to be equal to 1 and successively cut in half each time the line search fails to find a better fitting model.

3.2.1 Model Parameterization Using Dual Grid Strategy

We employ the dual grid strategy for the efficient discretization of the inverse model. The advantage of the dual grid method is the ability to reduce the number of unknowns of the inverse problem without compromising the accuracy of the forward solution. Since the inverse grid is fixed, the tiny finite elements required around the transmitters and receivers for numerical accuracy of the forward responses will not increase the size of the inverse problem. In the dual grid strategy, the inverse mesh has a large dimensional extension to satisfy the homogenous dirichlet boundary conditions for the finite element method. Adaptive mesh refinement could be performed during each step of the inversion to ensure the forward responses retain accuracy, while the model conductivity parameters change. The forward mesh based on the inverse mesh will be automatically generated using our goal-oriented adaptive refinement method, which

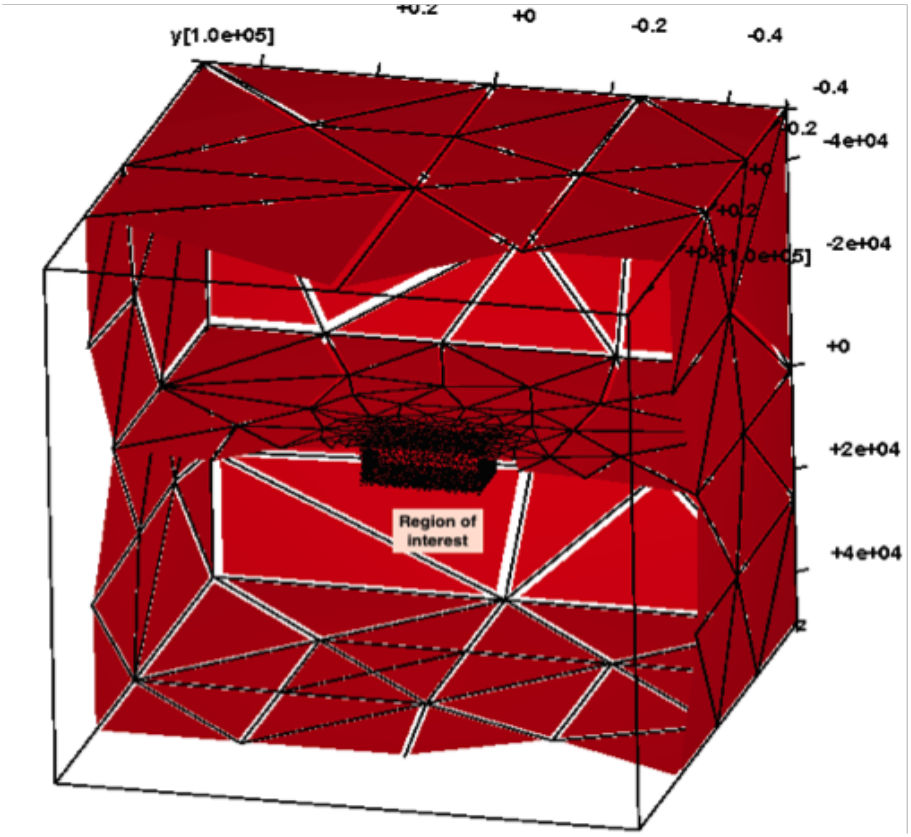

Figure 3.1: Polygon of the inverse model. In this example, we have a two layered inverse model. The top layer is the fixed region and the lower layer contains the free parameters. A subregion of interest was created inside of the free region with its bottom depth at 8km.

always conforms to the parameter grid. The nested relationship between the forward and inverse mesh also facilitates the mapping of conductivity and sensitivity kernel between the forward and inverse meshes. In addition, there is a subregion of interest in the middle of the modeling domain, which was filled with smaller tetrahedrons to maximize the data resolution. The outside region has increasingly larger parameters to reflect the decrease of resolution as the distance from the central region increases.

The dual grid was shown to be beneficial in 2D ([Hedlin and Constable, 2012]) and 3D MT ([Grayver, 2015]) inversions. In our approach, the user only needs to define the inverse parameter grid so that the code would then automatically generate and refine the finite element meshes on the fly.

3.2.2 Calculation of First and Second Order Derivatives

The sensitivity kernel describes the change of the fields at each receiver with respect to the variation of the conductivity of the inverse parameter. While in principle these can be obtained directly by taking the partial derivative of equation 3.1 with respect to each parameter and then solving the corresponding finite-element system, this approach becomes inefficient when the number of model parameters exceeds the total number of receiver components. To calculate the kernel more efficiently, we use the adjoint reciprocity formula provided in [McGillivray et al., 1994] to calculate the EM sensitivities. If there are p total measured electric and magnetic field components, the adjoint reciprocity method requires only p additional solutions to the original finite-element system. The solving of these additional system can reuse the factorization result for the p new right-hand side, resulting in a large savings compared to the direct sensitivity solution when the number of model parameter is much greater than p. Therefore, this adds another advantage for using direct solver compared with iterative solvers. The detailed derivation of the adjoint reciprocity formula can be founded in [McGillivray et al., 1994].

The sensitivity to parameter σ_j is found with the follow formula:

$$\int_{\Omega}(\mathbf{M}^{\alpha}\cdot\frac{\partial\mathbf{H}}{\partial\sigma_j}+\mathbf{J}^{\alpha}\cdot\frac{\partial\mathbf{E}}{\partial\sigma_j})d\Omega=\int_{V_j}\mathbf{E}^{\alpha}\cdot\mathbf{E}\frac{\partial\bar{\sigma}}{\partial\sigma_j}dV_j \tag{3.7}$$

where $\mathbf{M}^{\alpha}$ and $\mathbf{J}^{\alpha}$ are the adjoint source defined at each receiver's position. For isotropic models, the derivative $\frac{\partial\bar{\sigma}}{\partial\sigma_j}=1$ and the sensitivity depends on all three components of the electric field within parameter j. For example, to calculate the electric sensitivity for isotropic models, we place a vector electric current delta function at the corresponding receiver's location. By varying the orientation of the adjoint electric source among the coordinate axes, we compute the full components of the electric sensitivity according to the following equation:

$$\frac{\partial E_{k,i}}{\partial\sigma_j}=\int_{V_j}\mathbf{E}^{\alpha}\cdot\mathbf{E}dV_j \tag{3.8}$$

where k stands for the permutation of axis. The sensitivity for the i-th transmitter-receiver pair with respect to the j-th parameter is simply the integral of the dot product between the primary and adjoint electric field over the volume of that inverse parameter. By calculating this integral over all the elements for all the data type, we could get the explicit form of the jacobian matrix, which is a large dense matrix. To deal with the dense matrix operation, currently, we employ the ScaLAPACK routine PDSYRK to compute the dense matrix multiplication and routines PDPOTRF and PDPFTRS to solve the model update equation using Cholesky factorization. To deal with larger model, we could calculate the dense matrix operations distributedly in parallel, as discussed in [Key, 2016]. The details of the distributed dense matrix operations will be shown in the next Chapter.

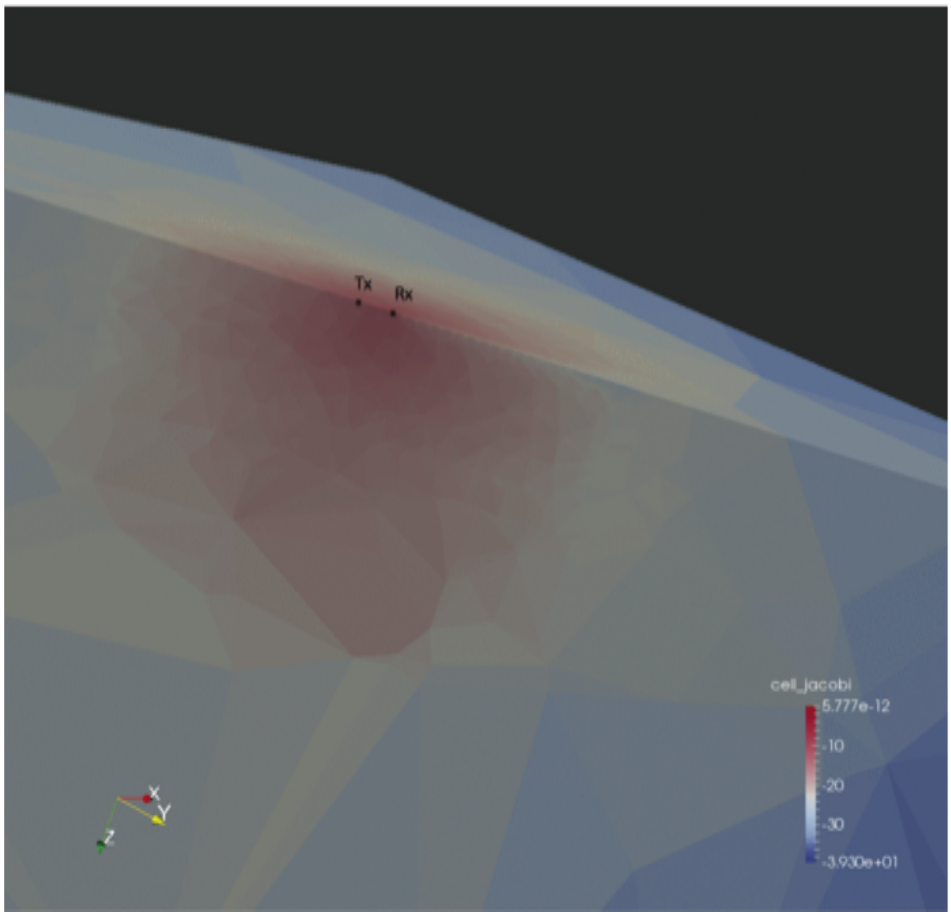

Figure 3.2: The sensitivity distribution of the Jacobian for a specific transmitter and receiver pairs. A horizontal cut along the seafloor and a vertical cut alone the Tx-Rx line have been carried out to expose the interior of the mesh. Warm color means the change of the conductivity of the parameter will have a stronger influence on the field than the change in the cold color area.

3.2.3 Regularization: Model Roughness as Penalty

Reconstruction of the subsurface electric conductivity based alone on data misfit is known to be unstable [Newman and Alumbaugh, 1997]. The regularization functional R(m) is introduced to stabilize the inversion and to provide information for parts of the model which are not or poorly resolved by the data. The model roughness operator R stabilizes the inversion by providing a measure of the model roughness, so that its minimization will steer the inversion away from producing spurious structures.

To derive smoothness operators on unstructured meshes within the finite element framework, we introduce the L_2 norm to measure the roughness of the model.

$$||R(m)||^2 = \int_{\Omega} \nabla m \cdot \nabla m \quad d\Omega \tag{3.9}$$

Here, the gradient dot product is integrated over the model domain.

In order to discretize the regularization functional, we recall that the electrical conductivity is assumed to be an element-wise constant.

$$\mathbf{m} = \sum_{k=1}^{n_c} m_k \lambda_k \tag{3.10}$$

where $m_k = log_{10}\sigma_k$ and λ_k is the basis function of the k_{th} element, that is, $\lambda_k = 1$ on k and $\lambda_k = 0$ on Ω / Ω_k. Afterwards, we could derive the discretized form of the smoothness opeartor:

$$||\mathbf{Rm}||^2 = \sum_{i=1}^{m} V_i [\sum_{j=1}^{N(i)} \omega_j (\frac{\Delta \mathbf{m}_{ij}}{\Delta r_{ij}})^2] \tag{3.11}$$

where

$$\Delta \mathbf{m}_{ij} = m_i - m_j \tag{3.12}$$

$$\Delta r_{ij} = \sqrt{(x_i - x_j)^2 + (y_i - y_j)^2 + (z_i - z_j)^2} \tag{3.13}$$

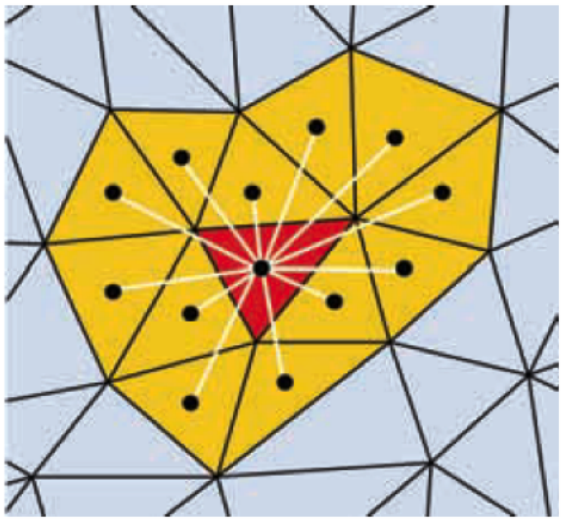

Figure 3.3: The roughness penalty for the central parameter (red triangle) is computed using a weighted sum of first differences within the ring of surrounding parameters (yellow triangles) according to equation 3.9

$$\omega_j = \frac{V_j}{\sum_{k=1}^{N(j)} V_k} \tag{3.14}$$

V_j is the volume of parameter i and accounts for the integration over the parameter region. N(j) is the set of all neighboring parameters. The neighboring concept shown in the 2D case in Fig. 3.3, can also be transferrable in 3D, where we define two elements sharing the edges or faces to be neighbors. The term in square brackets in eq. (3.11) approximates the L_2 norm of the roughness of the j_{th} parameter, using a volume weighted average of the conductivity differences among its neighboring elements, as shown in Fig 3.3. The distance Δr_{ij} between parameters is computed using the parameter centroids. This is easily implemented using sparse arrays format, so that computing $R^T R$ consumes an insignificant amount of time.

3.2.4 Bounding the Model Parameters

The model update eq. 3.2 does not place any constraints on the range of values that a parameter can take, yet often there are geological reasons or ancillary data sets that

suggest the conductivity will be within a certain range of values. When such inequality constraints are desired, they can be implemented simply by recasting the inverse problem using a non-linear transformation of the model parameters, so that the objective function and optimization algorithm remain essentially the same as the unconstrained problem. The model parameter m is bounded as

$$l < m(x) < u \tag{3.15}$$

while the transformed parameter x is unbounded

$$-\infty < x(m) < \infty \tag{3.16}$$

With the transformed model vector x, the model update is accomplished with a modified version of eq. 4.2.

$$\mathbf{x}_{k+1} = [\mu(\mathbf{R}^T\mathbf{R} + \mathbf{P}^T\mathbf{P}) + \mathbf{W}\mathbf{J}^{*T}\mathbf{W}\mathbf{J}^*]^{-1}[(\mathbf{W}\mathbf{J}^*)^T\mathbf{W}\hat{\mathbf{d}} + \mu\mathbf{P}^T\mathbf{P}\mathbf{m}_*] \tag{3.17}$$

with the modified data vector,

$$\hat{\mathbf{d}} = \mathbf{d} - \mathcal{F}(\mathbf{x}_k) + \mathbf{J}^*{}_k\mathbf{m}_k \tag{3.18}$$

$\mathbf{J}_k$ is the linearized model response gradient, or Jacobian matrix, defined as:

$$J^\star_{ij} = \frac{m_j}{x_j} J_{ij} \tag{3.19}$$

While an infinite number of transformations are possible for more restrictive double-sided inequality bounds, a common one is the introduced in [Habashy and Abubakar, 2004]. In fact, most EM inversion codes already use such a transform approach by inverting

for $log_{10}\sigma$ to avoid physically meaningless negative conductivities. Also, to avoid the under or over-penalizing on region where the model gradient changes fast, we introduce the bandpass transformation, which makes the transformed parameters identical to the original parameters within the range of the bounds:

$$\frac{\partial m}{\partial x} = \frac{1 - e^{c(l-u)}}{(1 + e^{-c(x-l)})(1 + e^{c(x-u)})} \tag{3.20}$$

where c is a constant that controls the decay of the scaling past the bounds. By setting c to be a function of the extent of the bounds, the shape of the transform shape can be made to be independent of the specific bounds. $c = 15/(u-l)$ has been found to work well in practice. Integrating this equation yields the expression for the bound model parameters:

$$m(x) = \frac{1}{c} log(\frac{1 + e^{c(l-x)}}{1 + e^{c(u-x)}}) + u \tag{3.21}$$

and

$$x(m) = \frac{1}{c} log(\frac{e^{c(m-l} - l)}{1 - e^{c(m-u)}}) + l \tag{3.22}$$

Between the bounds, the transformed parameters are identical to the original parameters, as desired, while the sensitivity scaling is flat between the passband with steep drop-offs beyond the bounds.

The bandpass transforms have been implemented in MARE3DEM, so that each model parameter can have its own unique bounds specified. For some data sets, the user will have a priori knowledge that can guide the use of a narrow range of parameter bounds in certain localized regions where nearby well logs provided independent constraints on conductivity. Narrow bounds could also be prescribed to test hypotheses about the range of permissible resistivity values that fit a given data set. Yet in most cases the inversion will be run without any bounds. However, experience has shown there to be

a benefit from applying global bounds on all model parameters, so that extreme values are excluded from the inversion. In particular, if the line search jumps to very low u values, the Occam model update can produce rough models that have unrealistically high and low resistivity. Bounding all parameters to a plausible range (such as 0.1 to 100,000 ohm-m for marine models) alleviates this situation. Another consequence is that unrealistically conductive regions can cause the adaptive mesh refinement scheme in the forward code to spend excessive effort refining the mesh to produce accurate responses in these regions. Therefore, bounding all the model parameters to a plausible range avoids unnecessary computational.

3.3 Synthetic Inversion Examples

For the following studies, synthetic data added with gaussian noise are inverted using Occam's method.

3.3.1 Half-space Model

The first synthetic example demonstrates the inversion aspects of MARE3DEM on the half-space model, described in Fig. 3.4. The model consists of two layers with a flat interface. The sea water layer has fixed model parameters, whereas the region with free parameters is underneath. Insides the free region, there is a region of interest where the size of the elements are finer than the outside region. The synthetic data is generated by a electric dipole with 0.1Hz frequency on a model where the resistivity of the free region equals to 5 $\Omega \cdot m$. CSEM forward response were generated for 20 receivers positioned every 500 m alone the seafloor.

Keeping the model's set-up unchanged, this section presents synthetic inversion studies that examine how the resolving capabilities of CSEM depend on the transmitted

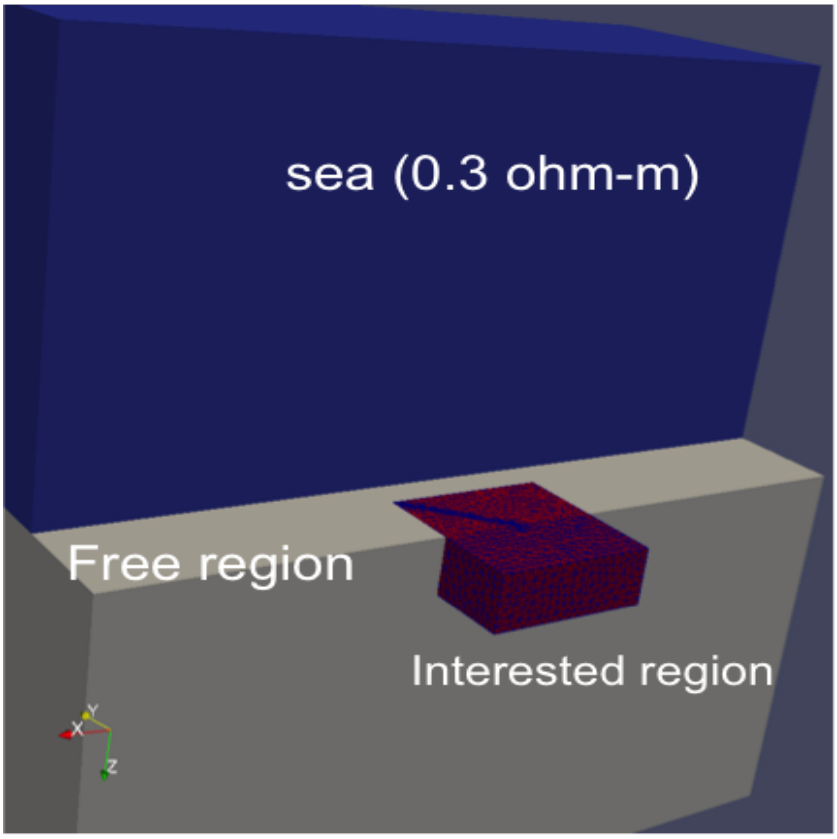

Figure 3.4: Half-space inversion test. In this two layered example, we have a transmitter pointing to the x axis. 20 receivers with 500m interval are deployed along the line x=y. For inversion, the sea layer has fixed resistivity, while the free region starts from resistivity equals to 100 $\Omega \cdot m$.

Table 3.1: Layout of the inversion experiments

Frequency	Amp	Log(AMP)
0.1 Hz	Experiment 1	Experiment 2
0.5 Hz	Experiment 3	Experiment 4

frequencies and the inverted data type. Table 3.1 summarise the experiments we are going to carried out for the half-space model.

1, Frequency: 0.1 Hz. Data type: $|E_x|$

We use the amplitude of the x component of the electric field as input. 1% random Gaussian noise was added to the data. In table 3.2, the first row shows the initial model and the corresponding RMS. As the inversion iteration goes on, the RMS continuously decrease to the target misfit, which is 1.0. For the final model at the 6th iteration, the resistivity could be bounded between 4.83 and 5.07 $\Omega \cdot m$, which is very close to the true value 5 $\Omega \cdot m$.

In the first stage of Occam algorithm when misfit is larger than the target misfit, the algorithm carries out a line search to find the value of μ that produces the model with the lowest misfit. The line search consists of two steps: first bracketing a minimum using a golden-section search, and then finding the minimum using Brent's method [Press et al., 1996]. In case the minimum search fails to find a model with a lower misfit, a reduced model step is taken and the line search is carried out again. Once the target misfit has been reached, Occam will seek the smoothest model by bracketing μ at the target misfit and then using interpolation to find the largest value of μ at the target misfit.

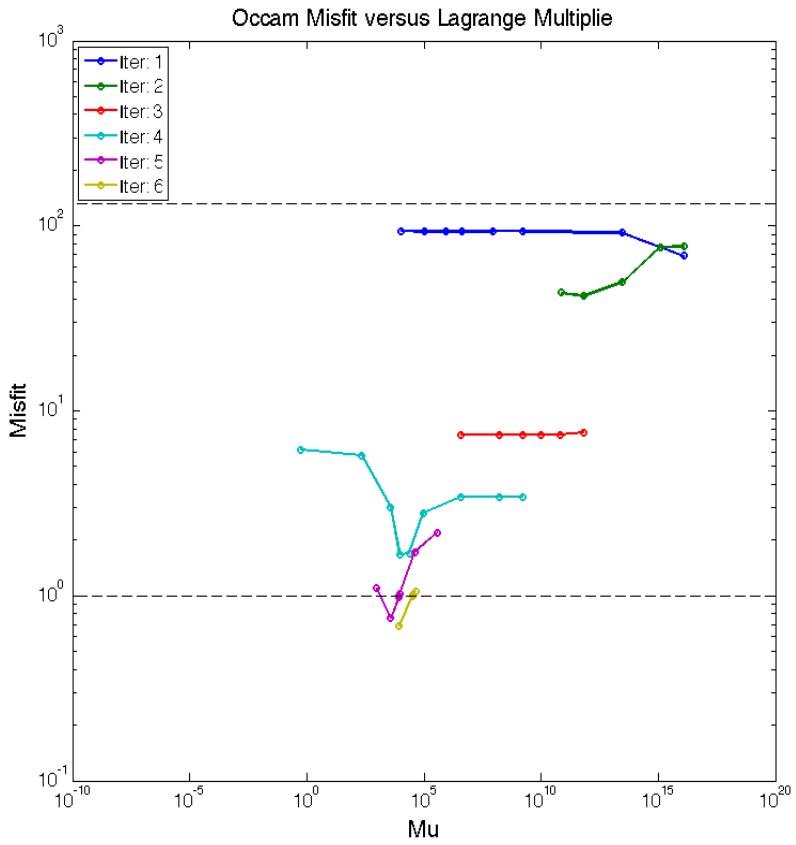

Figure 3.5: Convergence of the Regular Occam algorithms (1, Frequency: 0.1 Hz. Data type: $|E_x|$). Colored dots show the misfit for each forward call during the line search of each iteration.

Table 3.2: Resistivity, RMS and Model Roughness for each iteration (1, Frequency: 0.1 Hz. Data type: $|E_x|$).

No. Iteration	Resistivity	RMS	Model Roughness
1	100	132.31	.2486E-19
2	[8.48, 8.48]	68.98	0.1141E-13
3	[4.55, 4.55]	7.405	0.5500E-08
4	[4.15, 6.62]	1.67	3.88
5	[4.56, 5.30]	0.9997	0.91
Final Model	[4.83, 5.07]	0.9996	0.1117

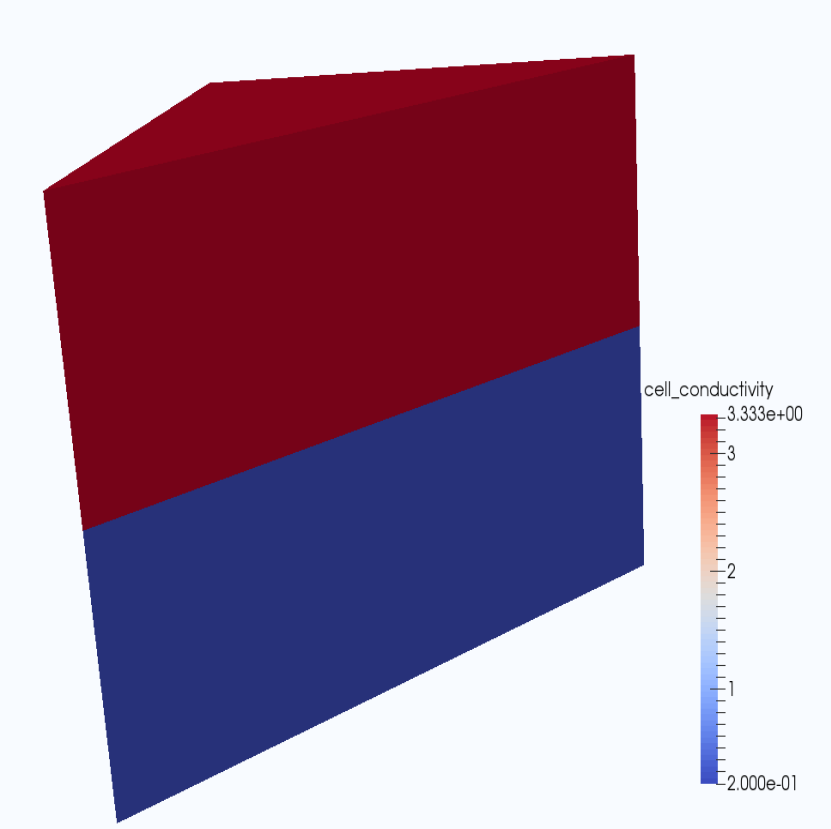

Figure 3.6: Inverted model for the two layered model. The top layer has fixed conductivity 3.3 s/m, while the free region has the inverted conductivity close to 0.2 s/m. Since the true model is half space, the invert result is also very smooth.

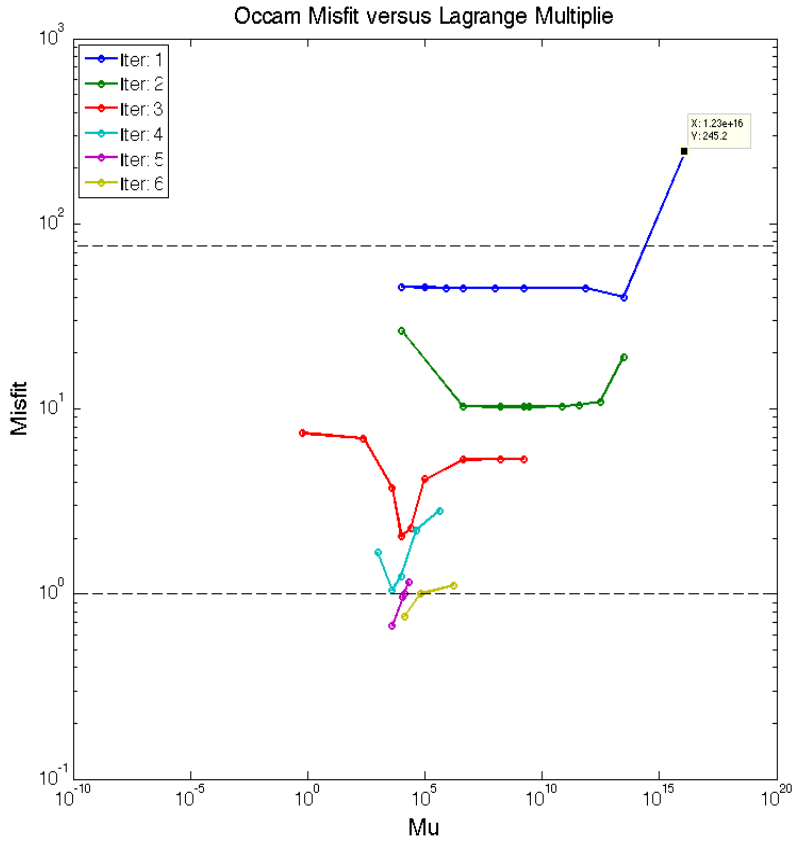

Figure 3.7: Convergence of the Regular Occam algorithms (2, Frequency: 0.1 Hz. Data type: Log($|E_x|$)). Colored dots show the misfit for each forward call during the line search of each iteration.

2, Frequency: 0.1 Hz. Data type: Log($|E_x|$)

We use the Log(amplitude) of the x component of the electric field as data. 1% random Gaussian noise was added to the data. In table 3.3, the first row shows the initial model and the corresponding RMS. As the inversion iteration goes on, the RMS continuously decrease to the target misfit, which is 1.0. In our example, the inversion starts from RMS=76.17 and ends below the target misfit of 1.0. At RMS = 0.997, the resistivity of the free region is bracket between 4.90 $\Omega \cdot m$ and 5.02 $\Omega \cdot m$, which is very close to the true value 5 $\Omega \cdot m$.

Table 3.3: Resistivity, RMS and Model Roughness for each iteration (2, Frequency: 0.1 Hz. Data type: Log($|E_x|$)).

No. Iteration	Resistivity	RMS	Model Roughness
1	100	76.17	0.7667E-18
2	[10.12, 10.12]	40.02	0.7741E-08
3	[4.17, 6.44]	10.27	6.868
4	[4.29, 5.53]	2.04	2.826
5	[4.67, 5.23]	1.05	0.455
Final Model	[4.90, 5.02]	0.997	0.026

Table 3.4: Resistivity, RMS and Model Roughness for each iteration (3, Frequency: 0.5 Hz. Data type: $|E_x|$).

No. Iteration	Resistivity	RMS	Model Roughness
1	100	3326.6	0
2	[714.49, 714.49]	1021	0.1953E-16
3	[92.21, 92.21]	68.93	0.1951E-18
4	[3.04, 3.04]	64.98	0.6039E-17
5	[3.20, 3.20]	61.80	0.6782E-17
6	[3.21, 3.21]	61.71	0.7345E-17
...	...	...	...
Final Model	[4.84, 5.09]	1.000	0.060

Compared with the previous example using $|E_x|$ as data, the inverted result using Log($|E_x|$) is better in two ways. First, the bracketed resistivity range is tighter around the true value and the final model is more smooth.

3, Frequency: 0.5 Hz. Data type: $|E_x|$

In this example, we change the transmitter's frequency to 0.5 Hz. As the first experiment, we use the amplitude of the x component of the electric field as input. 1% random Gaussian noise was added to the data. In table 3.4, the first row shows the initial model and the corresponding RMS. As the inversion iteration goes on, the RMS continuously decrease to the target misfit, which is 1.0. For the final model at the 6th iteration, the resistivity could be bounded between 4.84 and 5.09 $\Omega \cdot m$, which is very close to the true value 5 $\Omega \cdot m$.

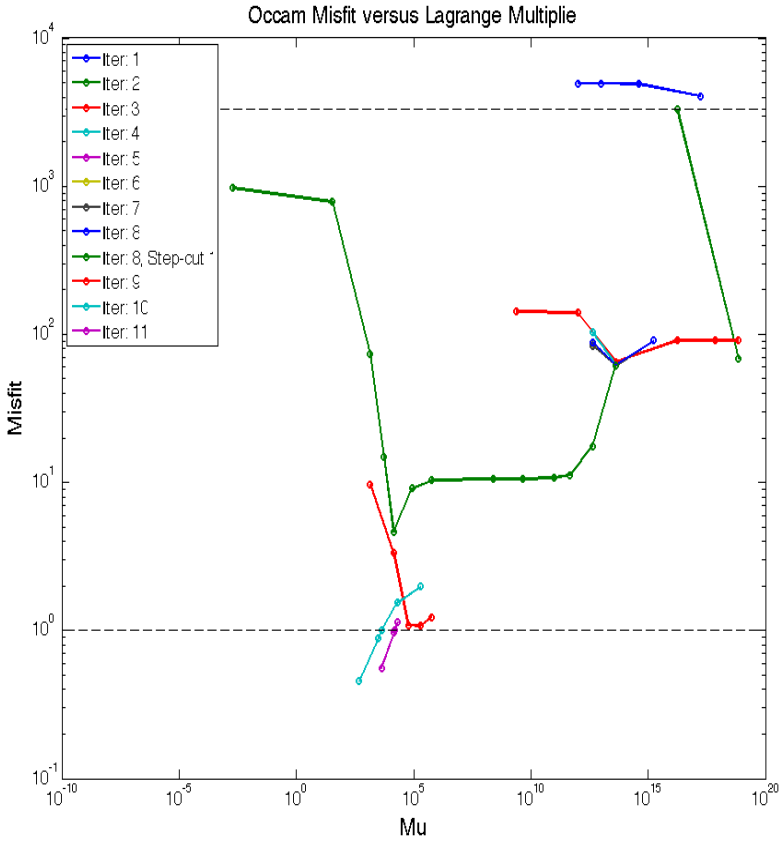

Figure 3.8: Convergence of the Regular Occam algorithms (3, Frequency: 0.5 Hz. Data type: $|E_x|$). Colored dots show the misfit for each forward call during the line search of each iteration.

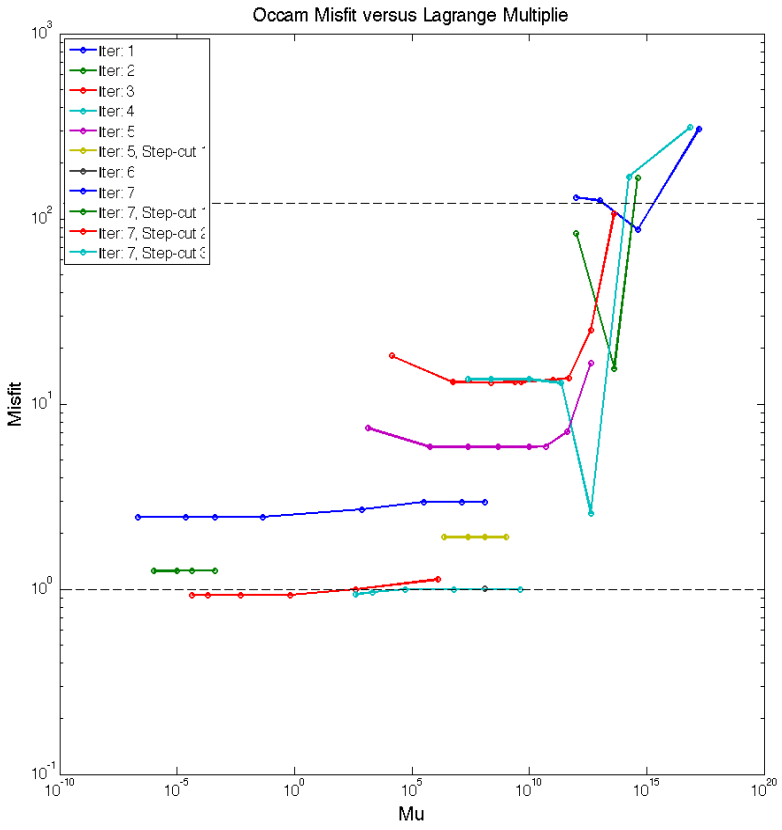

Figure 3.9: Convergence of the Regular Occam algorithms (4, Frequency: 0.5 Hz. Data type: Log($|E_x|$)). Colored dots show the misfit for each forward call during the line search of each iteration.

4, Frequency: 0.5 Hz. Data type: Log($|E_x|$)

We use the Log(amplitude) of the x component of the electric field as input. 1% random Gaussian noise was added to the data. In these two example where the transmitted frequency is increased to 0.5 Hz from 0.1 Hz. When Occam's inversion converge, all of the tests could constrain the resistivity of the free region around the true model. For both frequency, using Log($|E_x|$) as data provides a better results, in terms of the model smoothness and the resistivity value.

Table 3.5: Resistivity, RMS and Model Roughness for each iteration (4, Frequency: 0.5 Hz. Data type: Log($|E_x|$)).

No. Iteration	Resistivity	RMS	Model Roughness
1	100	121.50	0
Final Model	[4.99, 4.99]	0.9980	0.7101E-09

Table 3.6: Multiple frequency example: Resistivity, RMS and Model Roughness for each iteration (5, Frequency: 0.3 Hz + 0.05 Hz. Data type: Log($|E_x|$)).

No. Iteration	Resistivity	RMS	Model Roughness
1	100	40.07	0
Final Model	[4.99, 4.99]	0.62	0.1749E-15

5, Frequency: 0.3 Hz + 0.05 Hz. Data type: Log($|E_x|$)

In this example, instead of inverting single frequency, we test the multiple frequencies inversion behavior using Log($|E_x|$) as data. As is seen from the result, inversion converges with only 4 iterations and the constrained model is extremely smooth with resistivity at 4.99 $\Omega \cdot m$.

In the 1D layered example, we have a line of receiver and a single transmitter. Amplitude in $\log_{10}$ scale is proved to be advantageous.

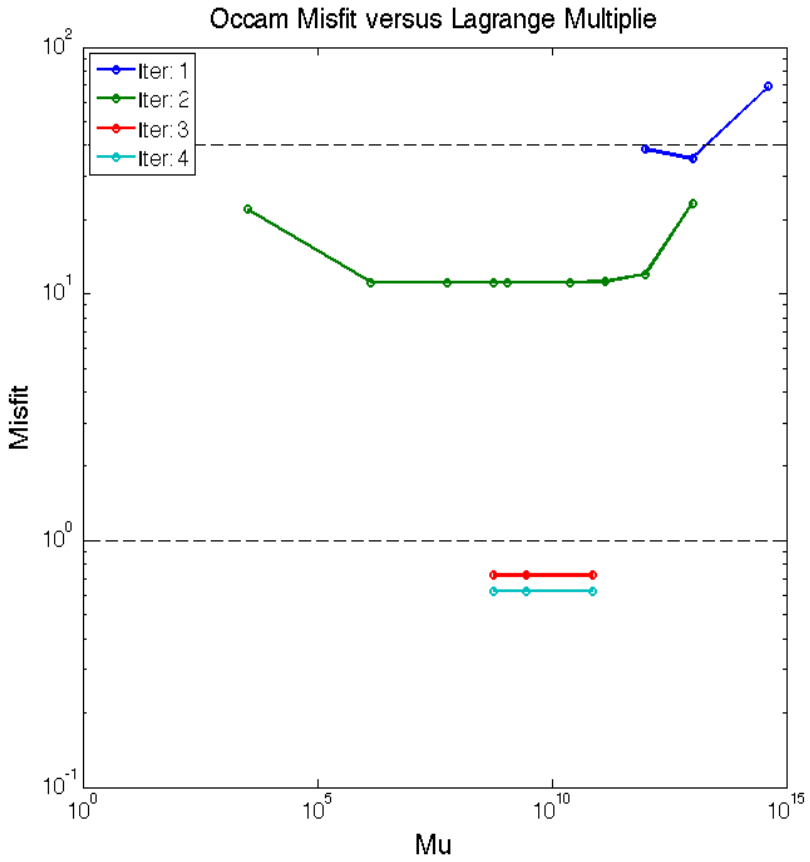

Figure 3.10: Convergence of the Regular Occam algorithms (5, Frequency: 0.3 Hz + 0.05 Hz. Data type: Log($|E_x|$)). Colored dots show the misfit for each forward call during the line search of each iteration.

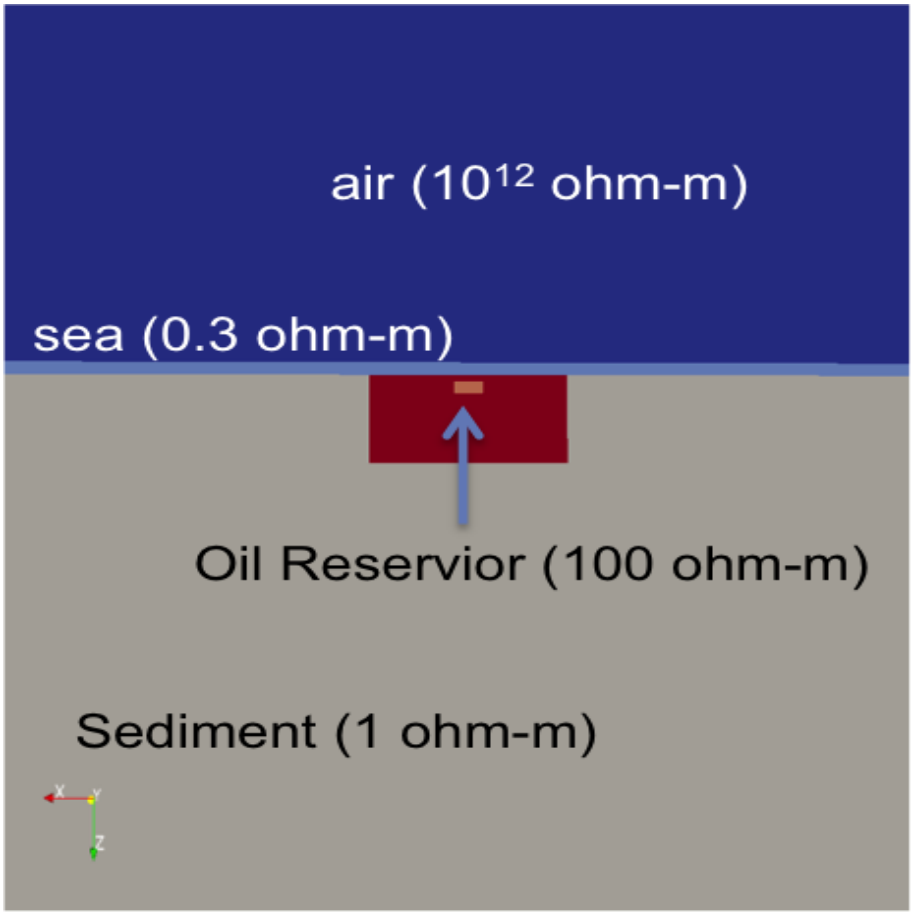

Figure 3.11: Oil reservoir model.

3.3.2 Model with Reservoir

In the second example, the air layer and sea layer are region with fixed parameters. In the free region, there is a resistive oil reservoir at 2km depth. For the following examples, we choose to use the log form of the amplitude data, which is also proved to have better performance in [Wheelock et al., 2015]. We first start the experiment with similar setting as the 1D example: single transmitter and line receivers. As we progressively change the setting of the experiments, the inversion result will be improved gradually.

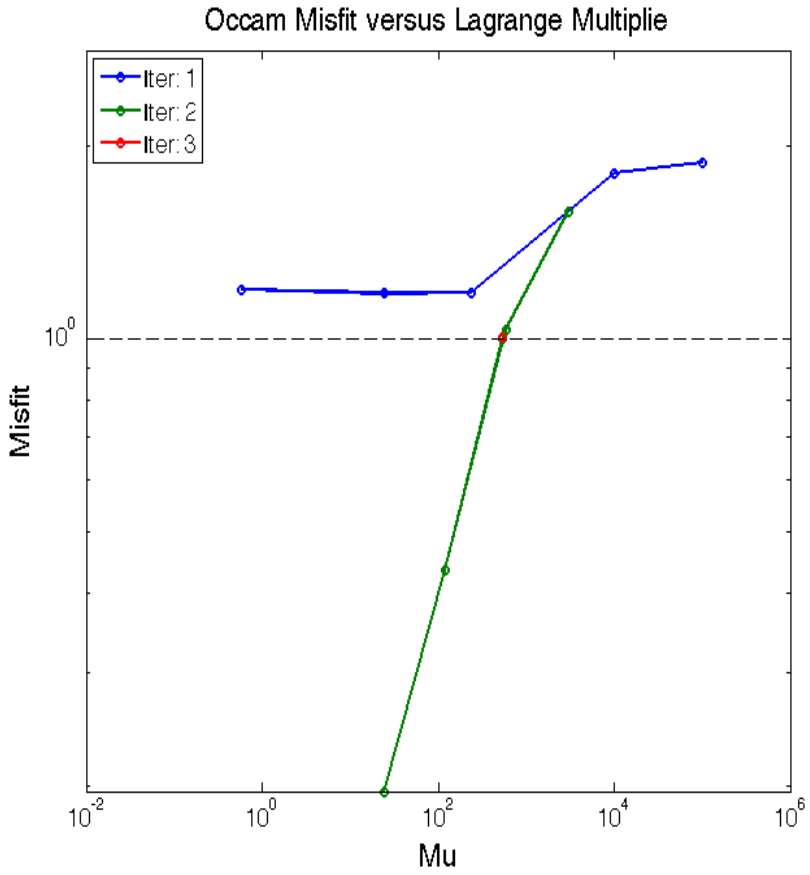

Figure 3.12: Convergence of the Regular Occam algorithms (1, Log(Amplitude) + line receivers + single transmitter

1, Log(Amplitude) + line receivers + single transmitter

As the initial step, we use a single transmitter and a line of receivers to try to illuminate the target. The data include the amplitude of the $|E_x|$ in log_{10} scale. Standard error is this case is $\sigma = 3\%$.

From Fig. 3.12, we can see that inversion converge after 3 iterations. However, the target is poorly imaged (see from Fig. 3.13). This is due to the fact that the source-receiver geometry does not have good sensitivity to the target. For the following example, we will replace the receivers' line by a receivers' grid.

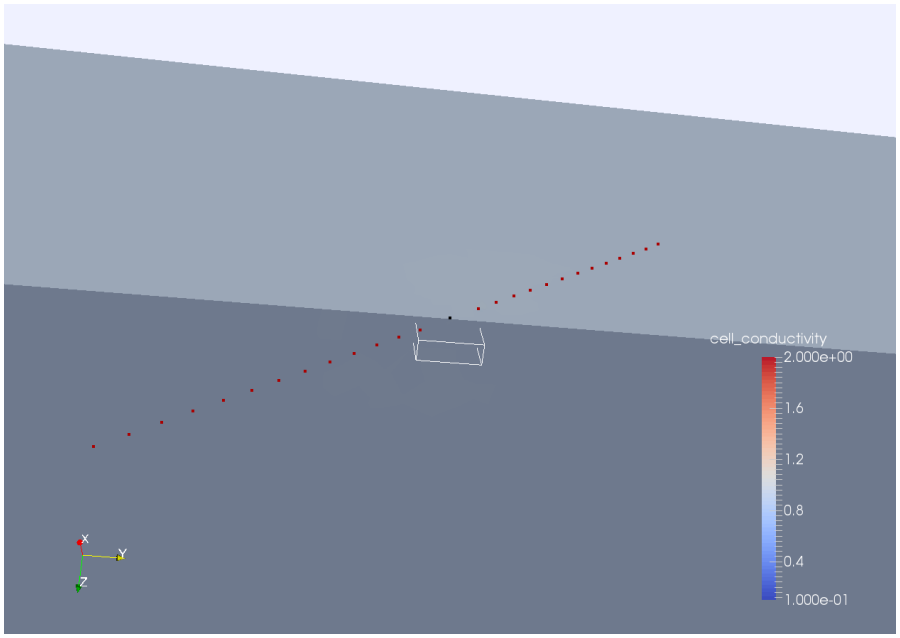

(a) Inverted model for the line receivers example. Result are shown in the original color scale.

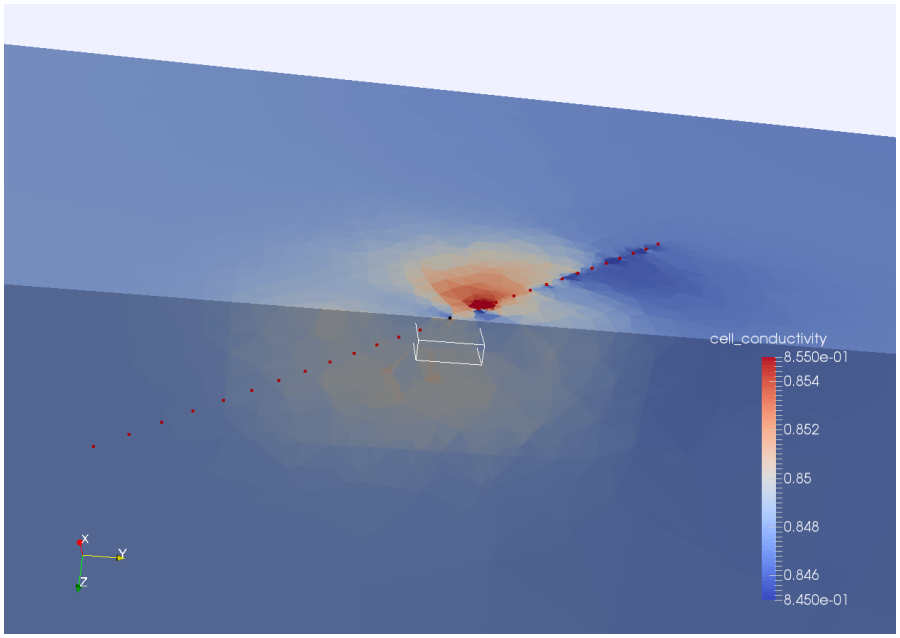

(b) Inverted model for the line receivers example. Same result as the above plot, shown in different color scale to magnify the contrast.

Figure 3.13: Inverted result for the oil reservoir model with line receivers. In this example, there are one transmitter and a line of receivers.

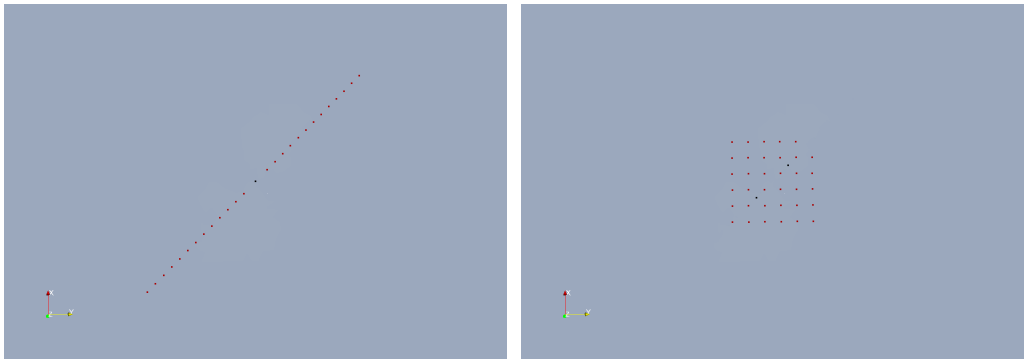

(a) Single transmitter and receivers line (b) Double transmitter and receivers grid

Figure 3.14: In the line receiver example, there are 26 receivers with 1km interval. The single transmitter are 50 m above the seafloor with 0.1 Hz. In the receiver grid example, we deployed 35 receivers on the seafloor, covering 10 km by 10 km area. There are two 0.1 Hz transmitters in this model.

2, Log(Amplitude) + receivers grid + double transmitter

The data include only amplitude of the Log($|E_x|$). Standard error is this case is $\sigma = 3\%$. Fig 3.14 shows the source and receivers location of the line and grid model. For the receiver grid model, we include two transmitters.

As we could see from Fig 3.16, the inversion result has been improved and source receivers lay-out is more sensitive to the region of interest. To further constrain the location of the oil reservoir, we add phase data into the inversion.

3, Log($|E_x|$) + Phase + receivers grid + double transmitter

Based on the setting of the previous experiment, we add the phase information into the data before inverting the model. From the convergence plot (Fig. 3.21), inversion converge with 14 iterations. It takes longer to reach the target RMS, but each iteration could arrive at a lower misfit, compared with the previous iteration. The intermediate and final model are shown in Fig 3.19 and Fig 3.20. The decreasing RMS misfit as a function of Occam iteration for the oil reservoir model are shown in Fig 3.18.

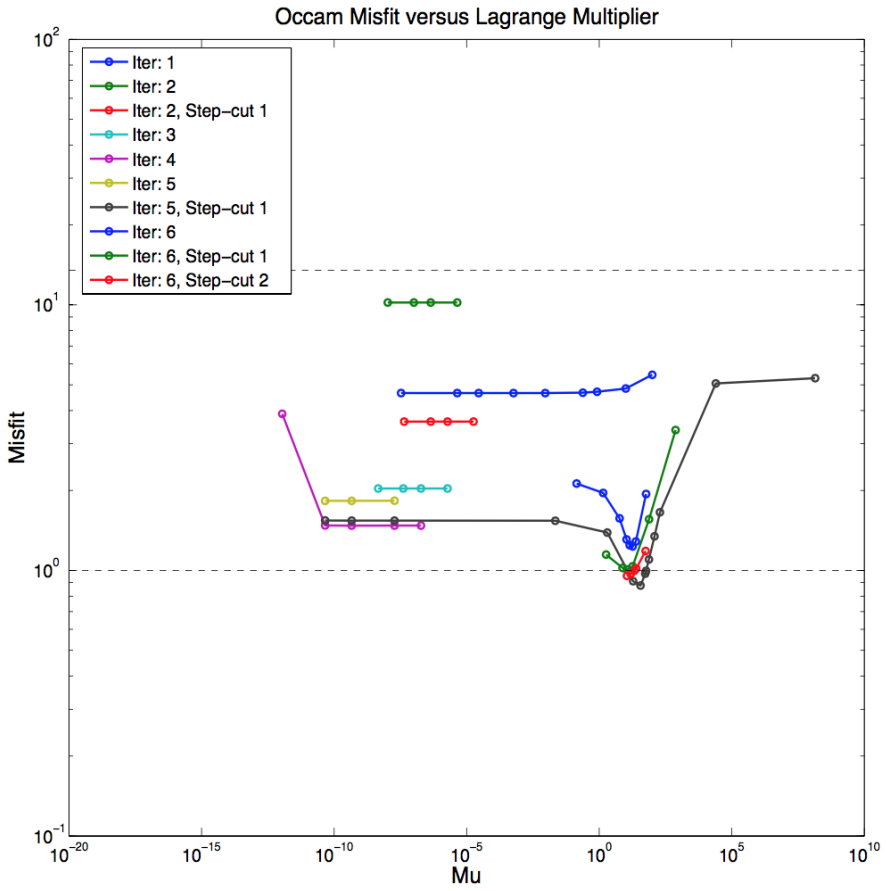

Figure 3.15: Convergence of the Regular Occam algorithms (2, Log(Amplitude) + receivers grid + double transmitter).

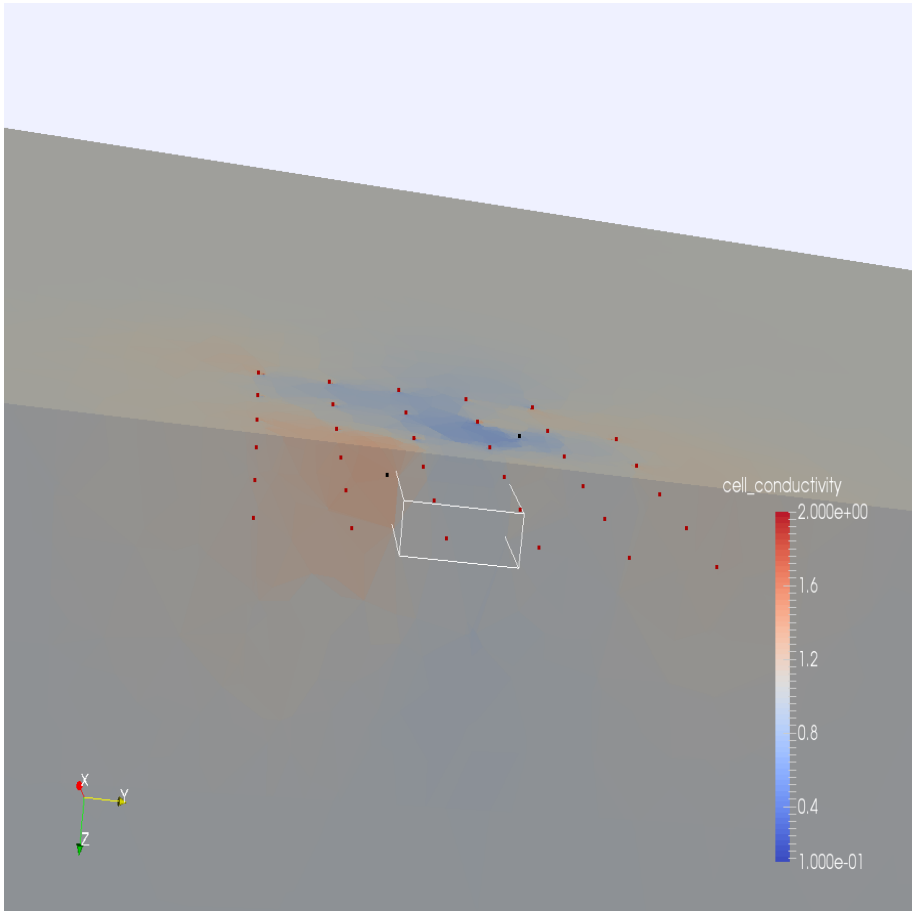

Figure 3.16: Inverted result for the oil reservoir model with receivers grid. (2, Log(Amplitude) + receivers grid + double transmitter).

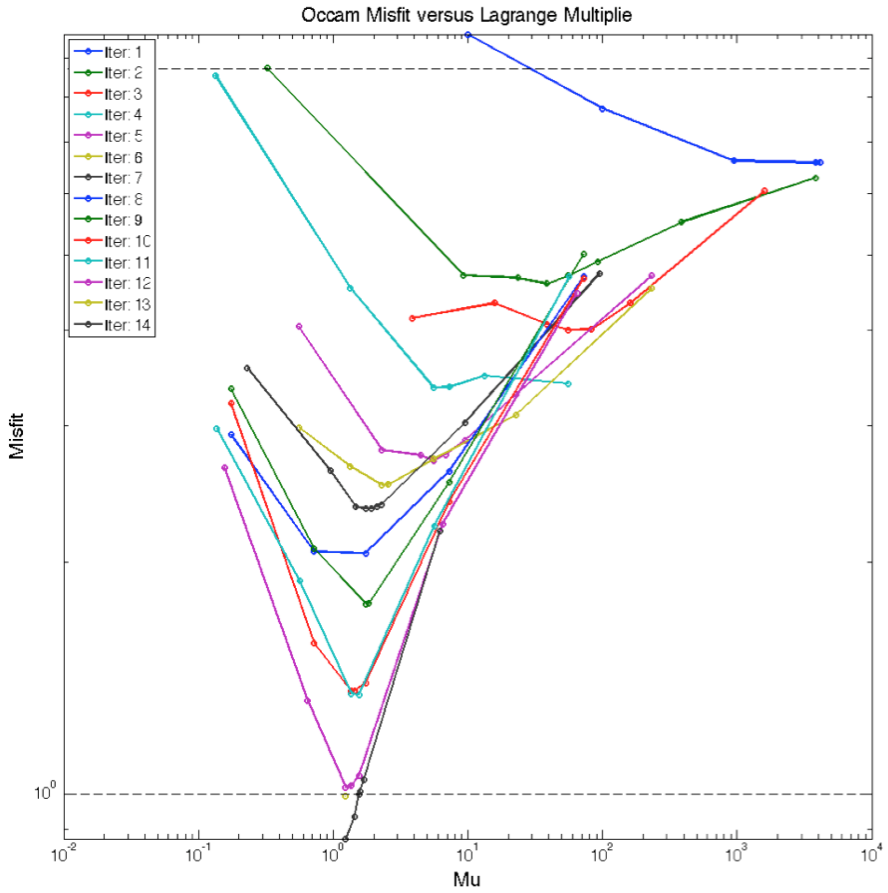

Figure 3.17: Convergence for the oil reservoir model: Experiment 3

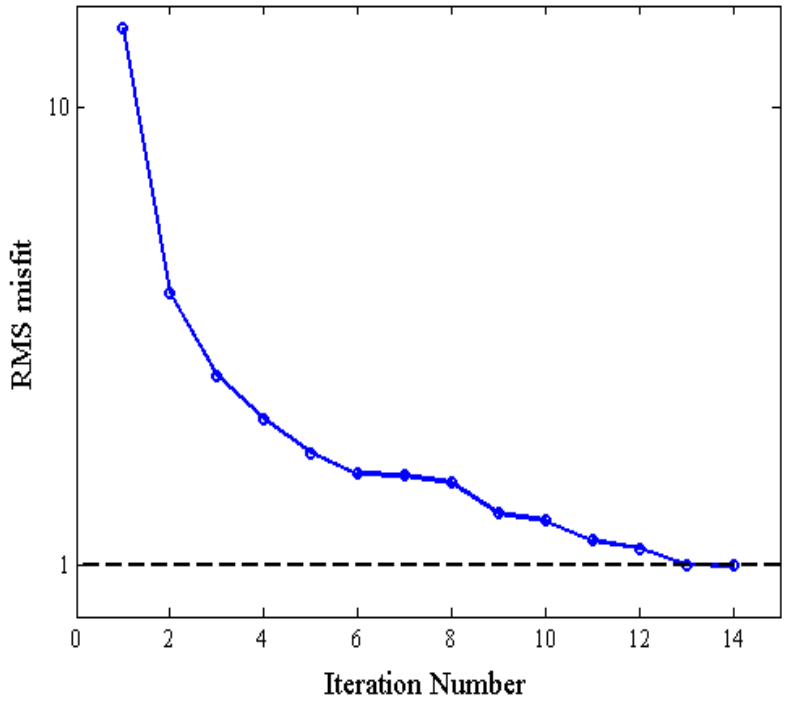

Figure 3.18: RMS misfit shown as a function of Occam iteration for the oil reservoir model.

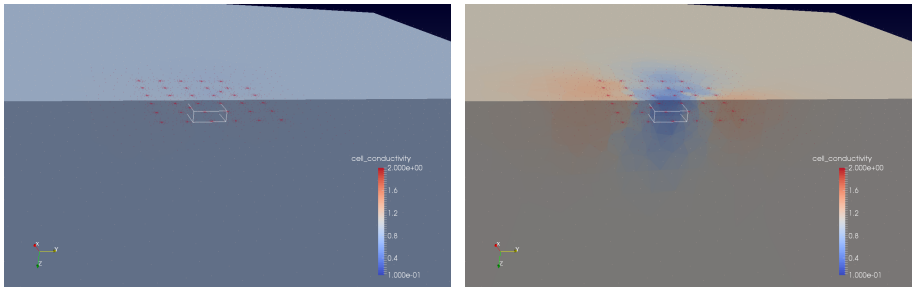

(a) Initial model

(b) 2nd iteration

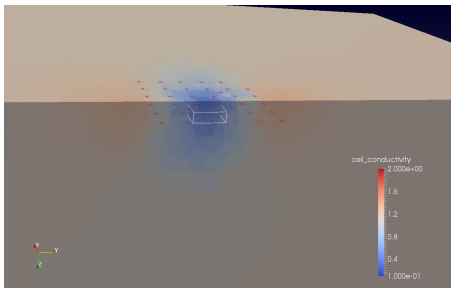

(c) 3rd iteration

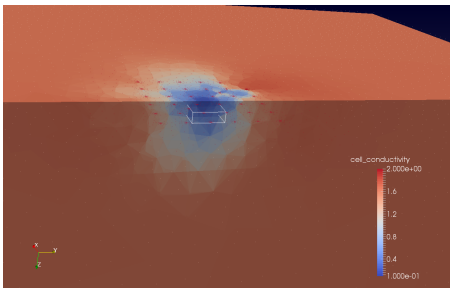

(d) 4th iteration

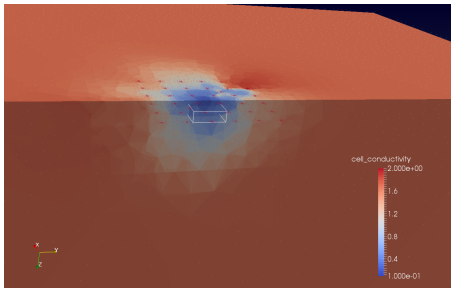

(e) 5th iteration

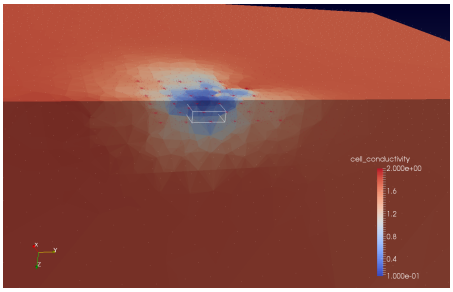

(f) 6th iteration

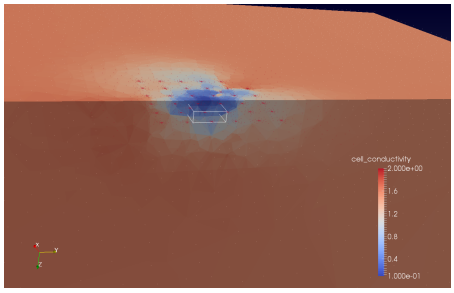

(g) 7th iteration

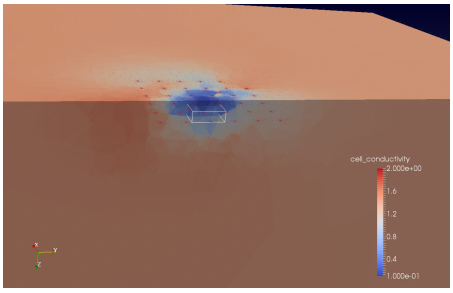

(h) 8th iteration

Figure 3.19: Inverted result for each iteration of the oil reservoir model with receiver grid: from iteration 1 to 8

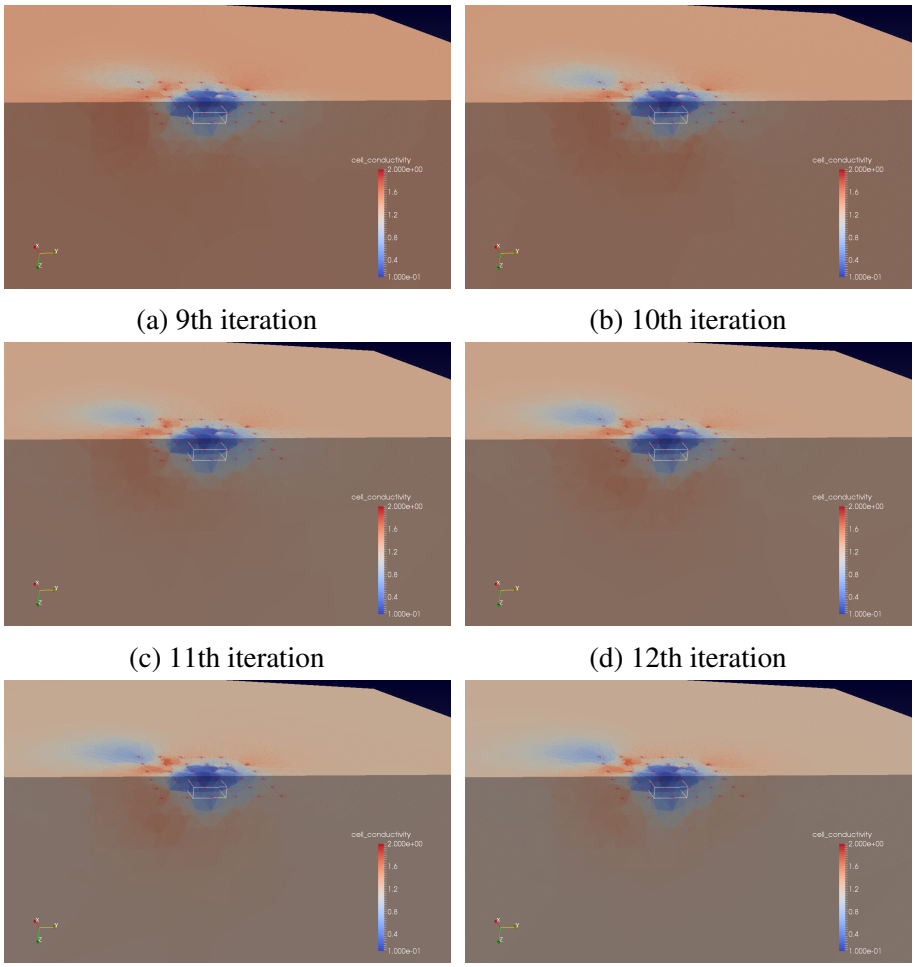

(a) 9th iteration (b) 10th iteration

(c) 11th iteration (d) 12th iteration

(e) 13th iteration (f) 14th iteration

Figure 3.20: Inverted result for each iteration of the oil reservoir model with receiver grid: from iteration 9 to 14

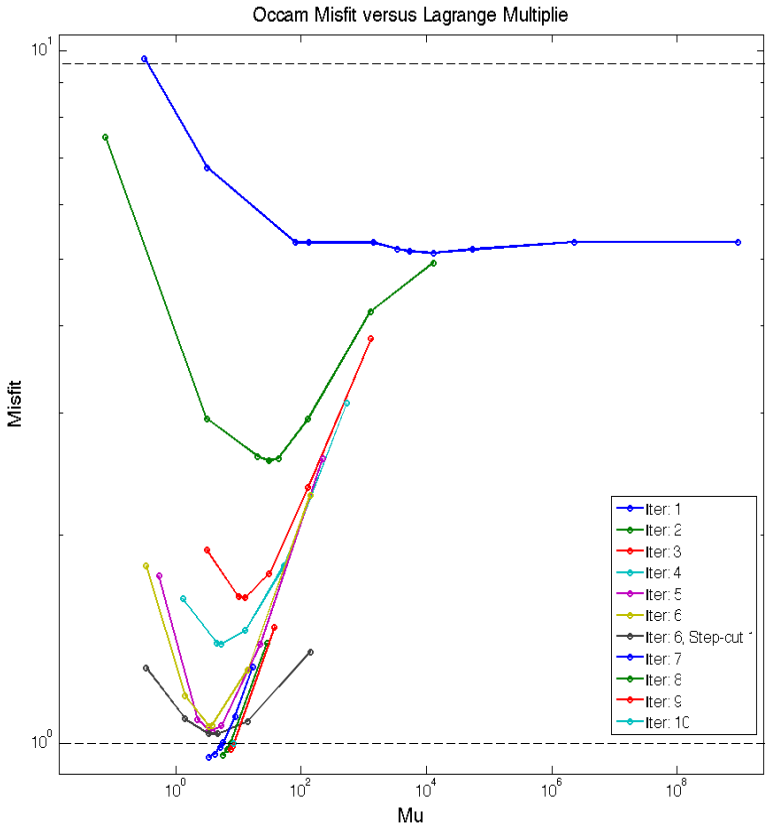

Figure 3.21: Convergence for the oil reservoir model with bathymetry.

3.3.3 Model with Reservoir and bathymetry

In the third model, we integrate the bathymetry of the seafloor into the model. Based on the previous results, we employ Log($|E_x|$) and Phase as data. The receivers grid are 6 by 6, covering an area of 10km by 10km with 2 km interval between each receivers. The resistivity body buried at 3600m depth with 100 $\Omega \cdot m$ resistivity. It has such dimension [4,4,1.7] km alone the x,y,z direction.

Fig. 3.25 and Fig. 3.26 shows the horizontal variation of the final inverted model. Slice cuts happen at different horizontal offsets. Fig. 3.27 and Fig. 3.28 shows the vertical variation of the final inverted model. Slice cuts happen at different vertical depth.

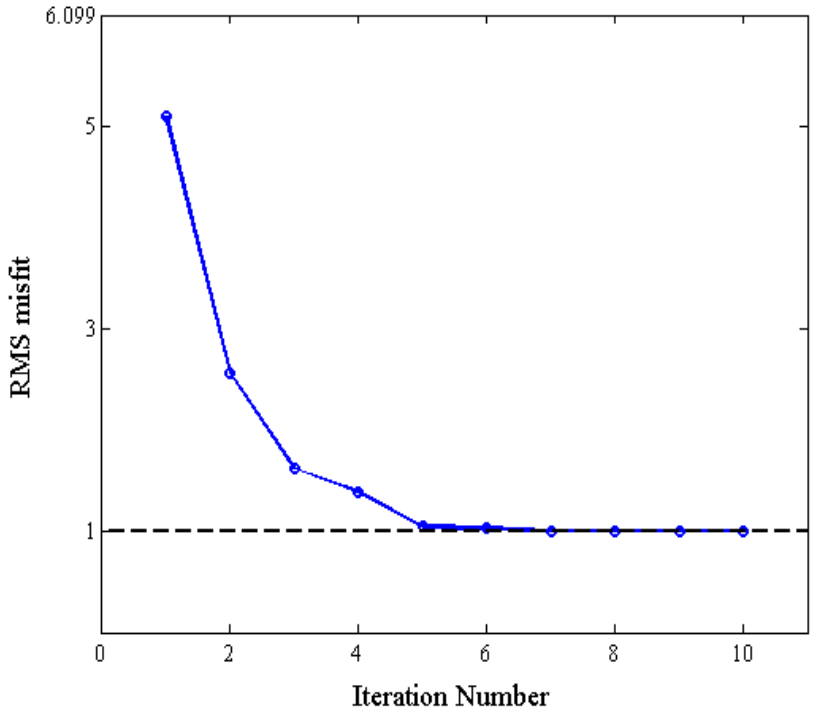

Figure 3.22: RMS misfit shown as a function of Occam iteration for the bathymetry model.

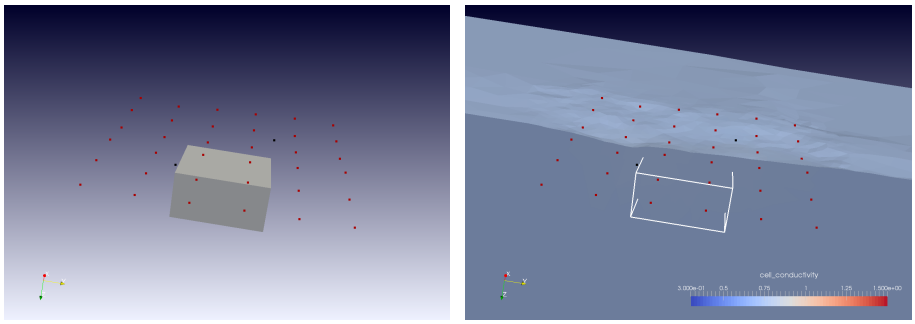

(a) Initial model

(b) 2nd iteration

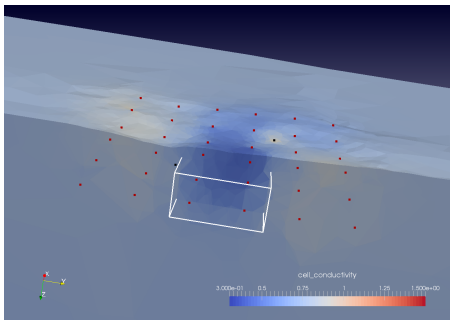

(c) 3rd iteration

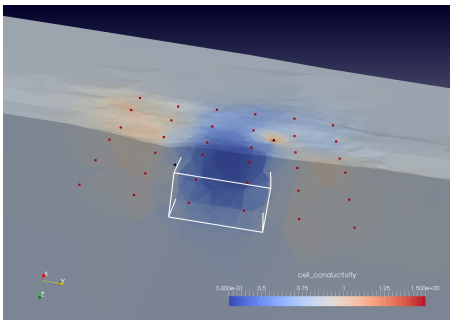

(d) 4th iteration

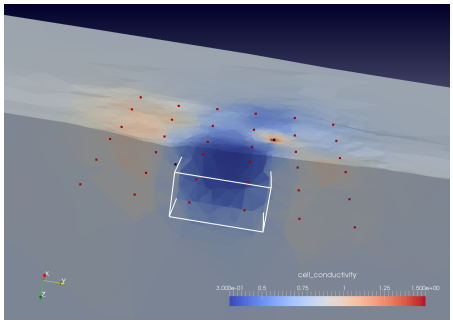

(e) 5th iteration

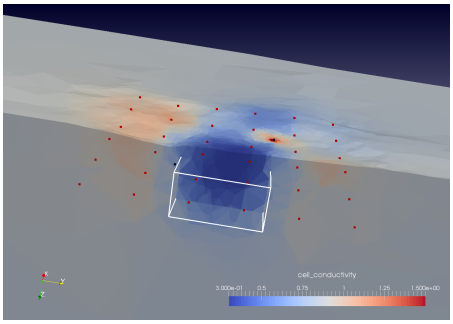

(f) 6th iteration

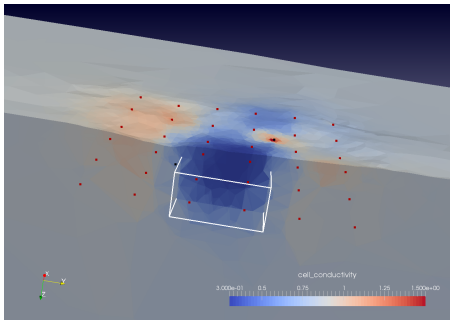

(g) 7th iteration

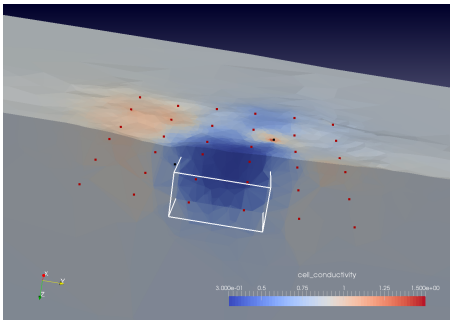

(h) 8th iteration

Figure 3.23: Inverted results for each iteration of the model with bathymetry: from iteration 1 to 8

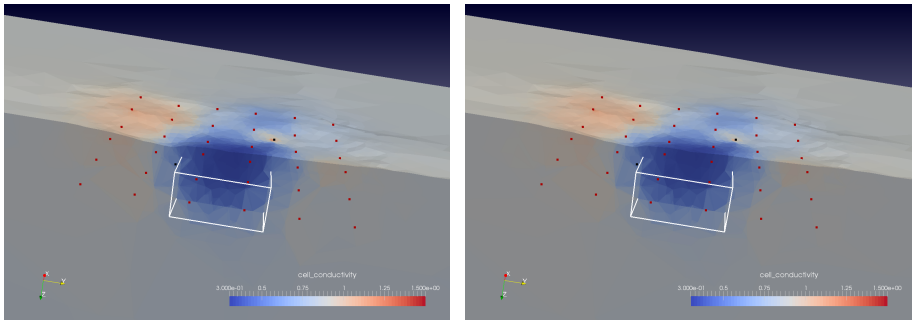

(a) 9th iteration (b) 10th iteration

Figure 3.24: Inverted results for each iteration of the model with bathymetry: from iteration 9 to 10

3.3.4 Conclusion

The MARE3DEM modeling method presented here can readily accommodate complex geological structure such as seafloor topography and seismically imaged strata. The receivers and transmitters can be located anywhere in the model, allowing for simulating the physical behavior of EM fields in various situation. Highly accurate EM responses are calculated based on the final optimized mesh generated by using the goal-oriented adaptive mesh refinement. This removes the question of how to manually design the optimal mesh. The topography can be included as precisely as it is known. MATLAB functions and subroutine allow users to create forward models with complex surfaces with ease. Dual grid strategy realizes a flexible and efficient parameterization for 3D inversion, which allows inversion parameters to be concentrated where needed while the outer regions of the model can be much more coarsely discretized. Unlike most regularized inversion algorithms, the value of the trade-off parameter between data misfit and model roughness do not need to be determined in advance.

Synthetic example shows the reliability and potential of the current implementation. To visualize the inversion results, paraview provides powerful visualization capabilities. Field amplitude in Log scale is proved to be more effective to find the target. Source and receiver coverage is also essential for imaging the target properly. Moreover,

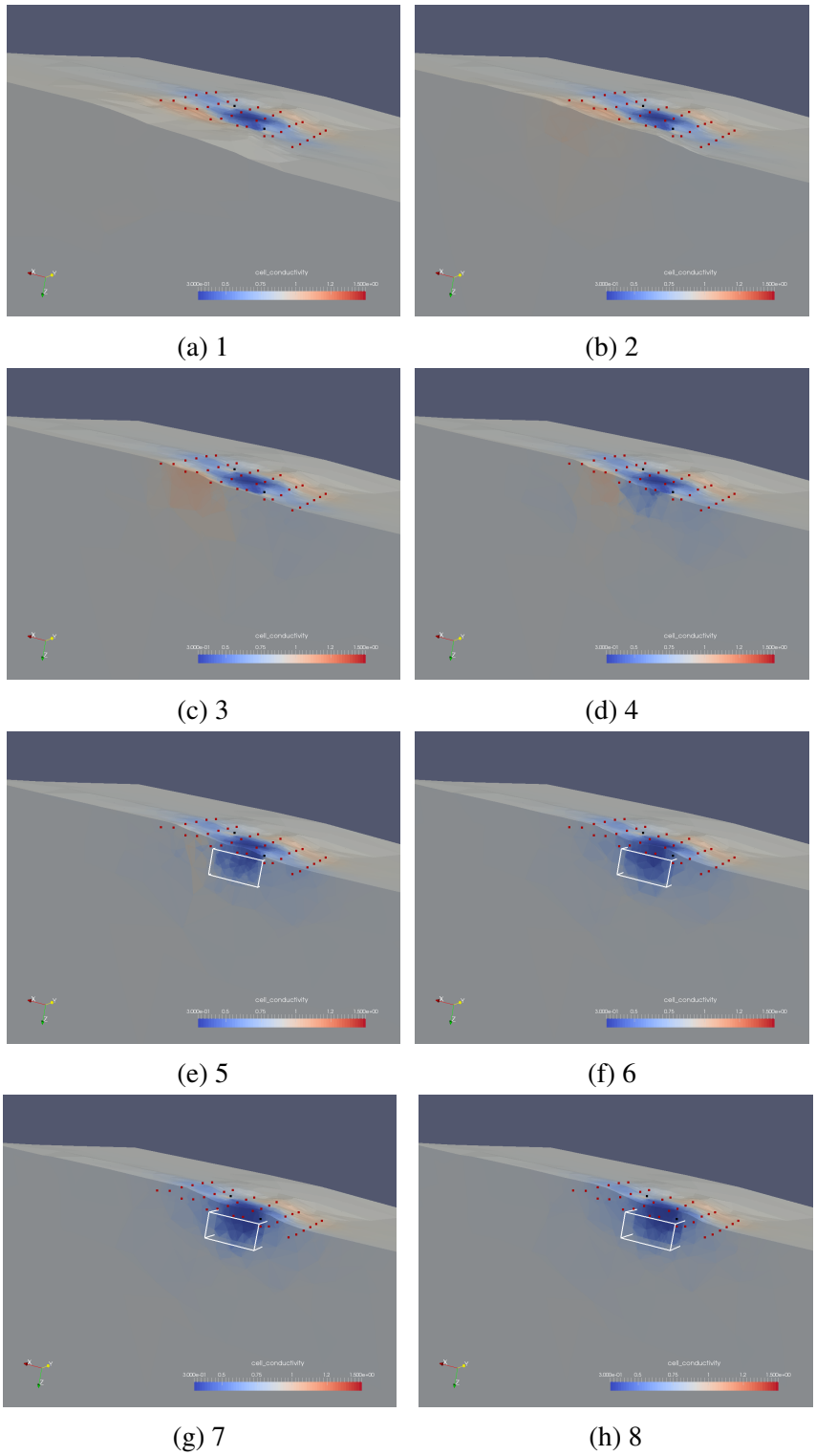

(a) 1 (b) 2

(c) 3 (d) 4

(e) 5 (f) 6

(g) 7 (h) 8

Figure 3.25: Lateral variation of the final model: from offset 1 to 8

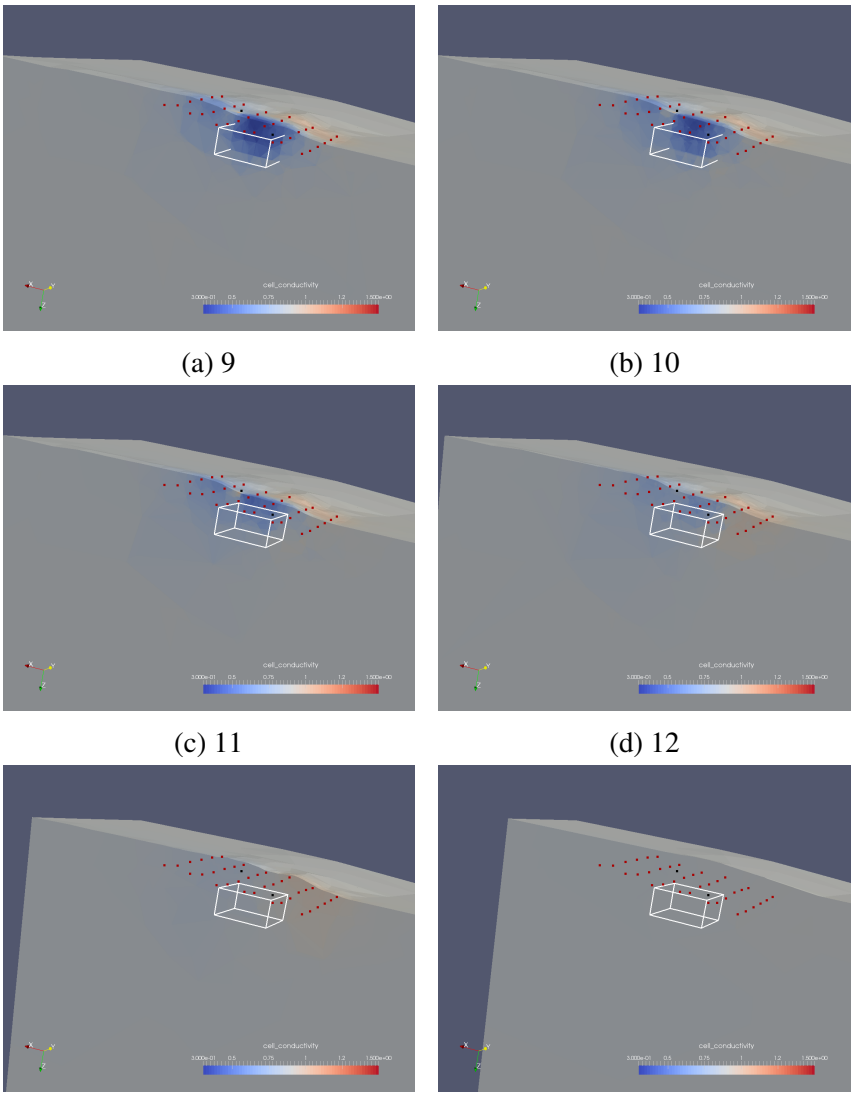

(a) 9 (b) 10

(c) 11 (d) 12

(e) 13 (f) 14

Figure 3.26: Lateral variation of the final model: from offset 9 to 14

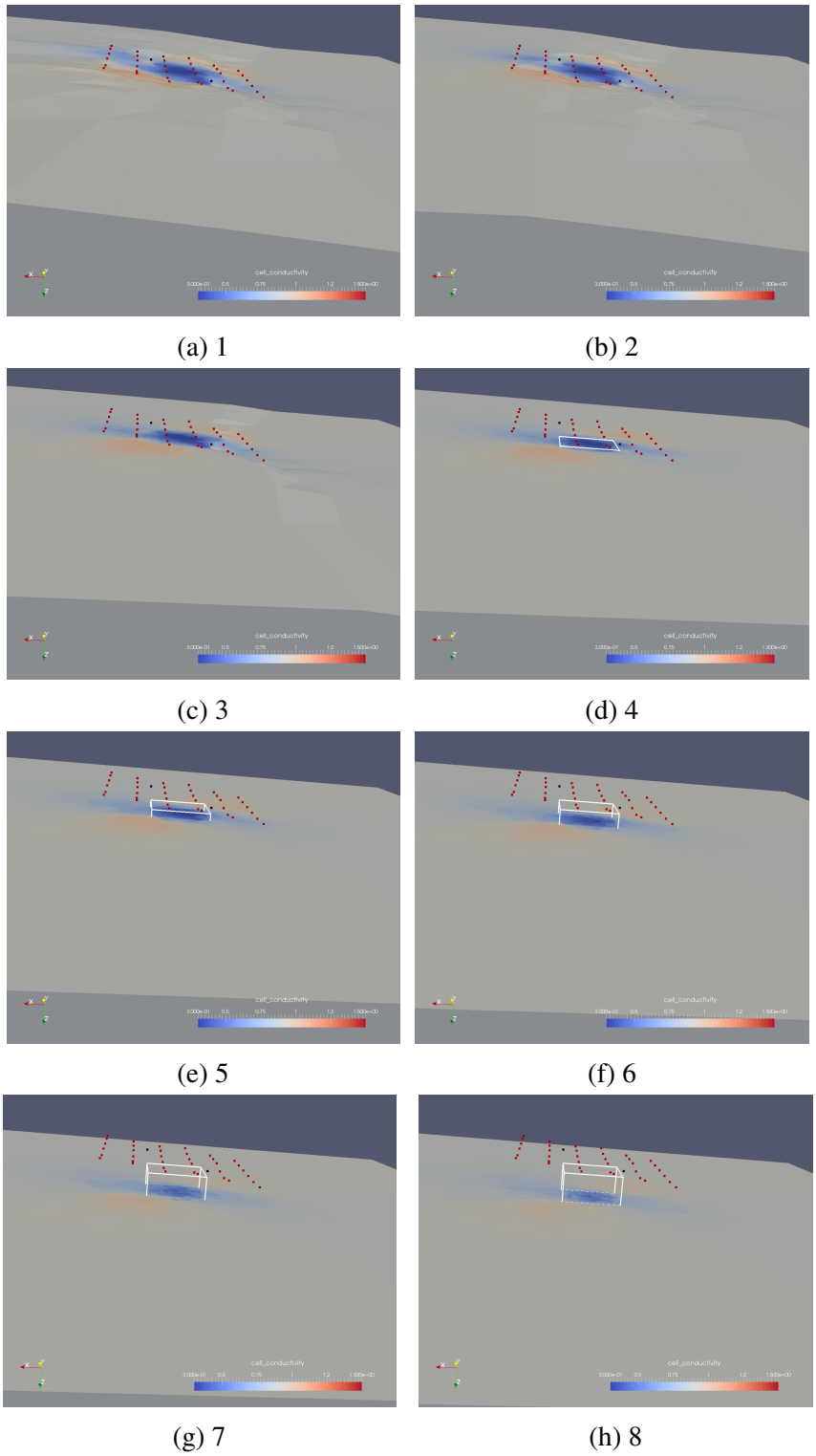

(a) 1 (b) 2

(c) 3 (d) 4

(e) 5 (f) 6

(g) 7 (h) 8

Figure 3.27: Vertical variation of the final model: from offset 1 to 8

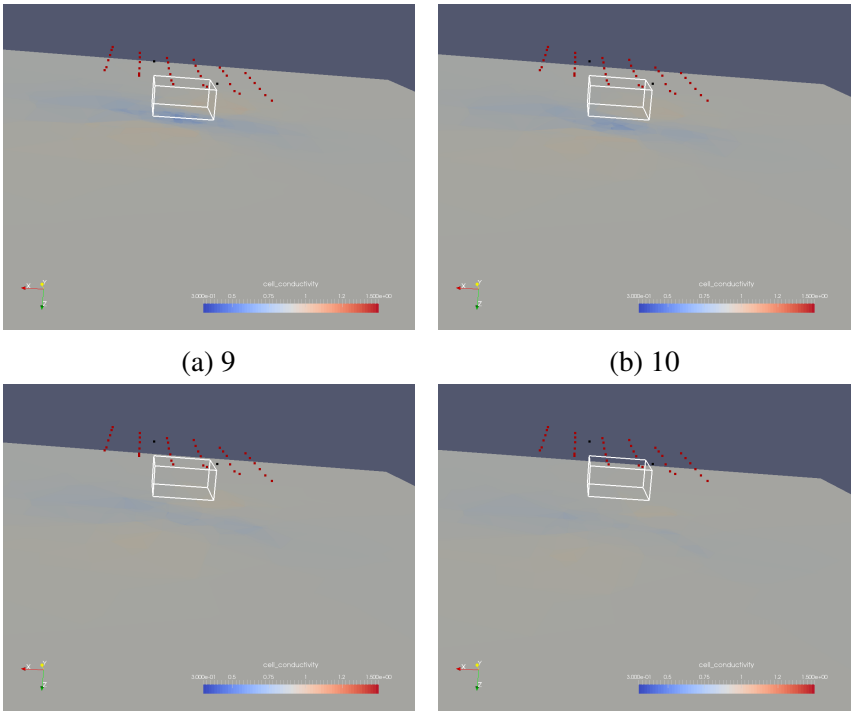

(a) 9 (b) 10

(c) 11 (d) 12

Figure 3.28: Vertical variation of the final model: from offset 9 to 14

including phase information into the data could increase the depth resolution of the inverted result. If the location of sharp discontinuities in resistivity is known, the penalty for roughness at the boundaries may be removed to allow sharp change of conductivity, since the inversion algorithm will not penalize the roughness at these boundaries.

The text of Chapter 3, in part, is being prepared for submission for publication of the material. Zhang, Y., Key, K., MARE3DEM: A Three-dimensional CSEM Inversion Based on A Parallel Adaptive Finite Element Method Using Unstructured Meshes. The dissertation author was the primary investigator and author of this paper.

Chapter 4

Conclusion and Outlook

4.1 Conclusions

We have successfully developed a novel goal-oriented adaptive finite-element scheme for controlled-source electromagnetic modeling. The curl-curl electric field equation is discretized utilizing the curl-conforming shape functions and unstructured grids. The resulting equation system is solved by direct solve based on Gaussian elimination, such as LU decomposition. The advantages of goal-oriented approaches are highlighted. As the core idea of goal-oriented error estimation, both residual based method and hierarchical basis method has been developed. Therefore, an accurate and efficient 3D code for CSEM modeling and inversion is available. It has the capability to automatically improve the accuracy for complex models. We point out that the main idea of the goal-oriented scheme is applicable to other equations, provided the modification of the dual function.

Although the proposed goal-oriented scheme requires a series of iteratively refined meshes, this approach is applicable for inversion using the dual grid strategy. In the inversion, we can use a fixed size inversion grid and a set of variable size forward

simulation grids. Accurate responses and sensitivity kernel could be calculated on the forward model and being efficiently mapped to the inversion grid. On the contrary, the updated model parameter on the inversion grid could be mapped to the forward model. Synthetic studies were carried out to understand the model space of a half-space model, as well as oil reservoir model with complex topography. In the half-space model, our results shows the true values of conductivity could be recovered using different data types. However, for the oil reservoir model, the values of conductivity are not the most probable, compared with the integrated resistivity thickness product. Our Occam's inversion was able to successfully delineate the reservoir laterally, with good indication of its depth but not thickness. Finally, we would like to point out that our inversion framework depends little on the nature of the forward problem, which could be used for any problem where a 3D smooth model is preferred.

4.2 Outlook

During the five years of my Ph.D study, I was able to implement the modeling and inversion for 3D CSEM presented in Chapter 2 and 3. The development of a robust and efficient algorithm should be a continuous effort to integrated the feedback of the users in the EM community. To make further improvement for 3D modeling and imaging, in this section I highlight the promising areas for future research, including developing the iterative solver for the equation system, as well as improving the scalability of inversion.

4.2.1 Iterative solver development

The discretization of a partial differential equation, which is by nature continuous, produces a very sparse system of linear equations with a finite number of unknowns:

$$\mathbf{Ax} = \mathbf{b} \tag{4.1}$$

Where **A** is the stiffness matrix and **b** is the source vector. **x** approximates the solution of the partial differential equation. Since the size of the problem is dependent on the discretization of the model, in the case of 3D modeling which involves many degrees of freedom per point, the derived linear system normally have hundreds of millions of unknowns, the system matrix **A** is extremely large. Therefore, solving the large-scale system efficiently is an crucial step to speed up the overall calculation.

There are two groups of methods for solving linear equation systems. The first one is the direct method, which derived from Gauss Elimination. The main advantage of direct solvers is that they are very robust and predictable, compared with iterative methods. Namely, direct methods guarantee that all matrices, except singular ones, can be solved. However, since direct solver involves decomposing the original matrix **A** into the factorized matrixes, resulting in the increasing of the number of non-zero entries in the system. Even for the most efficient direct solver, the maximum size of the problem can have no more than 10 million unknowns. It is clear that direct methods are not the ideal choice for the numerical scheme that has to deal with such enormous problems.

The second options are the iterative methods, which solve the system in an iterative fashion. Compared to direct methods, iterative techniques have the advantage of low storage requirements. Also, they can be parallelized much more efficiently. Therefore, iterative solver has the potential to solve large systems more efficiently in parallel. However, a problem associated with iterative solvers is that they are not as robust

as direct ones and also they are not generic. Moreover, there is not any mathematical rule that can tell us which iterative solver is the best and most efficient choice for each particular problem. The way to find out the most suitable iterative method for a certain problem is to implement different options and to test them empirically. Currently, the most widely used group of iterative techniques are Krylov subspace methods, which commonly include GMRES, QMR and BiCGStab algorithms.

Although Krylov subspace methods have many advantages, the convergence of Krylov subspace methods which heavily depends on the condition number of the system matrix $\mathbf{A}$ can vary a lot. Matrices with small condition numbers tend to converge rapidly, while those with large ones converge much slower. In the marine CSEM application, due to the high conductivity contrasts in models, the condition number is very large. Besides, the high element size ratios in unstructured meshes considerably deteriorate the condition numbers. Therefore, the Krylov method commonly converge very slowly in marine CSEM application.

In order to expedite the convergence, a variety of pre-conditioners, such as Jacobi, symmetric successive over-relaxation and incomplete LU factorization, have to be designed and applied. A good preconditioning technique can substantially improve both the efficiency and robustness of an iterative method. For example, the low induction number pre-conditioner in [Newman and Alumbaugh, 2002], as well the the multigrid pre-conditioner in [Haber et al., 2000] has been developed to further improve the computational efficiency. To emphasis the significance of preconditioning for solving the equation system, the reliability of iterative solvers depends much more on the quality of the pre-conditioner than on the particular Krylov subspace method. Examples could be found in both [Everett, 2012] and [Koldan, 2013], which use multigrid preconditioning to solve the finite element system, improving the robustness and efficiency of the iterative solver.

4.2.2 Inversion scalability improvement

In chapter 3, I explained the Occam's scheme to iteratively solve for the final model with minimal data misfit. The key step is to calculated the new model based on the model update equation (Equation. 4.2). In the model update equation, the prejudice term **P** and the roughness term **R** are sparse matrices that are trivial to compute, whereas the computationally expensive parts are the matrix multiplication and Cholesky factorization associated with the weighted Jacobian term **WJ**.

$$\mathbf{m}_{k+1} = [\mu(\mathbf{R}^T\mathbf{R} + \mathbf{P}^T\mathbf{P}) + \mathbf{W}\mathbf{J}^T\mathbf{W}\mathbf{J}]^{-1}[(\mathbf{W}\mathbf{J})^T\mathbf{W}\hat{\mathbf{d}} + \mu\mathbf{P}^T\mathbf{P}\mathbf{m}_*] \tag{4.2}$$

To support the inversion of large data sets with high efficiency for these 3D applications, we could implement the dense matrix operations in its distributed form. [Key, 2016] has implement the distributed calculations in 2D case using the ScaLAPACK library [Blackford et al., 1997]. Since the structure of our 2D and 3D algorithms are very similar, the framework of distributed computation could also be transferred from 2D to 3D. In figure 4.1, we illustrates an example of using ScaLAPACK to compute the dense matrix multiplication and Cholesky factorization. From the 2D result, we could infer the scalability in 3D, since the performance is only dependent on the number of free parameters, instead of the dimension of the modeling problem.

Test cases are shown for m = n = 20,000, 40,000 and 80,000, when run on 8 to 480 2.6GHz Intel Xeon processors connected with a quad data rate Infini-band network. In the case with 80,000 unknowns, the matrix-matrix multiplication took over one hour when carried out on 8 processors, yet was reduced to only 95 seconds when run on 480 processors. A similar reduction is seen for the Cholesky factorization, which runs about 50% faster than the matrix multiplication. For the speed-ups, both the matrix multiplication and Cholesky routines scale very well for the large matrix case with

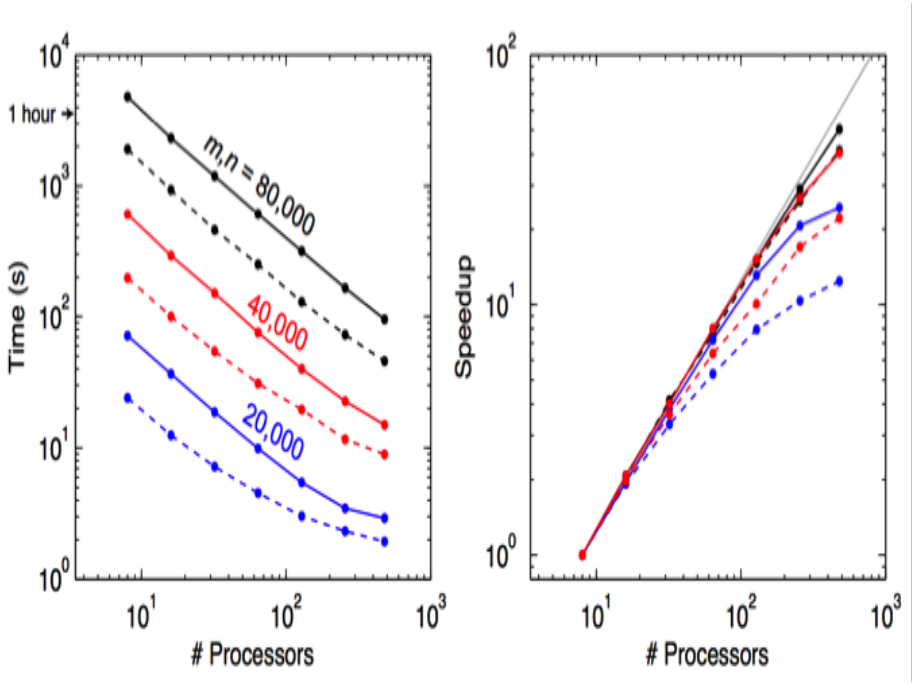

Figure 4.1: Run-time scaling (left) and speed-up (right) of the ScaLAPACK routines used for the dense matrix operations. Solid lines show the time to compute the dense matrix product $(WJ)^T WJ$. Dashed lines show the time required to solve the linear system using the Cholesky factorization routines.

80,000 parameters, reaching speed-ups of about 50 and 40 when run on 480 processors, which is close to the theoretical maximum speed-up of 60.

In the Occam's framework, we need to explicitly calculate and store the jacobian matrix **J**, which is dense matrix. The cost of the manipulations on **J**, such as multiplication and factorization, are expensive, even on a distributed computing system. Those inversion techniques with better memory efficiency lie in the context of conjugate gradient methods, which avoid the explicit storage of **J** in memory by only computing the action of **J** on a vector ([Mackie and Madden, 1993, Newman and Alumbaugh, 2000]). Although the frugal use of memory could be very beneficial for large 3D problem, the convergence of conjugate gradient method is much slower than Gauss-Newton inversion.

Bibliography

[Ainsworth and Oden, 1997] Ainsworth, M. and Oden, J. T. (1997). A posteriori error estimation in finite element analysis. *Computer Methods in Applied Mechanics and Engineering*, 142(1-2):1–88.

[Avdeev and Avdeeva, 2009] Avdeev, D. and Avdeeva, A. (2009). 3D magnetotelluric inversion using a limited-memory quasi-Newton optimization. *GEOPHYSICS*, 74(3):F45–F57.

[Avdeev et al., 2002] Avdeev, D. B., Kuvshinov, A. V., Pankratov, O. V., and Newman, G. A. (2002). Three-dimensional induction logging problems, part i: An integral equation solution and model comparisons. *Geophysics*, 67(2):413–426.

[Bank and Ovall, 2007] Bank, R. E. and Ovall, J. S. (2007). Dual Functions for a Parallel Adaptive Method. *SIAM Journal on Scientific Computing*.

[Becker and Rannacher, 2001] Becker, R. and Rannacher, R. (2001). An optimal control approach to ¡em¿a posteriori¡/em¿ error estimation in finite element methods. *Acta Numerica 2001*, 10:1–102.

[Blackford et al., 1997] Blackford, L. S., Choi, J., Cleary, A., D'Azevedo, E., Demmel, J., Dhillon, I., Dongarra, J., Hammarling, S., Henry, G., Petitet, A., et al. (1997). *ScaLAPACK users' guide*, volume 4. siam.

[Börner, 2009] Börner, R.-U. (2009). Numerical Modelling in Geo-Electromagnetics: Advances and Challenges. *Surveys in Geophysics*, 31(2):225–245.

[Brenner and Scott, 2008] Brenner, S. C. and Scott, L. R. (2008). Series: Texts in applied mathematics. *The mathematical theory of finite element methods*, 15.

[Chen and Dickens, 2009] Chen, J. and Dickens, T. A. (2009). Effects of uncertainty in rock-physics models on reservoir parameter estimation using seismic amplitude variation with angle and controlled-source electromagnetics data. *Geophysical Prospecting*, 57(1):61–74.

[Coggon, 1971] Coggon, J. (1971). Electromagnetic and electrical modeling by the finite element method. *Geophysics*, 36(1):132–155.

[Commer and Newman, 2008] Commer, M. and Newman, G. A. (2008). New advances in three-dimensional controlled-source electromagnetic inversion. *Geophysical Journal International*.

[Constable and Srnka, 2007] Constable, S. and Srnka, L. J. (2007). An introduction to marine controlled-source electromagnetic methods for hydrocarbon exploration. *Geophysics*, 72(2):WA3–WA12.

[Constable and Weiss, 2006a] Constable, S. and Weiss, C. J. (2006a). Mapping thin resistors and hydrocarbons with marine em methods: Insights from 1d modeling. *Geophysics*, 71(2):G43–G51.

[Constable and Weiss, 2006b] Constable, S. and Weiss, C. J. (2006b). Mapping thin resistors and hydrocarbons with marine EM methods: Insights from 1D modeling. *GEOPHYSICS*, 71(2):G43–G51.

[Constable et al., 1998] Constable, S. C., Orange, A. S., Hoversten, G. M., and Morrison, H. F. (1998). Marine magnetotellurics for petroleum exploration part i: A sea-floor equipment system. *Geophysics*, 63(3):816–825.

[Constable et al., 2012] Constable, S. C., Parker, R. L., and Constable, C. G. (2012). Occam's inversion: A practical algorithm for generating smooth models from electromagnetic sounding data. *GEOPHYSICS*, 52(3):289–300.

[Darnet et al., 2007] Darnet, M., Choo, M. C., Plessix, R.-E., Rosenquist, M. L., Yip-Cheong, K., Sims, E., and Voon, J. W. (2007). Detecting hydrocarbon reservoirs from csem data in complex settings: Application to deepwater sabah, malaysia. *Geophysics*, 72(2):WA97–WA103.

[Druskin and Knizhnerman, 1994] Druskin, V. and Knizhnerman, L. (1994). Spectral approach to solving three-dimensional maxwell's diffusion equations in the time and frequency domains. *Radio Science*, 29(04):937–953.

[Du, 2014] Du, Z. (2014). Using seismic guided em inversion to explore a complex geological area: An application to the kraken and bressay heavy oil discoveries, north sea. In *SEG Technical Program Expanded Abstracts 2014*, pages 781–785. Society of Exploration Geophysicists.

[Edwards, 2005] Edwards, N. (2005). Marine Controlled Source Electromagnetics: Principles, Methodologies, Future Commercial Applications - Springer. *Surveys in Geophysics*.

[Eidesmo et al., 2002] Eidesmo, T., Ellingsrud, S., MacGregor, L., Constable, S., Sinha, M., Johansen, S., Kong, F., and Westerdahl, H. (2002). Sea bed logging (sbl), a new method for remote and direct identification of hydrocarbon filled layers in deepwater areas. *First break*, 20(3).

[Ellingsrud et al., 2002] Ellingsrud, S., Eidesmo, T., Johansen, S., Sinha, M., MacGregor, L., and Constable, S. (2002). Remote sensing of hydrocarbon layers by seabed logging (sbl): Results from a cruise offshore angola. *The Leading Edge*, 21(10):972–982.

[Estep et al., 2006] Estep, D., Holst, M., and Larson, M. (2006). Generalized Green's Functions and the Effective Domain of Influence. *SIAM Journal on Scientific Computing*, 26(4):1314–1339.

[Evans, 1998] Evans, L. C. (1998). Partial differential equations. *Graduate Studies in Mathematics*, 19.

[Everett, 2012] Everett, M. E. (2012). Theoretical developments in electromagnetic induction geophysics with selected applications in the near surface. *Surveys in geophysics*, 33(1):29–63.

[Franke et al., 2007] Franke, A., Börner, R. U., and Spitzer, K. (2007). Adaptive unstructured grid finite element simulation of two-dimensional magnetotelluric fields for arbitrary surface and seafloor topography. *Geophysical Journal ...*.

[Giles and Süli, 2002] Giles, M. B. and Süli, E. (2002). Adjoint methods for PDEs: a posteriori error analysis and postprocessing by duality. *Acta Numerica*.

[Grayver, 2015] Grayver, A. V. (2015). Parallel three-dimensional magnetotelluric inversion using adaptive finite-element method. part i: theory and synthetic study. *Geophysical Journal International*, 202(1):584–603.

[Grayver and Kolev, 2015] Grayver, A. V. and Kolev, T. V. (2015). Large-scale 3D geoelectromagnetic modeling using parallel adaptive high-order finite element method. *GEOPHYSICS*, 80(6):E277–E291.

[Habashy and Abubakar, 2004] Habashy, T. M. and Abubakar, A. (2004). A general framework for constraint minimization for the inversion of electromagnetic measurements. *Progress in electromagnetics Research*, 46:265–312.

[Haber et al., 2000] Haber, E., Ascher, U. M., Aruliah, D. A., and Oldenburg, D. W. (2000). Fast Simulation of 3D Electromagnetic Problems Using Potentials. *Journal of Computational Physics*, 163(1):150–171.

[Haber and Heldmann, 2007] Haber, E. and Heldmann, S. (2007). An octree multigrid method for quasi-static maxwell?s equations with highly discontinuous coefficients. *Journal of Computational Physics*, 223(2):783–796.

[Haber et al., 2007] Haber, E., Heldmann, S., and Ascher, U. (2007). Adaptive finite volume method for distributed non-smooth parameter identification. *Inverse Problems*, 23(4):1659.

[Hedlin and Constable, 2012] Hedlin, C. d. and Constable, S. (2012). Occam's inversion to generate smooth, two-dimensional models from magnetotelluric data. *GEOPHYSICS*, 55(12):1613–1624.

[Hohmann, 1988] Hohmann, G. W. (1988). Numerical modeling for electromagnetic methods of geophysics. *Electromagnetic methods in applied geophysics*, 1:313–363.

[Holst, 2001] Holst, M. (2001). Adaptive Numerical Treatment of Elliptic Systems on Manifolds. *Advances in Computational Mathematics*, 15(1-4):139–191.

[Hoversten et al., 2000] Hoversten, G. M., Constable, S. C., and Morrison, H. F. (2000). Marine magnetotellurics for base-of-salt mapping: Gulf of mexico field test at the gemini structure. *Geophysics*, 65(5):1476–1488.

[Hughes, 2012] Hughes, T. J. (2012). *The finite element method: linear static and dynamic finite element analysis*. Courier Corporation.

[Jin, 2014] Jin, J.-M. (2014). *The finite element method in electromagnetics*. John Wiley & Sons.

[Key, 2009] Key, K. (2009). 1d inversion of multicomponent, multifrequency marine csem data: Methodology and synthetic studies for resolving thin resistive layers. *Geophysics*, 74(2):F9–F20.

[Key, 2012a] Key, K. (2012a). Marine electromagnetic studies of seafloor resources and tectonics. *Surveys in geophysics*, 33(1):135–167.

[Key, 2012b] Key, K. (2012b). Marine electromagnetic studies of seafloor resources and tectonics. *Surveys in geophysics*, 33(1):135–167.

[Key, 2016] Key, K. (2016). Mare2dem: a 2-d inversion code for controlled-source electromagnetic and magnetotelluric data. *Geophysical Journal International*, 207(1):571–588.

[Key and Ovall, 2011a] Key, K. and Ovall, J. (2011a). A parallel goal-oriented adaptive finite element method for 2.5-D electromagnetic modelling. *Geophysical Journal International*.

[Key and Ovall, 2011b] Key, K. and Ovall, J. (2011b). A parallel goal-oriented adaptive finite element method for 2.5-d electromagnetic modelling. *Geophysical Journal International*, 186(1):137–154.

[Key and Weiss, 2006a] Key, K. and Weiss, C. (2006a). Adaptive finite-element modeling using unstructured grids: The 2d magnetotelluric example. *Geophysics*, 71(6):G291–G299.

[Key and Weiss, 2006b] Key, K. and Weiss, C. (2006b). Adaptive finite-element modeling using unstructured grids: The 2D magnetotelluric example. *GEOPHYSICS*, 71(6):G291–G299.

[Key, 2003] Key, K. W. (2003). Application of broadband marine magnetotelluric exploration to a three-dimensional salt structure and a fast-spreading ridge.

[Koldan, 2013] Koldan, J. (2013). Numerical solution of 3-d electromagnetic problems in exploration geophysics and its implementation on massively parallel computers.

[Li and Constable, 2007] Li, Y. and Constable, S. (2007). 2d marine controlled-source electromagnetic modeling: Part 2?the effect of bathymetry. *Geophysics*, 72(2):WA63–WA71.

[Li and Key, 2007] Li, Y. and Key, K. (2007). 2D marine controlled-source electromagnetic modeling: Part 1 — An adaptive finite-element algorithm. *GEOPHYSICS*, 72(2):WA51–WA62.

[Mackie and Madden, 1993] Mackie, R. L. and Madden, T. R. (1993). Three-dimensional magnetotelluric inversion using conjugate gradients. *Geophysical Journal International*.

[Mackie et al., 1993] Mackie, R. L., Madden, T. R., and Wannamaker, P. E. (1993). Three-dimensional magnetotelluric modeling using difference equations—Theory and comparisons to integral equation solutions. *GEOPHYSICS*, 58(2):215–226.

[McGillivray et al., 1994] McGillivray, P., Oldenburg, D., Ellis, R., and Habashy, T. (1994). Calculation of sensitivities for the frequency-domain electromagnetic problem. *Geophysical Journal International*, 116(1):1–4.

[Menke, 1984] Menke, W. (1984). Geophysical data analysis: Discrete inverse theory academic. *New York*.

[Mitsuhata and Uchida, 2004] Mitsuhata, Y. and Uchida, T. (2004). 3d magnetotelluric modeling using the t-ω finite-element method. *Geophysics*, 69(1):108–119.

[Monk, 2003] Monk, P. (2003). *Finite element methods for Maxwell's equations*. Oxford University Press.

[Naif et al., 2013] Naif, S., Key, K., Constable, S., and Evans, R. (2013). Melt-rich channel observed at the lithosphere-asthenosphere boundary. *Nature*, 495(7441):356–359.

[Nam et al., 2007] Nam, M. J., Kim, H. J., Song, Y., Lee, T. J., Son, J.-S., and Suh, J. H. (2007). 3d magnetotelluric modelling including surface topography. *Geophysical Prospecting*, 55(2):277–287.

[Nédélec, 1986] Nédélec, J.-C. (1986). A new family of mixed finite elements in r 3. *Numerische Mathematik*, 50(1):57–81.

[Newman and Alumbaugh, 1997] Newman, G. and Alumbaugh, D. (1997). Three-dimensional massively parallel electromagnetic inversion?i. theory. *Geophysical journal international*, 128(2):345–354.

[Newman and Alumbaugh, 2000] Newman, G. A. and Alumbaugh, D. L. (2000). Three-dimensional magnetotelluric inversion using non-linear conjugate gradients. *Geophysical journal ...*.

[Newman and Alumbaugh, 2002] Newman, G. A. and Alumbaugh, D. L. (2002). Three-dimensional induction logging problems, part 2: A finite-difference solution. *Geophysics*, 67(2):484–491.

[Newman and Commer, 2005] Newman, G. A. and Commer, M. (2005). New advances in three dimensional transient electromagnetic inversion. *Geophysical Journal International*, 160(1):5–32.

[Nitsche and Schatz, 1974] Nitsche, J. A. and Schatz, A. H. (1974). Interior estimates for Ritz-Galerkin methods. *Mathematics of Computation*, 28(128):937–958.

[Oden and Prudhomme, 2001] Oden, J. T. and Prudhomme, S. (2001). Goal-oriented error estimation and adaptivity for the finite element method. *Computers & mathematics with applications*, 41(5):735–756.

[Oristaglio and Spies, 1999] Oristaglio, M. and Spies, B. (1999). *Three-dimensional electromagnetics*. Society of Exploration Geophysicists.

[Ovall, 2006] Ovall, J. S. (2006). Asymptotically exact functional error estimators based on superconvergent gradient recovery. *Numerische Mathematik*, 102(3):543–558.

[Parker, 1994] Parker, R. L. (1994). *Geophysical inverse theory*. Princeton university press.

[Pierce and Giles, 2006] Pierce, N. A. and Giles, M. B. (2006). Adjoint Recovery of Superconvergent Functionals from PDE Approximations. *SIAM review*, 42(2):247–264.

[Press, 2007] Press, W. H. (2007). *Numerical recipes 3rd edition: The art of scientific computing*. Cambridge university press.

[Press et al., 1996] Press, W. H., Teukolsky, S. A., Vetterling, W. T., and Flannery, B. P. (1996). Numerical recipes in fortran 77, ed. 2.

[Raiche, 1974] Raiche, A. (1974). An integral equation approach to three-dimensional modelling. *Geophysical Journal International*, 36(2):363–376.

[Ray et al., 2014] Ray, A., Key, K., Bodin, T., Myer, D., and Constable, S. (2014). Bayesian inversion of marine csem data from the scarborough gas field using a transdimensional 2-d parametrization. *Geophysical Journal International*, 199(3):1847–1860.

[Ren et al., 2013] Ren, Z., Kalscheuer, T., Greenhalgh, S., and Maurer, H. (2013). A goal-oriented adaptive finite-element approach for plane wave 3-d electromagnetic modelling. *Geophysical Journal International*, page ggt154.

[Schwalenberg and Edwards, 2004] Schwalenberg, K. and Edwards, R. (2004). The effect of seafloor topography on magnetotelluric fields: an analytical formulation confirmed with numerical results. *Geophysical Journal International*, 159(2):607–621.

[Schwarzbach and Haber, 2013] Schwarzbach, C. and Haber, E. (2013). Finite element based inversion for time-harmonic electromagnetic problems. *Geophysical Journal International*, 193(2):615–634.

[Si, 2015] Si, H. (2015). Tetgen, a delaunay-based quality tetrahedral mesh generator. *ACM Trans. Math. Softw.*, 41(2):11:1–11:36.

[Stratton, 2007] Stratton, J. A. (2007). *Electromagnetic theory*. John Wiley & Sons.

[Streich, 2009a] Streich, R. (2009a). 3d finite-difference frequency-domain modeling of controlled-source electromagnetic data: Direct solution and optimization for high accuracy. *Geophysics*, 74(5):F95–F105.

[Streich, 2009b] Streich, R. (2009b). 3D finite-difference frequency-domain modeling of controlled-source electromagnetic data: Direct solution and optimization for high accuracy. *GEOPHYSICS*, 74(5):F95–F105.

[Wannamaker et al., 1987] Wannamaker, P. E., Stodt, J. A., and Rijo, L. (1987). A stable finite element solution for two-dimensional magnetotelluric modelling. *Geophysical Journal International*, 88(1):277–296.

[Ward and Hohmann, 1988a] Ward, S. H. and Hohmann, G. W. (1988a). Electromagnetic theory for geophysical applications. In *Electromagnetic methods in applied geophysics*, volume 1, pages 131–311.

[Ward and Hohmann, 1988b] Ward, S. H. and Hohmann, G. W. (1988b). Electromagnetic theory for geophysical applications. *Electromagnetic methods in applied geophysics*, 1:131–311.

[Webb, 1999] Webb, J. P. (1999). Hierarchal vector basis functions of arbitrary order for triangular and tetrahedral finite elements. *Antennas and Propagation, IEEE Transactions on*, 47(8):1244–1253.

[Weiss and Newman, 2002] Weiss, C. J. and Newman, G. A. (2002). Electromagnetic induction in a fully 3-D anisotropic earth. *GEOPHYSICS*, 67(4):1104–1114.

[Wheelock et al., 2015] Wheelock, B., Constable, S., and Key, K. (2015). The advantages of logarithmically scaled data for electromagnetic inversion. *Geophysical Journal International*, 201(3):1765–1780.

[Yee et al., 1966] Yee, K. S. et al. (1966). Numerical solution of initial boundary value problems involving maxwell?s equations in isotropic media. *IEEE Trans. Antennas Propag*, 14(3):302–307.

[Zhang et al., 2015] Zhang, Y., Key, K., Ovall, J., and M, H. (2015). Parallel goal-oriented adaptive finite element modeling for 3D electromagnetic exploration. *SEG extended abstract*.

[Zhdanov, 2015] Zhdanov, M. S. (2015). *Inverse theory and applications in geophysics*, volume 36. Elsevier.

[Zhdanov et al., 2006] Zhdanov, M. S., Lee, S. K., and Yoshioka, K. (2006). Integral equation method for 3d modeling of electromagnetic fields in complex structures with inhomogeneous background conductivity. *Geophysics*, 71(6):G333–G345.

[Zhong et al., 2012] Zhong, L., Chen, L., Shu, S., Wittum, G., and Xu, J. (2012). Convergence and optimality of adaptive edge finite element methods for time-harmonic maxwell equations. *Mathematics of Computation*, 81(278):623–642.